

# Studies on the Characteristics of Post-Frontal Precipitation Structures in the Mid-Latitudes

Von der Fakultät für Mathematik und Physik  
der Gottfried Wilhelm Leibniz Universität Hannover  
zur Erlangung des Grades  
Doktorin der Naturwissenschaften  
Dr. rer. nat.  
genehmigte Dissertation

von

Dipl.-Met. Tanja Weusthoff  
geboren am 07.08.1976 in Gifhorn

2008

Referent: Prof. Dr. Thomas Hauf  
Korreferent: Prof. Dr. Dieter Etling

## Abstract

Quantitative precipitation forecast is a special challenge for numerical weather prediction models, which is amongst others due to the still unsatisfying representation of convective processes. This study aims at an analytical description of small-scale convective precipitation structures to enable a better understanding of the underlying processes and an improved numerical representation, for example in a stochastic way. Therefore, the well-known convective precipitation pattern in the rear of cold-fronts is analysed by means of the quantitative radar composite RZ of the German Weather Service. Through the restriction to one specific synoptic situation and by assuming that post-frontal showers are generated by a stochastic process, it is for the first time possible to describe not only the geometrical structure of the post-frontal precipitation field, but also the mean temporal development of the individual structures within the field by means of simple analytical equations.

In an Eulerian-type approach, the geometric structure and the radar derived rain rates are investigated by means of the instantaneous values at each distinct time step. Enclosed rain areas are identified as clusters and are discriminated according to the number of included local maxima of rain rates, where each maximum is assumed to represent a single convection cell. It turns out that the cell number  $p$  is a crucial parameter for the description of the geometric structure. Furthermore, the area and the area integrated rain rate (AIRR) per cell increase with increasing cell number until saturation effects appear at a specific cell count. This has not been observed before and may be explained with an equilibrium stage reached at that point of growth.

In a Lagrangian-type analysis, the temporal development of basic characteristics is investigated via a tracking of individual clusters. The whole growth process, from genesis through all growth stages till the final dissolving, is referred to as a track with each track having a specific life span. Three types of tracks are distinguished by means of their complexity. Despite large variabilities in the development of individual tracks, one universal function for the cluster specific area as well as the AIRR development is identified for all three track types. The respective parameters depend on the track type and the life span of the track only. This allows for the first time a surprisingly simple analytical description of the mean life cycle of post-frontal, precipitating convective clouds with the life span as the determinant parameter. The frequency distribution of the latter follows basically a power law for all track types.

Together with recalculations of previous results concerning the geometric structure with the high resolution radar data, a set of analytical functions and distributions is presented which describe the basic characteristics of post-frontal shower precipitation over Central Europe. One envisaged application of the results is the construction of a forecast scheme for post-frontal shower precipitation as a tool for a stochastic post processing of deterministic model output.

Keywords: cell, convection, life cycle, radar, temporal development

## Kurzfassung

Quantitative Niederschlagsvorhersage ist eine Herausforderung für numerische Wettervorhersagemodelle, u.a. aufgrund der nicht zufriedenstellenden Darstellung konvektiver Prozesse. Ziel dieser Studie ist eine analytische Beschreibung kleinskaliger konvektiver Niederschlagsstrukturen, die ein besseres Verständnis der zugrundeliegenden Prozesse sowie eine verbesserte numerische Beschreibung, z.B. auf stochastischer Basis, ermöglichen kann. Dazu wird das typische konvektive Niederschlagsfeld auf der Rückseite von Kaltfronten mit Hilfe des quantitativen Radarkomposits RZ des Deutschen Wetterdienstes untersucht. Durch die Beschränkung auf eine spezielle synoptische Situation und die Annahme, dass die Entstehung der Schauer auf stochastischen Prozessen basiert, ist es zum ersten Mal möglich die mittlere zeitliche Entwicklung der einzelnen Regengebiete analytisch zu beschreiben.

Die geometrische Struktur und die Regenraten werden anhand der 5-minütigen Momantanteile des Radarkomposits untersucht (Euler-Analyse). Abgeschlossene Niederschlagsgebiete werden als Cluster identifiziert und bezüglich der Anzahl der enthaltenen lokalen Maxima unterschieden, wobei jedes Maximum eine einzelne Konvektionszelle repräsentiert. Die Zellenanzahl  $p$  stellt sich als ein bestimmender Parameter für die Beschreibung der geometrischen Struktur heraus. Des Weiteren nimmt die Fläche sowie die flächenintegrierte Niederschlagsrate pro Zelle mit zunehmender Zellenanzahl zu, bis bei einer bestimmten Zellenanzahl Sättigung auftritt. Dies ist bisher so nicht beobachtet worden und lässt auf das Erreichen eines Gleichgewichtszustands schließen.

In einer Lagrange Analyse wird die zeitliche Entwicklung grundlegender Charakteristika mit Hilfe eines Trackings individueller Cluster untersucht. Der gesamte Wachstumsprozess eines Clusters wird als Track bezeichnet, wobei jeder Track eine bestimmte Lebensdauer hat. Es werden drei Arten von Tracks bezüglich ihrer Komplexität unterschieden. Trotz einer großen Variabilität in der zeitlichen Entwicklung individueller Tracks, beschreibt eine einzige Gleichung die mittlere zeitliche Entwicklung der Fläche sowie des flächenintegrierten Niederschlags für alle drei Track-Arten. Die entsprechenden Parameter hängen nur von der Art und der Lebensdauer des Tracks ab. Zum ersten Mal wurde solch eine überraschend einfache analytische Beschreibung der mittleren Entwicklung postfrontaler, konvektiver Niederschlagsstrukturen gefunden, die die Lebensdauer als bestimmenden Parameter enthält. Die Häufigkeitsverteilung der Lebensdauer wird für jede Track-Art durch ein Potenzgesetz beschrieben.

Zusammen mit Neuberechnungen der Ergebnisse früherer Untersuchungen mit den höher aufgelösten Radardaten, wird eine Reihe von analytischen Funktionen und Verteilungen präsentiert, die die grundlegenden Charakteristika postfrontaler Schauerniederschläge über Mitteleuropa beschreiben. Eine mögliche Anwendung der Ergebnisse liegt in der Entwicklung eines Vorhersageschemas, welches als stochastisches Postprocessing auf deterministische Modellvorhersagen aufgesetzt werden kann.

Schlagwörter: Konvektion, Lebenszyklus, Radar, zeitliche Entwicklung, Zelle

# Contents

<b>1</b>	<b>Introduction</b>	<b>1</b>
<b>2</b>	<b>Background</b>	<b>6</b>
2.1	Atmospheric Convection . . . . .	6
2.1.1	Mesoscale organisation of convection . . . . .	7
2.1.2	Life cycle of convective showers . . . . .	11
2.2	Weather Radar . . . . .	15
2.2.1	Radar principles . . . . .	16
2.2.2	German radar network . . . . .	18
2.2.3	Quantitative precipitation estimation . . . . .	19
2.2.4	Error sources . . . . .	21
<b>3</b>	<b>Data</b>	<b>24</b>
3.1	Radar data . . . . .	24
3.1.1	Data processing . . . . .	24
3.1.2	Radar data quality . . . . .	26
3.2	Tracks . . . . .	28
3.2.1	Definition . . . . .	28
3.2.2	Track types . . . . .	30
3.2.3	Basic evaluation . . . . .	32
<b>4</b>	<b>Local rain rates</b>	<b>35</b>
4.1	Diurnal cycle of rain rate classes . . . . .	35
4.2	Daily rain totals . . . . .	36
4.3	Duration of wet and dry events . . . . .	38
4.4	Discussion . . . . .	39

## Contents

---

<b>5</b>	<b>Geometry</b>	<b>40</b>
5.1	Recalculation of selected structural characteristics . . . . .	41
5.1.1	Diurnal cycles . . . . .	41
5.1.2	Cell number distribution . . . . .	43
5.1.3	Cluster size distribution . . . . .	45
5.2	Cluster orientation and motion . . . . .	48
5.3	Cell based characteristics . . . . .	52
5.4	Discussion . . . . .	53
<b>6</b>	<b>Temporal development</b>	<b>56</b>
6.1	Temporal development of area and AIRR for three different track types	57
6.1.1	Determination of mean time series and normalisation . . . . .	58
6.1.2	Fitting of normalised time series . . . . .	63
6.1.3	Life span dependency of non-normalised functions . . . . .	65
6.2	Area and time integrated rain sum . . . . .	69
6.3	Additional investigations . . . . .	70
6.3.1	AIRR per area . . . . .	70
6.3.2	Cell number development . . . . .	71
6.4	Discussion . . . . .	72
<b>7</b>	<b>Summary and conclusions</b>	<b>74</b>
<b>8</b>	<b>Limitations and Outlook</b>	<b>80</b>
<b>A</b>	<b>Track Examples</b>	<b>84</b>
A.1	Single-cell-tracks . . . . .	85
A.2	Single-cluster-tracks . . . . .	86
A.3	Multi-cluster-tracks . . . . .	87
<b>B</b>	<b>Movement of the precipitation field</b>	<b>88</b>
<b>C</b>	<b>Statistical measures</b>	<b>95</b>
<b>D</b>	<b>Parameters of the fitting functions for different life spans</b>	<b>97</b>

---

**Contents**

---

<b>E Coefficients of variation for mean time series</b>	<b>101</b>
E.1 Coefficients of variation for area . . . . .	101
E.2 Coefficients of variation for AIRR . . . . .	102
<b>Bibliography</b>	<b>103</b>
<b>List of Figures</b>	<b>109</b>
<b>List of Tables</b>	<b>112</b>
<b>List of Symbols</b>	<b>114</b>
<b>List of Abbreviations</b>	<b>116</b>
<b>Acknowledgements</b>	<b>117</b>
<b>Curriculum Vitae</b>	<b>118</b>

# Chapter 1

## Introduction

Precipitation is defined as condensed water vapour falling to the Earth's surface in a liquid or solid state of aggregation. It is generally classified into stratiform and convective precipitation. This thesis deals with the latter type which often leads to significant amounts of precipitation on small spatial and temporal scales. According to TETZLAFF AND HAGEMANN (1986), who analysed the precipitation type with data of the synoptical observation station Hannover-Herrenhausen for a period of six years (1979 - 1984), convection accounts for 24 % of the total precipitation. WALTHER (2007) analysed precipitation events over the Baltic area by means of radar data for the years 2000-2002, distinguishing convective and frontal precipitation. It was found that the annual overall fraction of convective events is about 36 %, with larger values over land than over the sea. Furthermore, almost half of the radar echoes equivalent to rain rates of more than  $10 \text{ mmh}^{-1}$  were identified to be related to convective processes.

Because of the small-scale nature of convection, the individual convection cells cannot be reproduced by current operational models. Although the resolution of the models has increased up to 2.8 km (COSMO-DE) now and deep convection is explicitly modelled, the small-scale structure of shallow convection is still not resolvable and needs to be parametrised. This is particularly true for global and climate models. The processes that govern the convective activity are still not fully understood. Especially convective initiation and the influence of orography are topics of current research. A better understanding of those processes in combination with new approaches for numerical representation, for example in a stochastic way, may lead to improved parametrisations and thus to a better quantitative precipitation forecast.

The spatial and temporal structure of precipitation fields has a significant influence on the components of the hydrological cycle, like for example the runoff, and constitutes an important input for hydrological models. Some of these models are based on long time series with high resolution precipitation data at single sites. Because of the lack of adequate data, such time series are generated stochastically



## Chapter 1. Introduction

---

(e.g. BÁRDOSSY (1998), HABERLANDT ET AL. (2007)), but without a distinction of different synoptic conditions. Another type of models directly takes into account the spatial structure of the precipitation field by modelling the characteristic patterns, especially for small hydrographic catchments (WILLEMS 2001). Here, often spatial and temporal stationarity is assumed. A review on recent developments with a focus on Poisson cluster-based models (for single-site modelling) and generalized linear models (for multi-site daily rainfall, non-stationary in space and time) can be found in WHEATER ET AL. (2005). A closer look on the structure and development of convective precipitation patterns could be beneficial for a better representation of precipitation in hydrological models.

The analyses presented in this thesis have been restricted to post-frontal shower fields. Those precipitation fields seemingly have a common structure which is apparent, for example, in the satellite derived cloud structure (see Figure 2.4). Based on the obvious similarities among different post-frontal precipitation fields, the assumption was made that they result from the same stochastic process and thus have identical statistical properties. It should be noted that post-frontal characteristics over sea differ significantly from those over land. Over sea, cloud streets as well as open and closed cells are observed while the appearance of the structures over land is less classifiable. The focus of this thesis is on mid-latitude convection over land. The results by THEUSNER (2007) and those of the present thesis confirm the assumption of common statistical properties for that type of convection. Due to the limited area of the radar composite, only Germany was considered for the analysis. However, it is hypothesised that the results are also applicable to other areas within Central Europe.

Convective precipitation fields have been studied at the *Institute of Meteorology and Climatology of the Leibniz University of Hannover* for more than 10 years now. HAESELER (1995) investigated the precipitation structure on the rear side of a trough and constructed a simple model for the spatial and temporal development of single shower cells with cloud thickness and cell velocity as input parameters. CLAUSEN AND ROTH (1997) worked on the regionalisation of convective precipitation from large scale climate models with a special focus on post-frontal showers. This was done by means of a conceptual model, relating large-scale properties, like the temperature in 850 hPa, to statistical information on precipitation parameters which describe single cells or an ensemble of cells, respectively. HAUF ET AL. (2001) investigated on a statistical basis the spatial and temporal structure of convective precipitation fields in the lowlands of Northern Germany as a prerequisite for a subscale parametrisation of precipitation in climate models. It was found that the precipitation intensity measured at a fixed location depends not only on the life span of the cells and the wind field, but to a high degree also on the orientation and geometrical formation of the shower cells. Hereupon, THEUSNER (2007) investigated the geometrical structure of the post-frontal precipitation field based on radar data with a spatial resolution of 2 km x 2 km and a temporal resolution of 15 min. A small number of parameters was found to be sufficient to describe the

## Chapter 1. Introduction

---

basic geometrical characteristics of the post-frontal shower field, for example the size distribution of the individual rain areas and the diurnal cycles of the number of rain areas and of the total precipitation area (see also Section 5.1). The observed day-to-day variability of the characteristics, however, could so far not be related to the synoptic conditions by means of conventional stability indices (WITHA 2007). Besides a conditional unstable stratification, a large scale lifting seems to be a necessary prerequisite for the formation of the shower structures.

Motivated by the promising results concerning the geometrical structure of the post-frontal precipitation field, the project *Hybrid probabilistic forecast scheme for post-frontal shower precipitation* (in the following referred to as *shower project*) was initiated in the scope of the the Priority Program 1167 *Quantitative Precipitation Forecast* of the German Research Foundation (DFG). The Priority Program was established because precipitation forecast has, in contrast to other parameters like temperature and wind, not significantly improved in the last 16 years. In order to identify and eliminate the prevailing deficiencies in quantitative precipitation forecast, the effort of university institutes and other research institutions were interconnected, together with the German Weather Service (DWD) providing the operational forecast system as a development, testing and validation instrument (HENSE ET AL. 2003).

One of the identified deficiencies concerns the temporal and spatial scale of precipitation events. It seems to be necessary to consider precipitation as a stochastic variable when using observational data and interpreting deterministic simulations. The shower project takes into account the stochastic nature of precipitation. By focusing on one special synoptic situation, simple analytical and statistical relationships could be derived, which allow an improvement of the precipitation forecast in a stochastic way. For a realisation of the planned forecast scheme, the investigation on the geometrical structure was extended by an analysis of rain intensity characteristics and temporal properties. For the latter, a tracking algorithm was developed by WEUSTHOFF (2005) and was in a first instance applied to two days with post-frontal shower precipitation. The preliminary results concerning growth processes of individual clusters within the shower field were confirmed with an enlarged data set of 17 days containing a total of over one million individual clusters (WEUSTHOFF AND HAUF 2008b). As a result, a simple growth model was proposed which describes the cluster growth process in terms of embedded convection cells (see Section 2.1.2).

The present thesis, which results from the shower project, aims at an analytical description of the mean temporal development of individual clusters within small-scale convective precipitation structures. As in previous studies, a special synoptic situation was chosen for the investigation, namely the precipitation field in the rear of a cold front. That post-frontal shower field shows a typical structure of convective shower precipitation, which can easily be identified in satellite or radar data. 17 days with post-frontal precipitation were analysed by means of radar data with a temporal resolution of 5 min and a spatial resolution of 1 km x 1 km. The high

## Chapter 1. Introduction

---

temporal resolution enabled the tracking of individual clusters which was the basis for the investigations on the individual clusters' time series. While the geometrical structure has been analysed by various authors in the last decades (a review can be found in MESNARD AND SAUVAGEOT (2003)), only one study is known where the temporal development of an ensemble of convection cells is analysed in a similar way by means of radar data (LÓPEZ ET AL. 1983).

The limitations of the analysis, i.e. the restriction to only one synoptic situation and the assumption of a stochastic process, only enabled the analytical description of the mean temporal development of individual small-scale precipitation structures in the way presented here. Such an investigation of the temporal development of rain rate and area for individual cluster tracks with respect to their life span has not been performed before. Furthermore, for the first time the mean time series of an ensemble of tracks which are grouped by the complexity of the development into three track types could be described by a simple analytical function. This function only depends on the life span.

Parts of the thesis have already been published in scientific journals. The investigations on the life cycle of convective showers can be found in the *Quarterly Journal of the Royal Meteorological Society* (WEUSTHOFF AND HAUF 2008b) while the analyses of the mean temporal development of the rain rate and the area of a cluster were submitted to the *Meteorologische Zeitschrift* this year (WEUSTHOFF AND HAUF 2008a).

## Objectives

The overall aim of this thesis is to give an analytical description of convective clusters and related rain rates within the post-frontal precipitation field. The key questions in this respect are:

1. Is it possible to derive a set of equations which describe the characteristics of the post-frontal precipitation field? What are the governing parameters?
2. How do the characteristics of the individual areas, like area size and rain rate, develop with time? Which analytical functions can be derived for the mean time series?
3. How can the rain rate characteristics be described?
4. Which shape can be assumed for the individual clusters in the precipitation field? And how are they related to the wind field?
5. Are the results of previous studies concerning the geometrical structure reproducible with the higher resolution RZ-composite?

### Structure of the work

This thesis is structured as follows. In **Chapter 2**, atmospheric convection is addressed including the life cycle characteristics of individual cells (Section 2.1.2) and mesoscale organisation of convection, with a special view on the post-frontal shower field (Section 2.1.1). Furthermore, the basic principles of weather radar are introduced (Section 2.2) as well as the German radar network and radar products of the DWD (Section 2.2.2). In **Chapter 3**, the data material is presented, comprising the radar data and the tracks. The latter are defined as the life cycle of individual clusters. The results are presented in the subsequent three chapters: In **Chapter 4**, basic investigations on the radar derived rain rates provided by the RZ composite are introduced. **Chapter 5** deals with the geometrical structure. Besides a recalculation of selected results of previous studies with the higher resolution data (Section 5.1), investigations on the shape and the orientation of the clusters (Section 5.2) as well as cell related properties (Section 5.3) are shown. The major results can be found in **Chapter 6**, namely the mean time series of area and rain rate for three different track types. Finally, a summary is given in **Chapter 7** and conclusions are drawn, followed by a short outlook (**Chapter 8**).

# Chapter 2

## Background

### 2.1 Atmospheric Convection

*If a body lighter than a fluid be forcibly immersed in it, the body will be driven upwards by a force equal to the difference between its weight and the weight of the fluid displaced.*

The sixth proposition from "On Floating Bodies", Archimedes, circa 260 B.C. (EMANUEL 1994)

Convection in the most general term refers to the movement of molecules within fluids resulting in transport and mixing of the properties. In atmospheric convection, the fluid is air and the process of convection results in the vertical heat transfer between different layers of the atmosphere. This heat transfer constitutes a compensation process caused by prevailing static instabilities. Because of the partially chaotic appearance, convection is often referred to as thermal turbulence (LILJEQUIST AND CEHAK 1974).

Meteorologists divide convection into dry and moist convection. Dry convection is apparent in non-saturated air without formation of clouds. Moist convection simply implies that the temperature of a rising air parcel cools down below the dew point and convective clouds form. A prerequisite for moist convection is atmospheric instability and especially conditional instability. Under conditional instabilities, an air parcel is unstable to up- and downward displacements, if it is saturated, but stable to small changes if the parcel is unsaturated. For the initiation of moist convection it is necessary, that the parcel is lifted above the condensation level. This may be caused by orographic uplift or by subsequent heating of the surface leading to a decreased stability of the near surface layer. Above the condensation level, cloud droplets form and the now saturated air parcel ascends further until the equilibrium

## Chapter 2. Background

---

level is reached, where the surrounding air is warmer than the ascending air parcel. This level marks the cloud top. The concept of atmospheric stability and the parcel theory are discussed in various textbooks, such as EMANUEL (1994), BLUESTEIN (1992) and BLUESTEIN (1993). Depending on the moisture of the air and the convective available potential energy (CAPE), the cloud droplets may grow to form much larger drops by the mechanisms of coalescence or the Bergeron-Findeisen process. When the convective clouds become so deep that the water droplets or ice crystals grow large enough to fall as precipitation, one speaks of precipitating convection (EMANUEL 1994).

Moist convection can generally be categorised in three types:

- (1) shallow non-precipitating convective clouds,
- (2) mid-level precipitating showers and
- (3) deep convection.

The emphasis of this thesis is on mid-level precipitating showers, whereas most previous studies on moist convection deal with deep convection. As the dynamic structure and the underlying processes are basically the same for all three categories, references in this chapter are frequently taken from deep convection studies.

Over homogeneous surfaces, particularly over oceans, moist convection becomes manifest in different types of ordered structures. Typical examples are open and closed hexagonal cells, cloud bands (across the direction of flow) and roll-convection (along the direction of flow) as described in BADER ET AL. (1995) and EMANUEL (1994), for example. These regular systems develop in the convective boundary layer and are related to non-precipitating shallow convection. When such structures are advected over land, they change their appearance due to coastal effects. The more irregular formation of mid-level and deep convection over land into convective complexes, which are subject of this thesis, is addressed in the following Section 2.1.1.

### 2.1.1 Mesoscale organisation of convection

Convection is often organised into larger mesoscale structures. Single convection cells combine to form clusters; AUSTIN AND HOUZE, JR. (1972) called those clusters small mesoscale area (SMSA). Several of those SMSA with a spatial extent of up to 1000 km<sup>2</sup> build a large mesoscale area (LMSA) with areas of up to several thousands of square kilometers. The post-frontal shower structures, which appear as an ensemble of several hundreds of convection cells and clusters of cells, can be allocated to the LMSA. The larger and more intense SMSAs are usually called mesoscale convective systems (MCS). Examples are squall lines and cloud clusters (EMANUEL 1997). MCSs are subject of various studies as they often cause heavy

## Chapter 2. Background

---

precipitation associated with flash floods. JEWETT AND WILHELMSON (2006), for example, investigated the mesoscale forcing on mid-latitude squall lines, while FU AND GUO (2006) analysed the role of merging on the formation of MCSs. A detailed overview over studies on MCSs over the past 10 - 15 years is given by HOUZE, JR. (2004). According to that study, MCSs are an important link between atmospheric convection and the larger-scale atmospheric circulation because they are associated with larger-scale wave motions.

### Post-frontal precipitation field

The subject of this study is a special case of atmospheric convection, namely the post-frontal shower precipitation field, its spatial organisation and the precipitation amount. This precipitation field is usually located behind a cold-front passing Germany in south-easterly directions. The convective structures develop in the approaching cold air masses of polar origin. They can easily be identified in satellite or radar data (Figures 2.4 and 2.5) by the characteristic cellular organisation. The apparent structuring of the precipitation field suggests simple underlying principles describing the structural characteristics and the corresponding precipitation. THEUSNER (2007) analysed the geometric structure of post-frontal precipitation fields by means of radar data and found that a small number of parameters is sufficient to describe the basic characteristics. In the present work, the analysis is extended by the precipitation rate characteristics and the temporal development of the individual convective complexes within the precipitation field, aiming at a better understanding of the formation and organisation of the investigated structures.

The characteristics of the precipitation field and the methodology of the data selection are in detail described in the previous works of WEUSTHOFF (2005) and THEUSNER (2007) on the same subject. Therefore, only a basic overview of the typical synoptic characteristics is given here by means of 9 November 2006. The synoptic situation is governed by a trough located over Northern Europe as can be seen in the 500 hPa chart in Figure 2.1. In the analysis of the 00 UTC surface chart (Figure 2.2), the cold front is located over Northern Germany, approximately parallel to the coast of the North Sea and moves in south-easterly direction. The air mass behind the cold-front shows a typical unstable structure favourable for convective activity. The radio sounding of Greifswald (Figure 2.3) reveals this unstable stratification up to a height of 7 km. In the satellite image of 1215 UTC (Figure 2.4), the post-frontal shower area is visible in the Northern part of Germany, approaching from north-west behind the cold-front, which at that time (1215 UTC) is located over Southern Germany and Austria. Embedded in the apparent convective cloud structure behind the cold-front, the precipitation is organised in contiguous rain areas as can be seen in the radar image (Figure 2.5).

## Chapter 2. Background

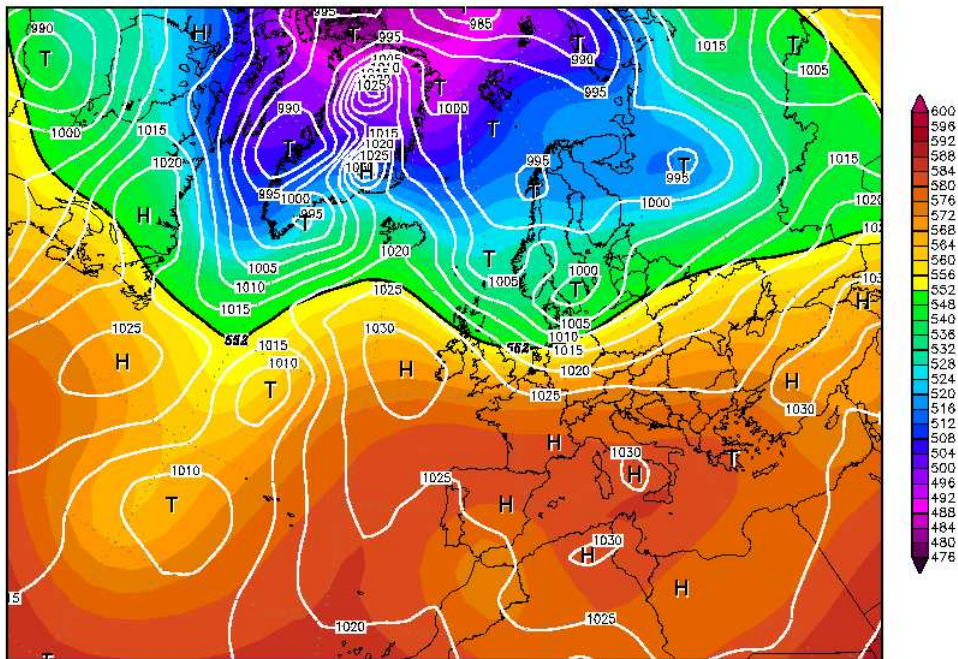


Figure 2.1: 500 hPa geopotential height [gpdm] and surface pressure [hPa], 9 November 2006, 00 UTC. Source: [www.wetterzentrale.de](http://www.wetterzentrale.de).

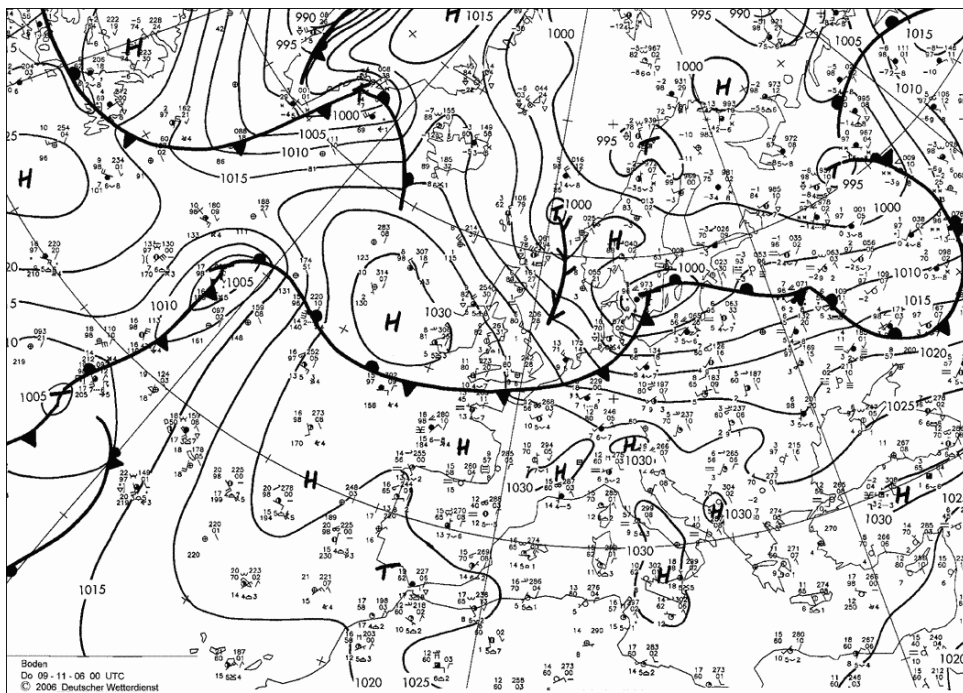
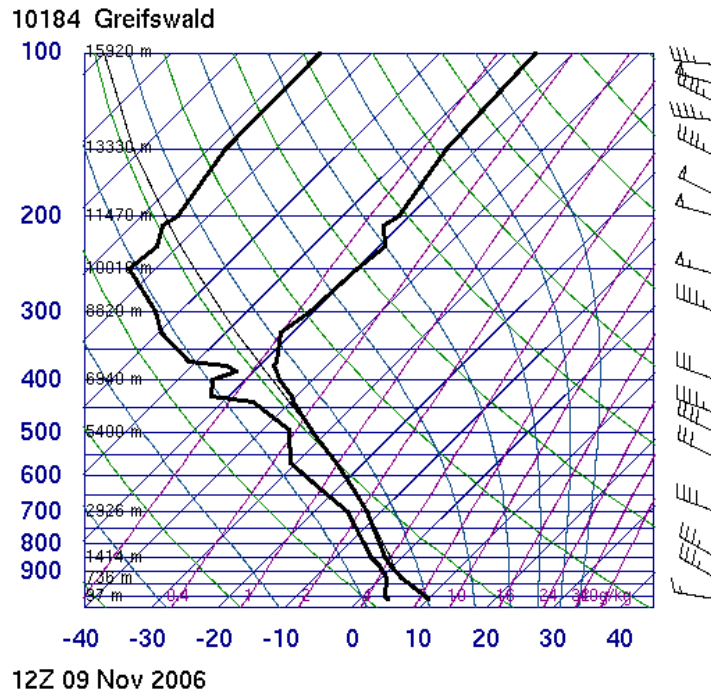


Figure 2.2: Analysis of surface chart, 9 November 2006, 00 UTC. Source: DWD.



## Chapter 2. Background

---



**Figure 2.3:** Radio sounding of Greifswald, 9 November 2006, 12 UTC. Source: University of Wyoming.

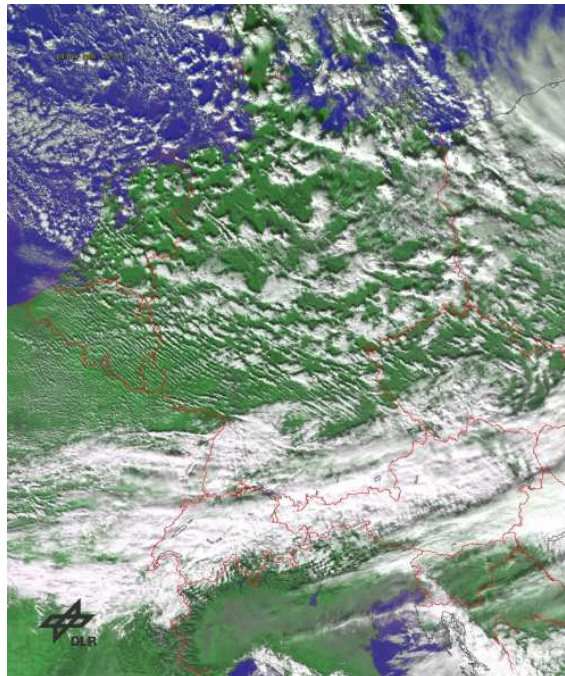


**Figure 2.4:** Satellite image of 9 November 2006, 1215 UTC. Source: DLR.

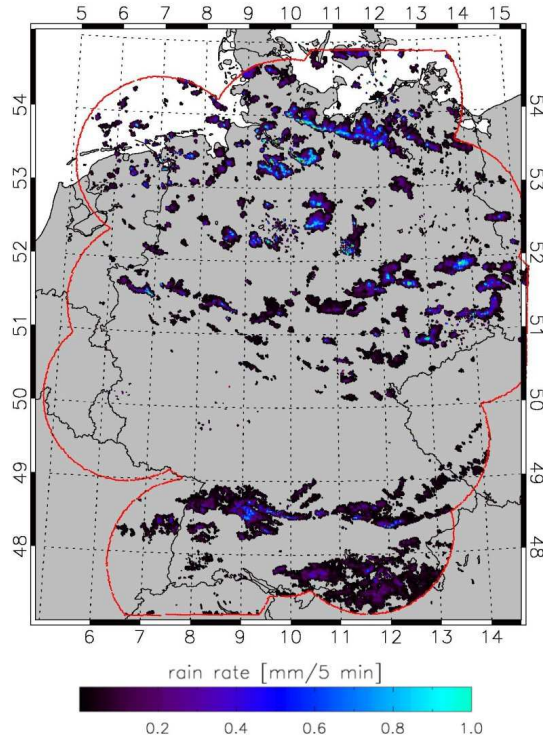


**Figure 2.5:** RZ-composite radar image of 9 November 2006, 1215 UTC. In Southern Germany, residuals of the frontal rain bands are present while in Northern Germany post-frontal shower precipitation prevails.

### 2.1.2 Life cycle of convective showers

The life cycle of precipitating convection cells has so far mainly been studied for the case of deep convection. The common idea of the life cycle of a single thunderstorm goes back to the early model proposed by Byers and Braham (BRAHAM JR. 1996) after the Thunderstorm Project in the late 1940s. They defined three stages in the life of a thunderstorm as depicted in Figure 2.6: towering cumulus stage, mature stage and dissipating stage. They also recognized the formation of individual cells in clusters. Although not explicitly dealt with at that time, this implies interactions among individual cells which may have consequences for the convective evolution, as was shown later, for example by JEWETT AND WILHELMSON (2006).

In the present study, mid-level convective showers as they appear in the post-frontal precipitation field (see Chapter 2.1.1) are investigated by means of radar data. Hereby, a shower is always related to a contiguous rain area in the radar image (in the following referred to as cluster) which may consist of one or more individual convection cells. Each of them is related to a maximum of reflectivity or precipitation rate, respectively. According to the number  $n$  of embedded cells, a cluster is referred to as an  $n$ -cell cluster. An example of a cluster comprising two individual convection cells is displayed in Figure 2.7 in a 3D representation. Each convection

## Chapter 2. Background

---

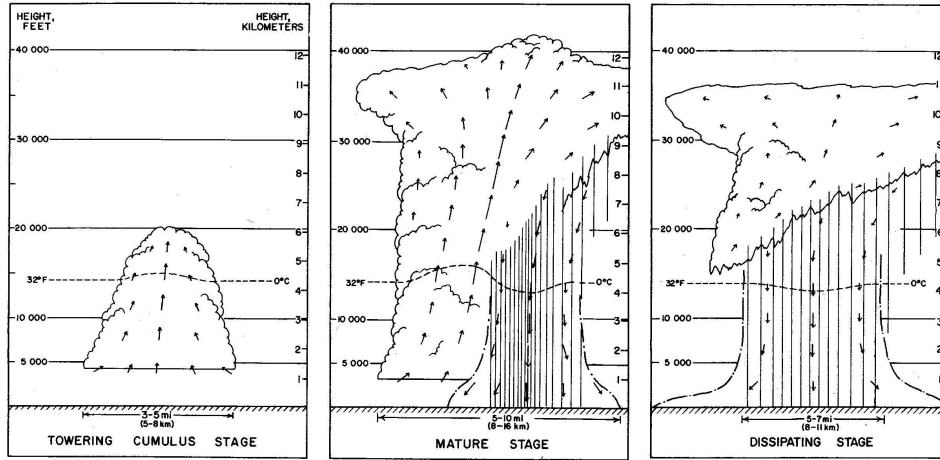


**Figure 2.6:** Life stages of a single convection cloud comprising towering cumulus stage, mature stage and dissipating stage (BLUESTEIN 1993).

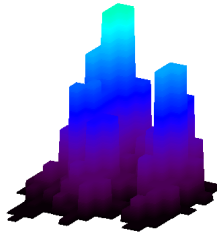


**Figure 2.7:** Example of a two-cell cluster in a 3D representation. Both the color and the height of the individual pixels indicate different rain intensities.

cell within a cluster runs through its individual life cycle which is comparable to that presented in Figure 2.6 for a single thunderstorm. Due to the formation of cells in clusters, neighbouring cells certainly have an effect on each others dynamics, which has already been observed for the case of deep convection.

Besides the individual life cycles of the embedded convection cells, the whole cluster shows a life cycle itself. The latter was investigated by tracking the clusters individually and relating the growth to the variation in the number of embedded cells (*number growth*). The results on the growth processes can be found in (WEUSTHOFF AND HAUF 2008b).

The whole life cycle of a cluster is in the following referred to as a *track*. Each track has a specific duration which is also called the life span of the track. Due to interactions amongst different clusters, a track refers to the whole set of clusters that were found to be precursor or successor of each other. The concept of tracks is addressed in more detail in Section 3.2. In the following, the individual growth processes within a track are considered. Within a time step of 5 min, a cluster with  $n$  maxima ( $n \geq 0$ ) develops to a cluster with  $m$  maxima ( $m \geq 0$ ):  $n \rightarrow m$ . Five life stages or transition processes were identified by visual inspection of radar time

## Chapter 2. Background

---

sequences (see Figure 2.8):

- (i) genesis,
- (ii) growth (including internal growth and merging),
- (iii) stagnation,
- (iv) decay (including internal decrease and splitting) and
- (v) dissolving.

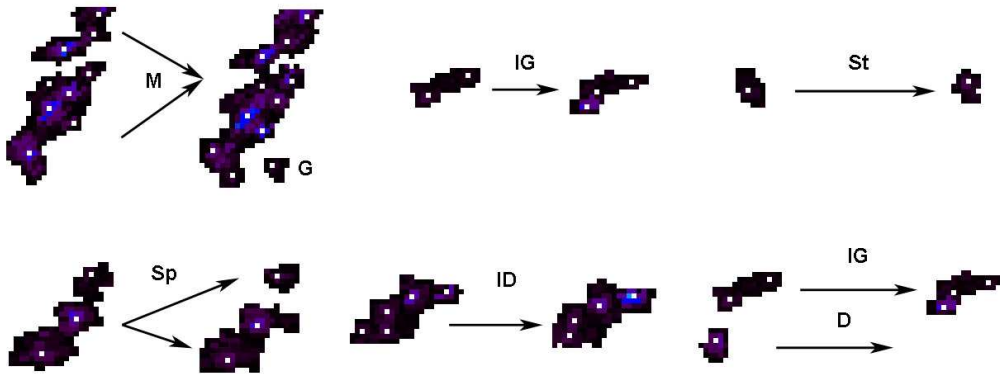


**Figure 2.8:** The life stages of a cluster (G = genesis, M = merging, IG = internal growth, St = Stagnation, Sp = splitting, ID = internal decrease, D = dissolving) (WEUSTHOFF AND HAUF 2008b).

For a description of the growth process, two different approaches are followed (WEUSTHOFF AND HAUF 2008b): the *cluster-based approach* and the *transition-based approach*.

1. In the *cluster-based approach* for each cluster identified in the radar data the transition process within the next time step is considered, which leads to one transition count per cluster. Growth is hereby subdivided into internal growth and merging, and decay, respectively, into internal decrease and splitting. As the processes are related to the starting cluster, each splitting counts only one transition process, while merging counts at least two processes, one for each actual cluster. As genesis is starting from no actual cluster, it is considered as an additional process.
2. The *transition-based approach*, in contrast, counts each transition from an  $n$ -cell cluster to an  $m$ -cell cluster ( $n \rightarrow m$ ). Merging and splitting are not especially accounted for in that approach. Each transition from the initial cluster  $n$  to any successor  $m$  is counted as an individual transition process. This includes also genesis ( $n = 0$ ) and dissolving ( $m = 0$ ).

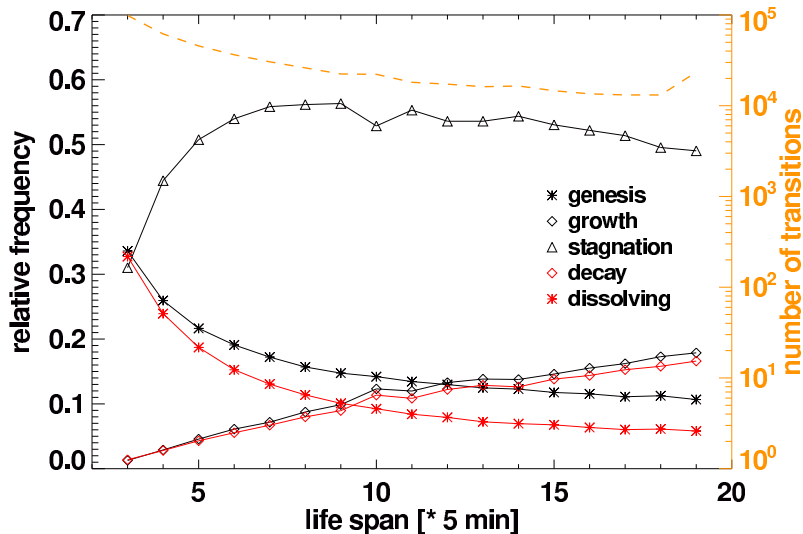


**Figure 2.9:** Growth processes with respect to life span for the *transition-based approach*. The dashed orange line gives the total number of transitions observed for each life span.

Altogether, most frequent transitions in both approaches are stagnations, followed in number by genesis (WEUSTHOFF AND HAUF 2008b). In the *transition-based approach*, genesis, growth, decay and dissolving show nearly the same frequency. In the *cluster-based approach*, however, decay and dissolving occur less frequently than genesis and growth. This is obviously due to the fact that in the cluster-based approach just one transition process is counted for splitting, while merging includes one transition process for each cluster involved.

Figure 2.9 shows a plot of the relative frequencies of transitions with respect to the life span of the tracks in which they are occurring (*transition-based approach*). Stagnation clearly dominates the growth process for all life spans. Genesis and dissolving represent the second most frequent transition processes for life spans up to  $l \approx 10 * 5$  min, whereas for longer life spans, growth and decay are more frequent. While the latter two occur nearly equally frequent, there is a marked difference between genesis and dissolving. This difference means that more clusters are generated than do disappear and leads to the assumption that merging is more frequent than splitting. Thus, when two clusters combine and this combined cluster disappears, there were two clusters generated in that track, but only one is disappearing. This was in fact observed in the cluster-based approach (WEUSTHOFF AND HAUF 2008b). About 28 % of all clusters were found to grow within a time step of 5 min, with 75 % of the cases being merging processes. Thus, growth is nearly twice as frequent as decay which occurs for 16 % of all clusters, with only 55.5 % of the cases caused by splitting.

Based on observed transition probabilities for the transitions from an  $n$ -cell cluster to an  $m$ -cell cluster (*transition-based approach*), a simple growth model was proposed which describes the incremental growth by one cell within a time step (see Figure

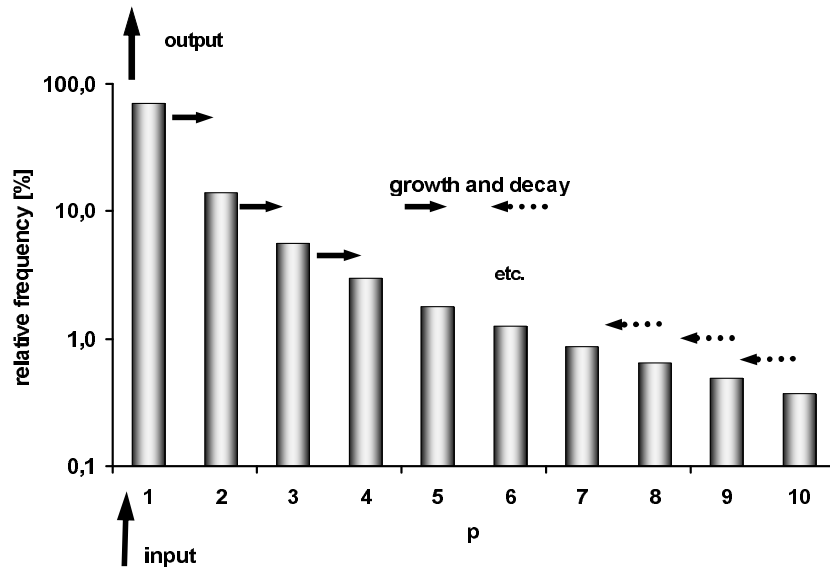


**Figure 2.10:** Simplified growth of the cluster growth process (WEUSTHOFF AND HAUF 2008b). Displayed is the frequency distribution of the cell number  $p$ , the arrows indicate growth and decay processes. A cluster preferably forms as single cell, grows and decays by one cell within a time step and finally disappears via the single-cell-stage.

2.10). Clusters form as single cells, grow by gaining one additional cell within each time step and decay accordingly preferably by one cell before they finally disappear via the single-cell-stage again. Within the growth process, a phase of stagnation may appear where the cell number stays constant. The basic model neglects the fact that larger clusters may generate first or that cells grow by more than one cell within a time step.

As stated in WEUSTHOFF AND HAUF (2008b), the growth mechanism of shower cells, deduced from observed transition frequencies, was found to fit the general properties of a Yule process (CONCAS ET AL. 2006). The key element of this process is that entities increase their property at each time step with a certain probability in proportion to the size of this property. According to that hypothesis, new shower cells would preferably grow in direct vicinity of existing cells, which would subsequently merge, or within already existing clusters. The existence of preferred locations for the formation of new shower cells has not been investigated so far. A test of the hypothesis is therefore left for further studies.

## 2.2 Weather Radar

As the analysis is mainly based on radar data, Section 2.2.1 gives a short introduction into the basic principles of radar measurements. For more detailed information the reader is referred to BATTAN (1973) and SAUVAGEOT (1992). In Section 2.2.2, the

## Chapter 2. Background

---

German radar network and the radar products of the DWD are introduced. The Z-R-relationship, as the common way of quantitative precipitation estimation by means of radar measurements, is addressed in Section 2.2.3. Finally, the problems of radar measurements are discussed in Section 2.2.4.

### 2.2.1 Radar principles

The weather radar is a ground based remote sensing instrument used for the detection of precipitation. RADAR stands here for **R**adio **D**etection **A**nd **R**anging. A radar station basically consists of a transmitter-receiver antenna and a protecting radome. The measurement is based on the principle that electromagnetic waves are propagated through the atmosphere at the speed of light ( $c \approx 3 \cdot 10^8 \text{m/s}$ ) and along straight lines. The directional antenna sends a narrow beam of pulsed microwave signals of known wavelength  $\lambda$  and duration  $\tau$ . The frequency with which radar pulses are emitted is given by the pulse-repetition frequency (PRF). The latter determines the maximum range  $r_{max}$  up to which radar measurements can be performed unambiguously:

$$r_{max} = c/2PRF \quad (2.1)$$

All types of targets present in the beam, such as hydrometeors, but also insects and birds, absorb the incident energy and radiate in different directions. Thus, a fraction of the energy is reflected and returns to the antenna. The runtime of the reflected signal gives information on the distance to the precipitation particles, while the strength of the signal gives hints on size and composition of the target. The capability to measure a specific type of hydrometeor is given by the wavelength. C-band radar stations, which are usually used for precipitation measurements, have a wavelength of 7.3 - 3.75 cm. Shorter wavelengths are applied for smaller particles, such as K-Band (2.4 - 0.75 cm) for cloud droplets.

Radar measurement is a volume measurement, i.e. the radar station captures backscatter of energy from a measuring volume which increases in size with increasing distance. The radar equation for volume targets assigns the received power  $P_r$  to the radar reflectivity factor  $Z$  (GEKAT ET AL. 2003):

$$P_r = C \cdot Z \cdot \frac{|k|^2}{r^2} \quad (2.2)$$

Here,  $r$  is the distance to the target,  $|k|^2$  is a factor depending on the state of aggregation (0.93 for water, 0.21 for snow) and  $C$  is a radar constant, including all radar station specific technical factors (e.g. wavelength, transmitted peak power at the antenna etc.). The reflectivity factor  $Z$  apparent in Equation 2.2 results from the radar reflectivity  $\eta$  under the assumption of the validity of Rayleigh scattering. The radar reflectivity  $\eta$  is the sum of the radar backscattering cross sections  $\sigma_i$  of

## Chapter 2. Background

---

the individual particles over the unit volume  $V$  (one cubic meter):

$$\eta = \frac{1}{V} \sum_V \sigma_i \quad (2.3)$$

$$= \int_{D_{min}}^{D_{max}} \sigma(D) \cdot N(D) \cdot dD \quad (2.4)$$

In this equation,  $D$  is the diameter of the particles in the volume and  $N(D)$  is the size distribution of the particles. The reflectivity  $\eta$  is a characteristic value for the size of the target and its definition includes no assumptions on the nature of the backscattering medium. Only by assuming the validity of Rayleigh scattering, i.e. when precipitation particles are small compared to the radar wavelength, the target is specified over the backscattering cross section:

$$\eta = \frac{\pi^5}{\lambda^4} \cdot |k|^2 \int_{D_{min}}^{D_{max}} D^6 \cdot N(D) \cdot dD \quad (2.5)$$

The radar reflectivity  $\eta$  is proportional to the radar reflectivity factor  $Z$ ; the latter is given by the expression behind the integral.

$$\eta = \frac{\pi^5}{\lambda^4} \cdot |k|^2 \cdot Z \quad (2.6)$$

$$Z = \int_{D_{min}}^{D_{max}} D^6 \cdot N(D) \cdot dD \quad (2.7)$$

$$\propto D^6 \quad (2.8)$$

As the reflectivity depends on the sixth power of the diameter of the drops, large hydrometeors dominate the precipitation signal.

The reflectivity factor is usually given in units of dBZ, where dB stands for decibel and  $Z$  is the radar reflectivity factor. The decibel is a logarithmic measure for the relation of two energy parameters ( $P(\text{in dB}) = 10 \log_{10} P_i / P_o$ ).

$$Z(\text{in dBZ}) = 10 \log_{10} \left[ \frac{Z(\text{in } mm^6 m^{-3})}{mm^6 m^{-3}} \right]. \quad (2.9)$$

Besides the conventional radar reflectivity measurements, modern radar systems, namely doppler radar and polarimetric radar, provide additional information on the targets. With a doppler radar, the radial velocity can be measured by means of frequency shift due to the Doppler effect. Polarimetric radars are capable of determining the shape of the drops by using two pulses with orthogonal polarization. This additional knowledge gives the possibility to differentiate precipitation types and, thus, to improve the rainfall estimates (ILLINGWORTH 2003). Furthermore, both radar types can improve the recognition of ground clutter.



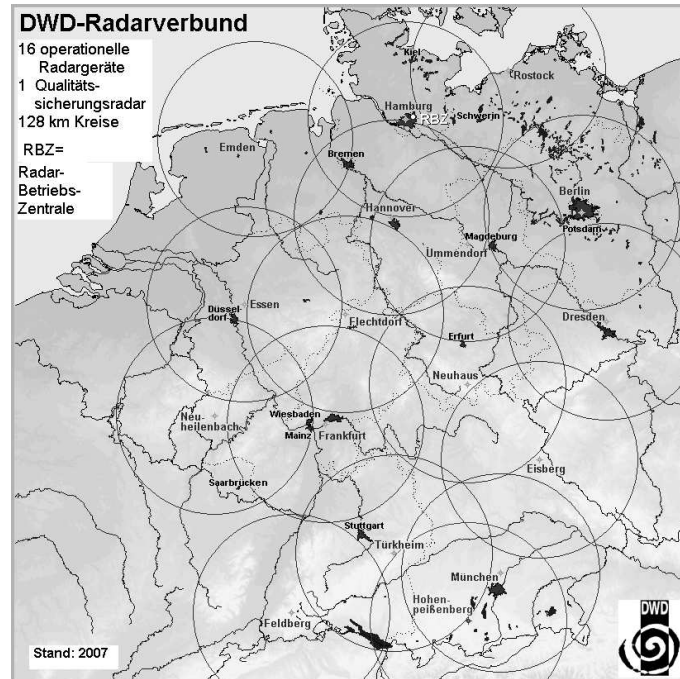


**Figure 2.11:** Map of the 16 radar stations of the German radar network (plus research radar at Meteorologisches Observatorium Hohenpeißenberg) with 128 km horizontal range. Source: DWD.

### 2.2.2 German radar network

The German Weather Service's (DWD) radar network comprises 16 C-band radar stations (wavelength = 5 cm, 5600 - 5640 MHz) of Doppler type covering the whole of Germany and parts of the surrounding countries. Figure 2.11 shows the radar stations with operating ranges of 128 km. Each radar station is operated in two different scan modes: the *volume scan* and the *precipitation scan* (SCHREIBER 1998). In the *volume scan*, the atmosphere is scanned every 15 minutes with 18 different elevations ranging from  $37.0^\circ$  to  $0.5^\circ$ . The volume scan comprises again two different modes: the *intensity mode*, for elevations from  $0.5^\circ$  to  $4.5^\circ$  has a horizontal range of 230 km, the *doppler mode*, covering elevations above that, ranges 120 km. Every 5 min the volume scan is halted to start the *precipitation scan* which provides the instantaneous values of the latest precipitation echoes in almost real time. Depending on the orography, the atmosphere is hereby scanned with an elevation of  $0.5^\circ$  and  $1.8^\circ$  and a horizontal range of up to 128 km.

### Radar products

From the different radar products available at the DWD, only those relevant for the present work are introduced. These are plan-position indicator (PPI) products which display a plan view of received signals on a polar coordinate system based

## Chapter 2. Background

---

on azimuthal antenna scans. Other available products, which were not used in this analysis, provide information on the vertical structure, such as the range-height indicator (RHI) where the antenna scans vertically, and the constant-altitude plan-position indicator (CAPPI) which gives signals calculated to constant altitudes. Additional information on the DWD's radar products can be found in SCHREIBER (1998) or in the *Radarbroschüre* available on the DWD's Websites ([www.dwd.de](http://www.dwd.de)).

The local radar product **PL** results from the volume scan providing every 15 min the nearest surface radar echoes in six reflectivity classes. The maximum scanning distance is 230 km, the horizontal resolution 2 km x 2 km. The PL products from all radar stations are merged to the national composite **PC**. In the overlap region of different radar stations, the strongest signal is taken. Based on that composite, THEUSNER (2007) analysed the geometrical structure of the post-frontal precipitation field.

The precipitation scan is used to produce the local **DX** products, which contain the current values of the latest precipitation echoes measured every 5 min. The horizontal resolution is 1 km x 1 km. The composite generated from the local DX products is the **RX**-composite. In overlap regions of two radar stations, the value which is nearer to the ground is used. The RX composite contains radar reflectivities encoded in so-called *RVP-6-Units* with a resolution of 0.5 dBZ. The measurement range runs from 0 to 255 RVP-6-Units, which can be converted to reflectivities by means of Equation 2.10.

$$\frac{RVP - 6 - Units}{2} - 32.5 = dBZ - Value \quad (2.10)$$

Thus, the measurement range covers reflectivities from -32.5 dBZ to +95 dBZ. The use of the RVP-6-Units has the advantage that negative dBZ values, occurring for low reflectivities, are avoided and that more information is conserved compared to a direct conversion to dBZ values.

The quantitative **RZ** composite, which is used for this thesis, is described in the following Section 2.2.3.

### 2.2.3 Quantitative precipitation estimation

Besides the spatial information gained by radar reflectivity measurements, the quantitative precipitation measurement by radar is of great interest. Therefore, the measured reflectivity values need to be converted into rain rates. This is usually done with the so called Z-R-relationship which is an empirically derived relationship between the measured radar reflectivity  $Z$  [ $\text{mm}^6\text{m}^{-3}$ ] and the correspondent rain rate  $R$  [ $\text{mmh}^{-1}$ ] and was first proposed by MARSHALL AND PALMER (1948):

$$Z = a \cdot R^b. \quad (2.11)$$

For the two constants  $a$  and  $b$ , a huge number of different values have been derived mainly by measurements of drop-size distributions as a function of precipitation

## Chapter 2. Background

---

intensities. The constants vary largely for different synoptic situations, regional characteristics and implicitly assumed rain drop size distributions. They essentially depend on whether precipitation is convective or stratiform. The problem is extensively discussed by BATTAN (1973), who gives a comprehensive list of values reported by different authors, and SAUVAGEOT (1992). Because of the large number of different constants, the restriction to a general Z-R-relationship cannot satisfy all purposes (BEHENG 1998). The German Weather Service uses with the standard relationship ( $a = 256$  and  $b = 1.42$ ) a mean Z-R-relationship of those found for convective and for stratiform precipitation events (see Figure 2.12). This leads, however, to an overestimation of convective and an underestimation of stratiform precipitation intensities (BARTELS ET AL. 2004).

In the framework of the project RADOLAN (BARTELS ET AL. 2004), an advanced Z-R-relationship was established which distinguishes stratiform and convective precipitation based on reflectivity values and a shower index  $\bar{\Delta}$ . With the resulting five different relationships (see Table 2.1, Figure 2.12), the reflectivity values of the RX composite are converted into rain rates, resulting in the **RZ** composite which constitutes the basic data material for the present analysis. The RZ composite contains rain rate values in steps of 0.01 mm per 5 min. It has a spatial resolution of 1 km x 1 km and a temporal resolution of 5 min.

According to BARTELS ET AL. (2004), the advanced Z-R-relationship has a positive impact on the quantitative precipitation estimation. However, the errors due to the variability of the drop size distribution may still be large (LEE AND ZAWADZKI 2004) and need to be kept in mind when radar data is used quantitatively. A common way to improve the quantitative precipitation estimation is the adjustment to rain gauge data (GJERTSEN ET AL. 2004), which is usually done for larger time intervals from one hour to 24 hours. EHRET (2002) proposed a statistical method where the spatial variability of the radar image is imprinted on the interpolated field from rain gauges with respect to the field mean (ordinary kriging). First quality investigations reveal a superiority of adjusted radar rainfall estimates based on this method over the unadjusted ones. The evaluation was done for a small catchment and by cross-validation as well as by runoff-simulations (HEISTERMANN (2008), <http://www.wrah-2008.com/PDF/O2-008.pdf>).

The German Weather Service applies an adjustment to rain gauges for example to the hourly precipitation sum composites both offline and in real-time, resulting in the **RW** composite (BARTELS ET AL. 2004). For smaller time scales, this adjustment is restricted by the displacement velocity of rain events and the spatial and temporal representativeness of the ground measurement. However, although the RZ composite might not be the best quantitative radar product, it is the most adequate for the purpose of this study because of the 5 min time resolution. A short discussion on the quality of the RZ composite is given in Chapter 3.1.2.

## Chapter 2. Background

---

dBZ	< 36.5			36.5 ... 44	> 44
$\bar{\Delta}$	< 3.5	3.5 ... 7.5	> 7.5		
$a$	125	200	320	200	77
$b$	1.4	1.6	1.4	1.6	1.9

**Table 2.1:** Parameters  $a$  and  $b$  in Equation 2.11 of the advanced Z-R-relationship for three reflectivity classes defined by BARTELS ET AL. (2004). For low reflectivities an additional discrimination based on the so-called shower index  $\bar{\Delta}$  is given.

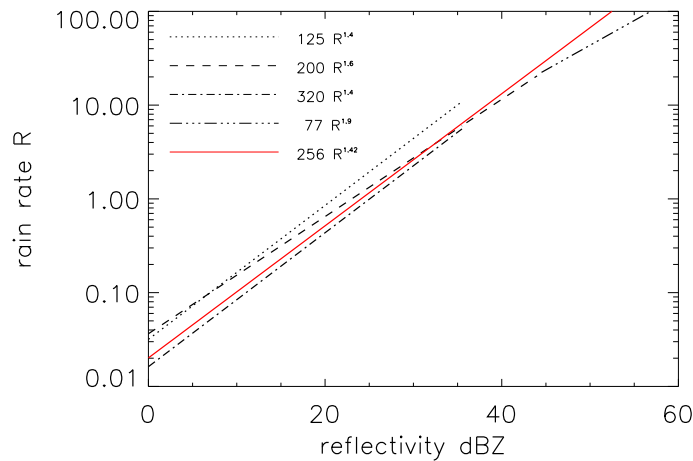


**Figure 2.12:** Advanced Z-R-relationship of the project RADOLAN (black lines) and the standard Z-R-relationship (red).

### 2.2.4 Error sources

Radar measurements have the great advantage of a high spatial and temporal resolution in combination with a large coverage range, but also exhibit certain constraints. Especially when using those measurements to estimate quantitative precipitation, the quality is limited due to various error sources. More details on the principles of quantitative rainfall estimation and the related uncertainties can be found e.g. in the review of JOSS AND WALDVOGEL (1990) or in SAUVAGEOT (1992) and SÁLEK ET AL. (2004). The relative importance of various kinds of uncertainties are discussed in AUSTIN (1987) on the basis of several case studies. Three types of uncertainties are introduced in the following.

The first type deals with the conversion from measured radar reflectivities into precipitation rates, which is usually done by an empirical Z-R-relationship as introduced in Section 2.2.3. That relationship depends strongly on the drop size distribution and varies largely with space and time. There is no unique relationship between

## Chapter 2. Background

---

radar reflectivity and rain rate and assuming such a relationship provides an uncertainty in the precipitation amount. Thus, the natural variability in drop size distributions is an important source of uncertainty in radar measurements of precipitation (JOSS AND WALDVOGEL 1990).

Another error source is the vertical variability of radar reflectivity (CHUMCHEAN ET AL. 2003). A change of the nature or intensity of precipitation with height, for example caused by orographic enhancement, creates a vertical varying reflectivity profile. This variability causes a range dependent bias in radar rainfall estimation (JOSS AND WALDVOGEL (1990), SMITH ET AL. (1996)). SALTIKOFF ET AL. (2004) identified the vertical dBZ profile as one of the most important challenges concerning radar quality issues for the Northern European countries.

Uncertainties of a third type are related to instrumental considerations, i.e. errors in the measurements of radar reflectivity itself (JOSS AND WALDVOGEL 1990). This includes ground clutter and attenuation as well as the hardware of the radar system. Some of those problems can be dealt with logistically, for example through changes of infrastructure or the radar scan strategy (SALTIKOFF ET AL. 2004).

### Clutter correction

The term clutter refers to echoes returned from fixed targets without meteorological content and is basically caused by orography (ground clutter) and anomalous propagation of the radar beam (anaprop) as a special case of ground clutter (SÁLEK ET AL. 2004). Besides a modification of the spatial structure, clutter has also a strong impact on quantitative precipitation estimation as its signal can be much more intense than that of meteorological targets. Several methods exist to detect and delete clutter from measured radar data, such as statistical techniques, the Doppler-method or a clutter-map (static or dynamic). The different methods are discussed, for instance, in SELTMANN (1997), GERMANN AND JOSS (2003) and SÁLEK ET AL. (2004). It is, however, impossible to remove clutter completely without changing the meteorological information. The elimination of clutter may cause new problems concerning radar applications. Resulting holes limit the use of tracking and extrapolating techniques based on radar data (GERMANN AND JOSS (2003), MECKLENBURG (2000)). The same is true for shielding, i.e. the blocking of the radar beam by buildings or orography causing a lack of radar information behind that object (see Figure 2.13). Those problems especially arise in mountainous regions as the graphic reveals.

For the RZ composite, the measured radar reflectivity is clutter-corrected by means of statistical clutter filtering and doppler filter (BARTELS ET AL. 2004). Elimination of clutter shall be enhanced in the quality improved **RY** composite, which was unfortunately not available for the investigated dates.

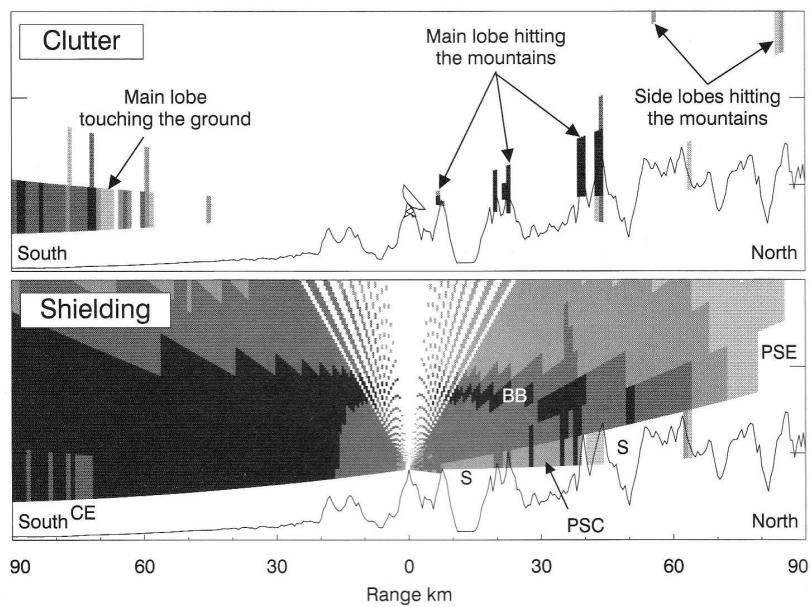


**Figure 2.13:** Vertical cross section (0 to 6 km above sea level) of a radar station in a mountainous region, displaying the radar error sources clutter and shielding (GERMANN AND JOSS 2003). The top figure represents intensity of ground echoes during clear weather without clutter elimination. In the bottom figure, a 24 h accumulation of stratiform precipitation illustrates the problem of shielding. To the north, for example, the lowest elevations are blocked at a range of 8 and 44 km; everything behind is shielded (S). More detailed information can be found in GERMANN AND JOSS (2003).

# Chapter 3

## Data

The data set comprises basically the radar data, namely the 5 min RZ composite, and the *character*-files containing all information on the individual clusters as well as the tracking information from the previous study by WEUSTHOFF AND HAUF (2008b) for 17 days with post-frontal showers. In Section 3.1.1, the processing of the radar data is described, followed by a short discussion on the data quality in Section 3.1.2. Section 3.2 introduces the concept of *tracks* as the basic data needed to describe the characteristics of individual clouds in the course of their life. The latter will be presented in Chapter 6.

### 3.1 Radar data

While the basic principles of radar measurement and the radar products of the DWD were addressed in Section 2.2 including an introduction to the RZ composite in Section 2.2.3, the explicit data processing procedures and the data quality are described in the following sections.

#### 3.1.1 Data processing

The analyses for the current thesis are based on the quantitative radar composite RZ, which was introduced in Section 2.2.1. For 17 days in 2004 and 2006, listed in Table 3.1, the 5 min RZ composite data of the whole day was analysed, in total 288 files for each day. On two days, consecutive data was only available from 09 UTC (25 February 2004, resulting in 180 files), respectively from 06 UTC (21 March 2004, resulting in 216 files). Due to temporarily missing data from a single radar site or sometimes even from the whole radar network, some additional data gaps were present. The data was processed following the method described in WEUSTHOFF

## Chapter 3. Data

---

Year	Month	Day	Number of clusters	$p_{\max}$	
2004	February	25. (from 09 UTC)	24 000	48	
	March	21. (from 06 UTC)	43 000	105	
	May	23.	51 000	82	
	June	12.	58 000	106	
	July		10.	64 000	60
			12.	70 000	74
			13.	88 000	289
	August		26.	118 000	161
			31.	72 000	160
24.			112 000	248	
2006	January	21.	70 000	440	
	March	01.	64 000	85	
		02.	71 000	70	
		05.	39 000	180	
		06.	85 000	90	
		07.	70 000	110	
	November	09.	48 000	67	

**Table 3.1:** List of analysed days together with the total number of clusters detected on each day (rounded to full thousands) and the maximal cell number occurring within a cluster  $p_{\max}$ .

AND HAUF (2008b). In a first step, the post-frontal shower area was extracted and rain rate values below a cut-off of 0.05 mm per 5 min were eliminated. That threshold was chosen as THEUSNER (2007) found in a previous study a reflectivity value of 19 dBZ being sufficient to detect the convective structures within the precipitation field. Calculated with the standard Z-R-relationship (Equation 2.11), a rain rate of 0.05 mm per 5 min corresponds to a radar reflectivity value of about 20 dBZ.

The extracted radar data was then labelled. This means, each cluster which is defined as a contiguous rain area in the radar data was continuously numbered for each day. This way, a cluster can be unambiguously identified by date and number. The characteristics of all clusters were stored in an hourly data file (*character\_yymmddhh00.txt*); an example of such a file is given in Figure 3.1. The column numbers start with 0 as displayed in the first line. In column 0, the time is displayed, followed by the label number in column 1 and the cluster's characteristics in the subsequent columns. Among them are the cluster size (2), the number of embedded cells (3), the area integrated rain rate (5), the  $x$ - and  $y$ -value of the centre of the encompassing ellipses (7 and 8) and information about the tracking, e.g. precursor (18) and successors (19 - end). The tracking procedure will be addressed in Section 3.2. Finally, the basic data set for each day consists of the extracted 5 min radar data (288 in total) and the character-files (24 in total). All presented



## Chapter 3. Data

0	1	2	3	4	5	6	7	8	9	10	11	12	13	14	15	16	17	18	19
1015	1631	16	1	9	154	11	442	134	6047	0	0	0	0	0	0	0	0	1102	0
1015	1632	14	2	7	105	11	462	135	6573	0	0	1	7	171	0	0	0	0	2116
1015	1633	5	1	17	86	33	593	134	6117	0	0	0	3	108	0	0	0	0	2128
1015	1634	7	1	7	51	8	664	133	6046	0	0	0	3	123	0	0	0	1100	2129
1015	1635	5	1	14	70	22	516	134	5698	0	0	0	1	90	0	0	0	0	2131
1015	1636	26	1	22	574	50	543	137	5698	0	0	2	9	251	0	0	0	1098	2127
1015	1637	18	1	7	131	9	415	139	4695	0	0	0	2	63	0	0	0	1103	2140
1015	1638	11	1	9	107	20	658	138	6194	0	0	0	3	71	0	0	0	0	2137
1015	1639	5	1	52	263	72	518	137	5698	0	0	1	16	100	0	0	0	1105	2127
1015	1640	11	1	8	93	12	689	139	6048	0	0	0	4	104	0	0	0	1104	2138
1015	1641	1374	41	20	27785	103	466	138	6573	0	0	2	20	0	0	0	0	1108	2135
1015	1642	59	2	12	759	32	553	142	5698	0	0	2	2	116	0	0	0	1098	2141
1015	1643	4	1	13	55	18	522	140	5698	0	0	1	13	116	0	0	0	1109	2127
1015	1644	280	4	41	11655	223	671	160	5367	0	0	2	16	201	0	0	0	1110	2147
1015	1645	6	1	11	66	17	543	145	5698	0	0	0	2	135	0	0	0	1098	2144
1015	1646	5	1	8	43	12	500	146	6573	0	0	0	0	0	0	0	0	1108	0
1015	1647	19	1	10	195	15	448	147	6573	0	0	1	21	58	0	0	0	0	2135
1015	1648	7	1	18	126	26	685	148	6120	0	0	0	3	108	0	0	0	0	2149
1015	1649	33	2	14	469	37	542	153	6573	0	0	0	3	108	0	0	0	1112	2150
1015	1650	12	1	29	356	46	342	151	6570	0	0	0	2	116	0	0	0	1114	2151
1015	1651	13	2	10	141	14	651	153	5987	0	0	1	19	222	0	0	0	1111	2119
1015	1652	4	1	8	32	9	691	151	6050	0	0	0	0	0	0	0	0	1113	0
1015	1653	7	1	8	61	11	500	153	5768	0	0	0	2	135	0	0	0	1117	2153
1015	1654	13	1	11	150	21	695	155	5770	0	0	0	0	0	0	0	0	1119	0
1015	1655	29	1	15	443	44	708	156	5766	0	0	0	2	90	0	0	0	1118	2155

**Figure 3.1:** Example of a *character*-file containing in the columns time (0) and cluster label (1) as well as characteristics of the individual clusters (2-6) and information on their location (7 and 8), precursor (18) and successors (19-end).

analyses are based on this information.

### 3.1.2 Radar data quality

As the analysis is completely based on the RZ composite, the limitations of the latter should be kept in mind. As mentioned before, the main advantage of precipitation measurement by weather radar is the measurement over a large range with a high temporal and spatial resolution. The resulting data provide a coherent image of the spatial precipitation structure. An important disadvantage, however, is certainly the quantitative aspect. Measured radar reflectivities can be converted into rain rates using for example an empirical Z-R-relationship. The quality of those rain rate values is a problem due to various error sources which are discussed in Section 2.2.1. Direct measurements by rain gauges, in contrast, allow a precise determination of the rain amount, but they have the problem of spatial representativeness. Rain gauge measurements are point measurements of the surface precipitation, and interpolation and regionalisation is necessary to get the spatial structure of the precipitation field. The best procedure is to combine the spatial structure of radar measurement with the good quality point measurements of rain gauges (*adjustment*), as it is done, for example, at the DWD on an hourly basis (see Section 2.2.3).

For the purpose of tracking individual clusters over time, the 5 min RZ composite is the most applicable product, although it is not calibrated by rain gauge measurements. Instead, precipitation is calculated with an advanced Z-R-relationship using five different Z-R-relationships depending on the reflectivity values and the

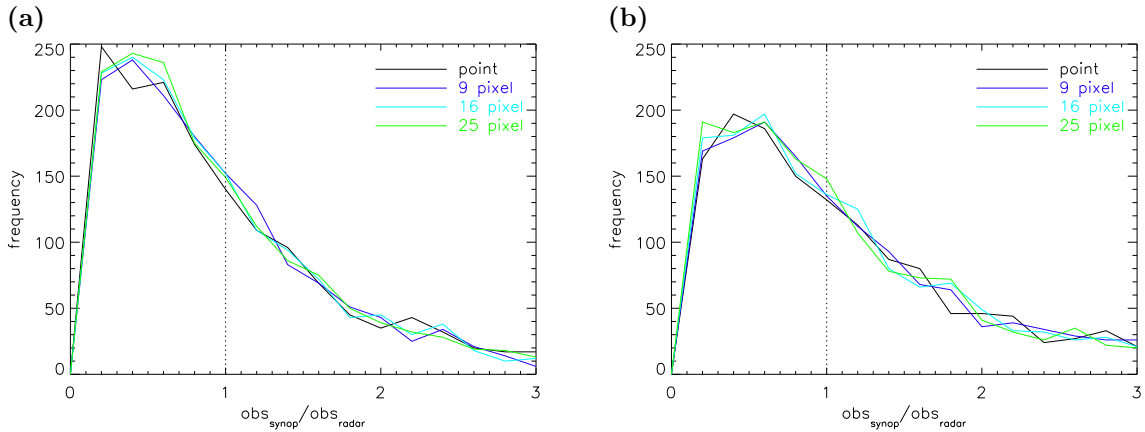


**Figure 3.2:** Frequency distribution (absolute values) of the ratio of daily sums from synoptical observations ( $obs_{synop}$ ) and derived by radar ( $obs_{radar}$ ) for a single pixel closest to the station (point) as well as with precipitation sums averaged over 9, 16, and 25 pixels around the station location. The ratio displayed in (a) includes all radar derived rain rates while in (b) only values larger than 0.05 mm per 5 min are considered.

shower index (see Chapter 2.2.3), which presumably has a positive impact on the quantitative precipitation estimation. HEUEL (2004) investigated different methods to estimate precipitation amounts based on radar measurements and found that the error could be reduced when different Z-R-relationships are used for convective and stratiform rain events. In that study, the error reduction reached up to 20 % for an automatically differentiation and even 48 % if this differentiation was done manually. In another study, MARX (2007) compared three different Z-R-relationships, (a) the standard form, (b) the improved Z-R-relationship by BARTELS ET AL. (2004) and (c) a new Q-Z-R-relationship calibrated with runoff measurements and simulations with data of six different rain gauge stations. It was found that, for hydrological modelling, (b) has already improved the quality of runoff-simulations while (c) performs best in this comparison. All three relationships lead to an underestimation of high rain intensities.

To get an idea of the quality of the radar derived rain rates for the investigated post-frontal shower events, the pixel-wise daily sums were compared to 24 h rain gauge measurements. The comparison was done only for 15 of the 17 days, as the radar data for two days were incomplete (25 February and 21 March 2004, cf. Table 3.1). For about 150 synoptic observation stations distributed over all of Germany, the hourly sums were accumulated to daily totals. For a comparison of these station measurements ( $obs_{synop}$ ) with the radar derived precipitation sums ( $obs_{radar}$ ) at a single pixel closest to the station as well as with precipitation sums averaged over 9, 16, and 25 pixels around the station location, the respective quotients were calculated ( $obs_{synop}/obs_{radar}$ ). A quotient of 1.0 would indicate a perfect fit, values below 1.0 indicate an overestimation by radar and values larger than 1.0 an underestimation by radar, assuming that the synoptic observations give the true precipitation

amounts. Due to the limitations of both instruments and the problems concerning their comparability (ground based vs. remote sensing instrument), certainly no perfect agreement is expected. The frequency distributions of the ratios are displayed in Figure 3.2 (a), including all radar derived rain rates, and in Figure 3.2 (b) considering only those rain rates with values of more than 0.05 mm per 5 min. Obviously, the radar overestimates the precipitation amount which is indicated by the peak at a ratio of approximately 0.40 in both figures. This value lies in between those reported by PAULAT (2007), who analysed radar data for the period of 2001 - 2004 by means of the PC composite. The rain rates in that study were calculated from measured radar reflectivities by means of the standard Z-R-relationship (Equation 2.11). PAULAT (2007) found that the overestimation by radar was larger in summer with a ratio value of 0.35 than in the other seasons with a ratio of 0.45. The peak value identified in the present study without season distinction represents the average of those two values. A truncation of rain rate values below 0.05 mm per 5 min leads obviously to a less distinct peak and generally lessens the overestimation of the daily rain sum by radar.

The frequency distribution shows a decrease towards larger values of the ratio  $obs_{synop}/obs_{radar}$ . Less than 40 % of the radar derived precipitation sums revealed an underestimation with ratio values  $> 1$ . Including only values larger than 0.05 mm per 5 min, overestimation and underestimation become more balanced with about 45 % of the ratios revealing values larger than 1. A value of approximately 1 was obtained in both cases for 8 % of the calculated ratios.

Concerning the different methods of comparison, averaging yielded slightly better results than the comparison with values from only one pixel, regardless over which number of surrounding pixels the average was calculated.

## 3.2 Tracks

### 3.2.1 Definition

Based on the 5 min radar composite, a tracking of individual clusters was performed. The procedure in use combines various methods such as correlation analysis and individual tracking. A detailed description can be found in WEUSTHOFF AND HAUF (2008b). Altogether, on the 17 analysed days, a total of over 81 000 tracks could be identified, which form the basis for the present analysis, in particular for the investigation of the clusters' life cycle. A track is hereby defined as the whole set of clusters that belong together such that they are precursors or successors of each other. As mentioned before, the precursors and successors of a cluster are stored in the *character*-file (see example in Fig. 3.1). Each track has a specific life span  $l$  which is the time from the genesis of the first cluster of the track until the disappearance of the last member of the track. A cluster has to be tracked at least once to be referred to as a track. The minimum life span is consequently 15 min,

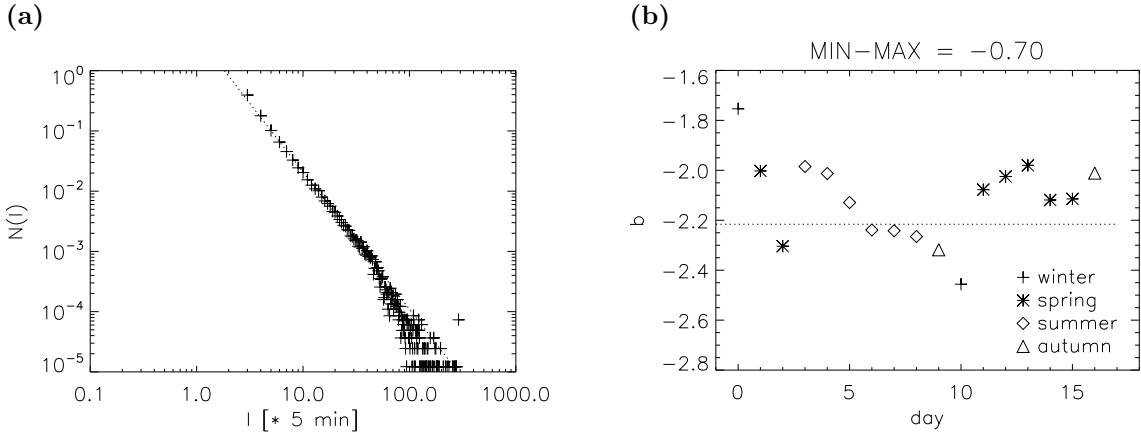


**Figure 3.3:** (a) Frequency distribution of the tracks' life span fitted by a power law (Equation 3.1,  $N(l)$  = relative frequency) and (b) day-to-day variation of the coefficient  $b$ . The two days furthest away from the mean (day 0 and day 10) are the winter days.

as each transition process is assigned to a 5 min time interval (e.g. genesis, growth, dissolving). About 10 % of all clusters have neither precursor nor successor, they could not be tracked and thus have a life span of just ten minutes comprising genesis and dissolving. They are not included in the track analysis.

The frequency distribution of the life span  $l$  for all tracks is displayed in Figure 3.3 (a). It can be described by a power law of the form

$$N(l) = a \cdot l^b \quad (3.1)$$

with  $N(l)$  being the relative frequency,  $a = 3.94$  and  $b = -2.28$  and a correlation value of  $\mathcal{R} \cong 1.00$  (cf. Table 3.2). The negative value of the parameter  $b$ , which is the slope in the double logarithmic representation, indicates that the short life spans are dominant. About 80 % of the tracks have a life span of 15 to 35 minutes. LÓPEZ ET AL. (1983) found that even 90 % of the cells have a duration of less than 20 minutes. In this number were also those cells included that could not be tracked and thus have a duration of only 10 minutes. As stated above, those clusters are not included in the present study as they are no tracks by definition.

The parameter  $b$  of the frequency distribution shows a day-to-day variation which is displayed in Figure 3.3 (b). With the exception of two days, the variations are quite low. Those two days are the winter events: 25 February 2004 (day 0) and 21 January 2006 (day 10). They show opposed deviations, i.e. while on day 0, less short living tracks were observed, more short life spans were found on day 10. However, for an elaborate sensitivity study regarding the influence of the season on the results, the number of considered days is too low. Such an analysis is therefore left for subsequent studies with more observation days.

### 3.2.2 Track types

For a determination of the time series with respect to area integrated rain rate and cluster size, the tracks were grouped into three categories:

1. Single-cell-tracks (53 500 tracks = 66 %, see Figure 3.4 (a))  
 Clusters that remain single cells over their whole life time. This means, growth occurs only with respect to the area and the rain rate, but not with respect to the number of cells within the cluster.
2. Single-cluster-tracks (10 500 tracks = 13 %, see Figure 3.4 (b))  
 Clusters which develop only by internal growth and decay are called single-cluster-tracks. They have no interaction with other clusters, but the number of embedded cells varies.
3. Multi-cluster-tracks (17 000 tracks = 21 %, see Figure 3.4 (c))  
 Multi-cluster-tracks are all those tracks where interactions among clusters occur, namely merging and splitting. Those tracks often have a long duration and a rather complex life cycle.

In Appendix A, three examples of each track type with different life spans are presented to show the variety of possible developments. For each of those track types, the mean time series of the cluster size and the area integrated rain rate will be determined over each respective life span. The investigations concerning single-cell-tracks are published already in WEUSTHOFF AND HAUF (2008a). Together with the two other track types, the results will be presented in Chapter 6.

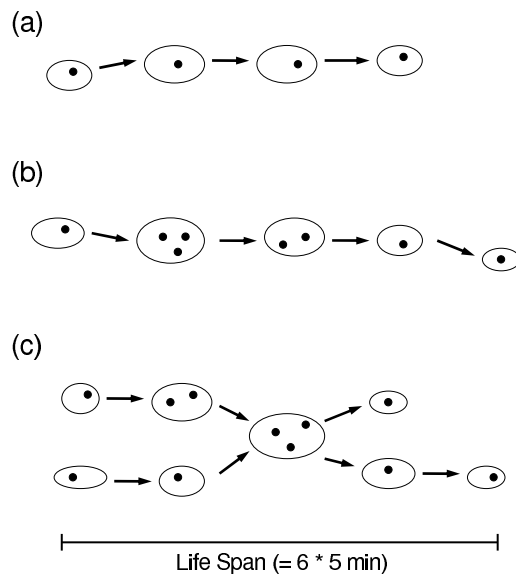


**Figure 3.4:** The three different track types: (a) single-cell-tracks, (b) single-cluster-tracks and (c) multi-cluster-tracks.

## Chapter 3. Data

The life span distributions of the individual track types, as displayed in Figure 3.5 (a) in a linear representation, can be fitted to a power law (Equation 3.1). They are plotted together with the frequency distribution of all tracks' life spans in Figure 3.5 (b) in a double-logarithmic presentation. The respective parameters and the correlation coefficients are given in Table 3.2. Although the correlation coefficients are quite high for all three track types, a closer look reveals that single-cluster-tracks and multi-cluster-tracks are better described by a modified power law (Figures 3.5 (c) and (d), Equation 3.2). The coefficients of the equation and the correlation coefficients can be found in Table 3.3. The modified power law yields correlation coefficients of more than 0.99 for the two track types.

$$N(l) = c_2 \cdot l^{d_2} \cdot \left(1 - c_3 \cdot l^{d_3} - \frac{c_4}{l}\right) \quad (3.2)$$

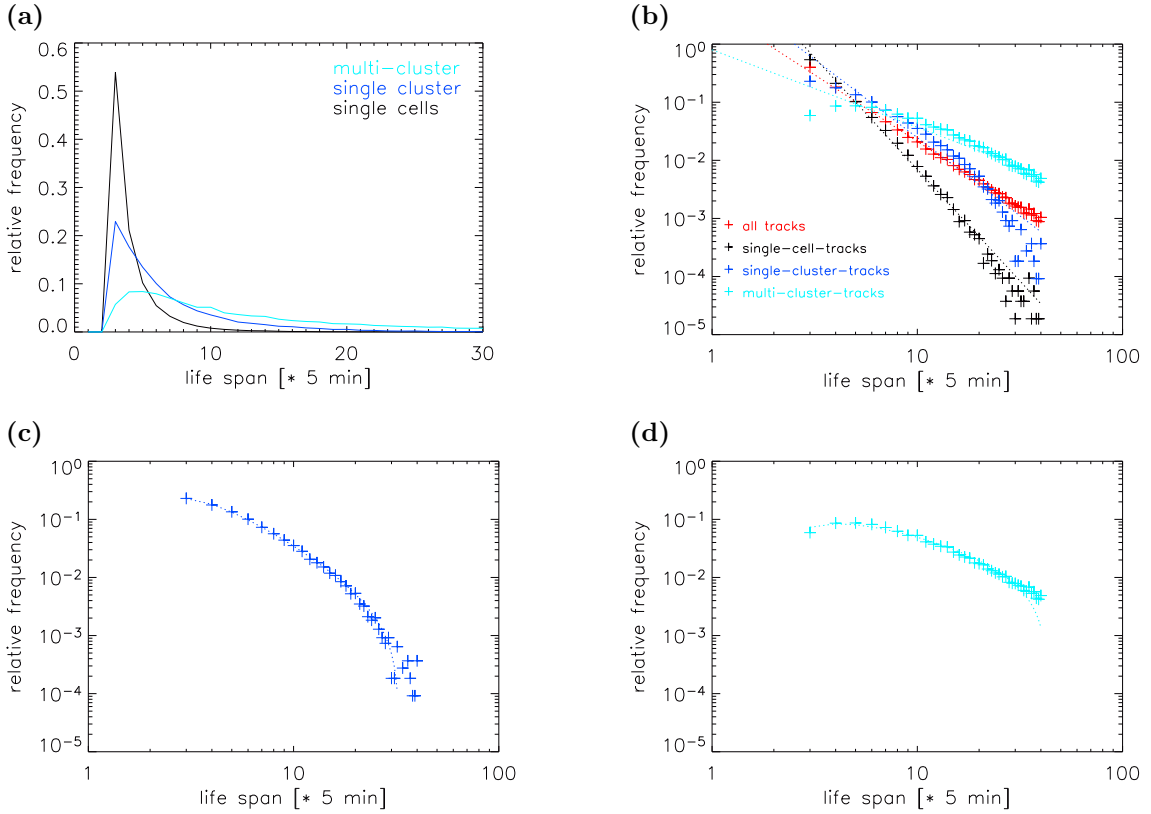


**Figure 3.5:** Frequency distributions of the life spans for the three different track types in a linear presentation (a) and in a double-logarithmic plot together with the frequency distribution for all tracks together (b). The dashed lines represent the power law regression (Equation 3.1), calculated for frequencies greater than  $5 \cdot 10^{-4}$ . The respective parameters can be found in Table 3.2. The distributions for (c) single-cluster tracks and (d) multi-cluster tracks were additionally fitted to a varied power law (dotted lines, Equation 5.4). The parameters can be found in Table 3.3.

## Chapter 3. Data

track type	$l_{max}$ [ $\cdot 5min$ ]	<b>a</b>	<b>b</b>	$\mathcal{R}$
single-cell	19	48.77	-3.84	0.997
single-cluster	32	12.03	-2.69	0.973
multi-cluster	40	0.80	-1.33	0.957
all	40	3.94	-2.28	0.999

**Table 3.2:** Parameters  $a$  and  $b$  of the life span frequency distribution fitted to a power law (Equation 3.1) and correlation coefficient  $\mathcal{R}$ . The second column gives the maximum life span  $l_{max}$  used for the calculation.

track type	$c_2$	$c_3$	$c_4$	$d_2$	$d_3$	$\mathcal{R}$
single-cluster	7.85	0.04	1.85	-2.05	0.90	$\cong 1.000$
multi-cluster	3.09	0.73	0.47	-0.68	0.08	0.990

**Table 3.3:** Parameters of the life span frequency distribution fitted to a modified power law (Equation 3.2).

### 3.2.3 Basic evaluation

Remaining clutter in the radar data that could not be eliminated by clutter filtering has certainly an impact on the tracking procedure. When, for example, two clusters move over permanent clutter at different times, they can misleadingly be assigned to the same track. Caused by an overlap with a cluster  $n$ , the clutter will be assigned to a track  $\theta$ . For each time step the clutter lasts, it will be precursor of itself and thus remain a member of the same track  $\theta$ . When a new cluster  $m$  has an overlap with the still present clutter, that cluster  $m$  is allocated to the already existing track  $\theta$  and the two independent clusters  $n$  and  $m$  would thus be member of the same track.

Another problem arises when radar data is missing in certain parts of the radar image, for example due to shielding or caused by a temporary breakdown of a radar station. This may lead to large clusters suddenly disappearing or reappearing within a time step of 5 min (WEUSTHOFF AND HAUF 2008b).

The performance of the tracking has only been checked for a small set of selected cases. Despite the problems with clutter, the results are promising so far. As a first quality measure, the identified tracks are compared to the wind field in a qualitative way. This comparison is presented here for data of 26 August 2004. In Figures 3.6 and 3.7 tracks with a length of 50 - 100 min with starting times of 00-06 UTC, 06-12 UTC, 12-18 UTC and 18-24 UTC are presented together with the 925 hPa wind fields at the beginning of the respective period. The tracks basically move with the 925 hPa wind field with only slight deviations. This indicates that the steering level for post-frontal showers is probably located in that height. A change in the wind

### Chapter 3. Data

---

direction as for example observed in the north-eastern part of Germany between 12 and 18 UTC causes a correspondent change in the movement of the tracks. A more quantitative evaluation of the tracking results is left for further studies. So far, it can be stated that the 925 hPa wind field seems to be an appropriate indicator for the movement of the clusters.

In Appendix B, the comparison is shown for all investigated days. All tracks of a day with a life span of 50 - 100 min are presented in direct comparison to the 925 hPa wind field at 12 UTC and the daily rain sums. The spatial structure of the latter also indicates the movement of the clusters.

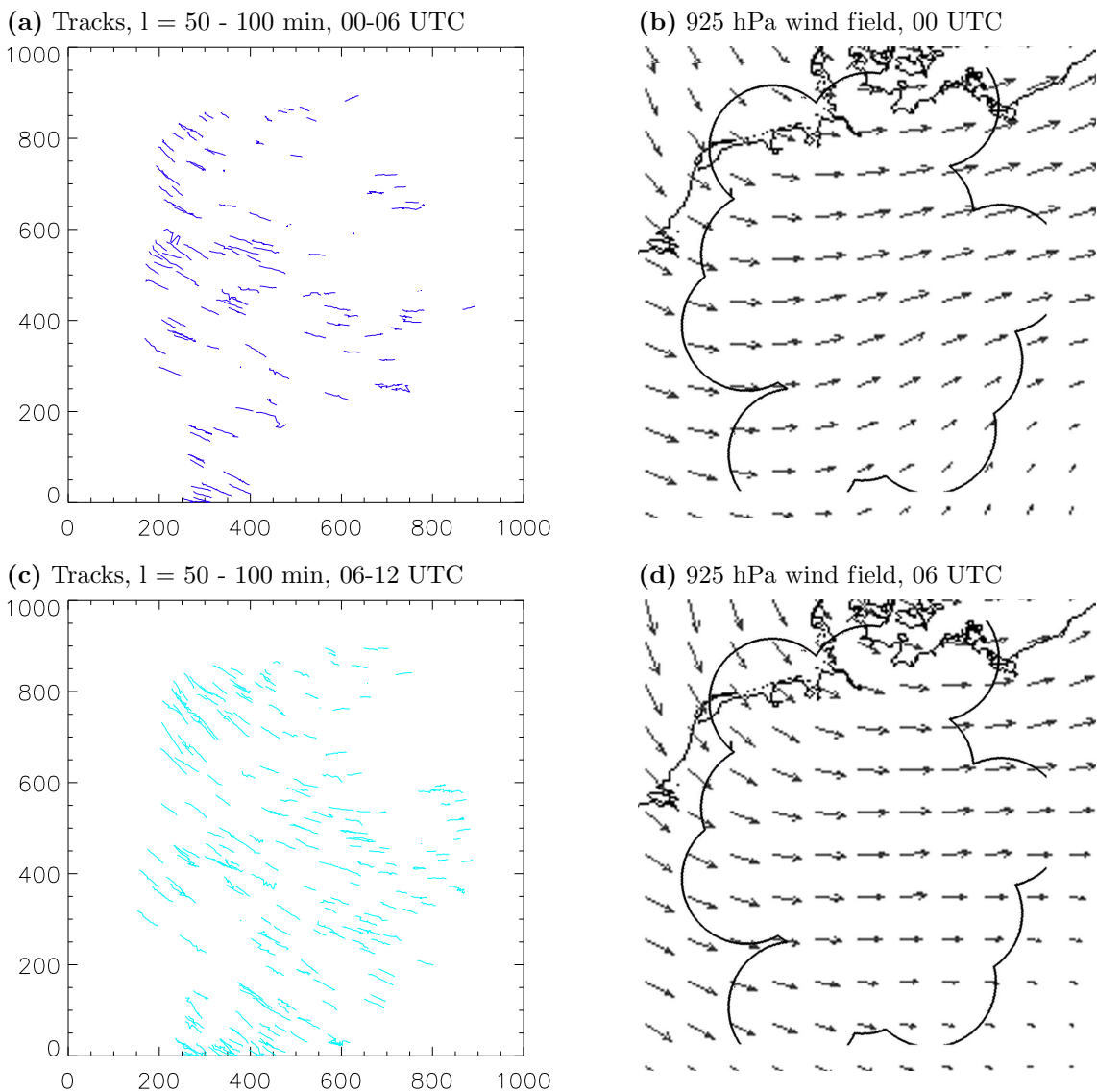


**Figure 3.6:** Comparison of tracks with life spans of 50 - 100 min with the 925 hPa wind field (NCEP reanalysis data) for 26 August 2006, 00 and 06 UTC.



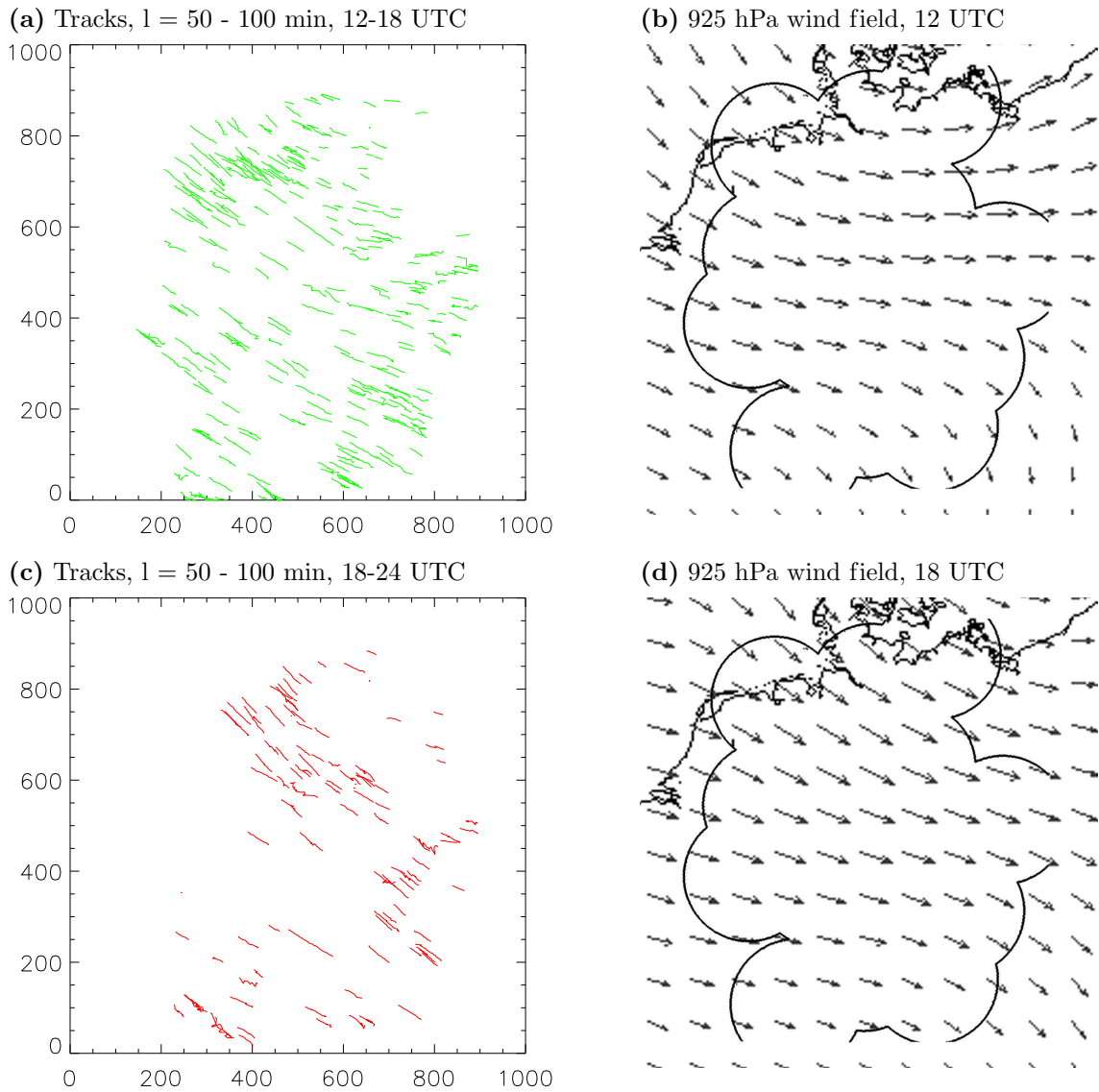


**Figure 3.7:** Comparison of tracks with life spans of 50 - 100 min with the 925 hPa wind field (NCEP reanalysis data) for 26 August 2006, 12 and 18 UTC.

# Chapter 4

## Local rain rates

For the present study, a quantitative radar product, which gives the 5 min rain rate values with an accuracy of 0.01 mm per 5 min, was analysed. This data gives the possibility to investigate not only the spatial structures of the precipitation field, but also the quantitative precipitation characteristics. Thus, the radar derived rain rates were analysed at fixed times and diurnal cycles were determined (Section 4.1). Furthermore, the daily sums were calculated (Section 4.2) and mean wet and dry times were determined (Section 4.3).

	Radar reflectivity [dBZ]	Rain rate [mm / 5 min]
I	7-18.9	0.01-0.03
II	19-27.9	0.03-0.16
III	28-36.9	0.16-0.68
IV	37-45.9	0.68-2.92
V	> 45.9	> 2.92

**Table 4.1:** Radar reflectivity and rain rate classes, respectively.

### 4.1 Diurnal cycle of rain rate classes

In a first attempt to qualify the rain rates given in the RZ composite, the occurrence of rain rate classes according to Table 4.1 was determined. The classes were defined on the basis of the corresponding reflectivity classes of the DWD, calculated by using the standard Z-R-relationship. Caused by the cut-off of 0.05 mm per 5 min used for the radar data (see Section 3.1.1), class II with a modified lower value of 0.05 mm per 5 min is the lowest class considered. It can be seen that in post-frontal

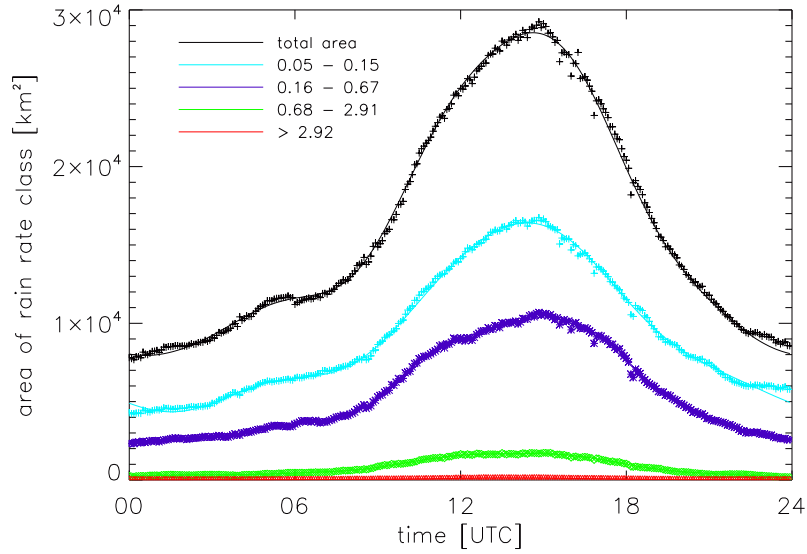


**Figure 4.1:** Mean diurnal cycle of area covered by the different rain rate classes as well as of the total precipitation area, averaged over all 17 days.

situations the lower rain rates clearly dominate the radar image. Almost 75 % of the detected rain activity in the investigated situations shows a radar derived rain rate of 0.05 - 0.16 mm per 5 min. Higher rain rates are less dominant and values of more than 2.92 mm per 5 min are rarely detected.

The diurnal cycle of each of those rain rate classes shows a shape which is close to that of the diurnal variations of the total precipitation area (Figure 4.1, see also Section 5.1.1). The maximum in each class is reached in the early afternoon while the minimum can be found in the night. The differences between day and night are less for the lower rain rate classes ( $Max/Min = 4.0$  for II) than they are for the higher rain rate values ( $Max/Min = 11.9$  for V). The diurnal variations are well described by the first five frequencies of the fast Fourier transformation (FFT):

$$f(t) = \frac{a_0}{2} \left( 1 + \sum_{n=1}^5 \left[ \frac{2a_n}{a_0} \cdot \cos(n\omega t + \phi_n) \right] \right) \quad (4.1)$$

with  $a_n$  and  $a_0$  being scaling parameters and  $\phi_n$  an offset parameter (THEUSNER 2007). The parameters and the correlation can be found in Table 5.1.

## 4.2 Daily rain totals

The daily totals of the radar derived rain rates were already introduced in Section 3.2.3 for the evaluation of the tracks. For the summation all available radar derived rain rates were employed, including those below the cut-off. The spatial structure of the daily precipitation total reveals basically the movement of the clusters, but it also exposes the deficiencies of radar measurements, such as consistency problems

## Chapter 4. Local rain rates

	$a_0$	$a_1$	$a_2$	$a_3$	$a_4$	$a_5$	$\phi_1$	$\phi_2$	$\phi_3$	$\phi_4$	$\phi_5$	$\mathcal{R}$
<b>II</b>	18528.6	0.59	0.15	0.05	0.02	0.00	0.59	1.36	1.35	-1.47	1.20	$\cong 1.00$
<b>III</b>	11228.4	0.69	0.18	0.00	0.04	0.02	0.59	1.47	1.57	-1.42	-1.01	$\cong 1.00$
<b>IV</b>	1620.9	0.87	0.27	0.01	0.03	0.04	0.45	1.13	1.26	-1.38	-0.69	$\cong 1.00$
<b>V</b>	94.9	1.02	0.40	0.13	0.02	0.03	0.48	1.03	-1.39	-1.48	0.92	$\cong 1.00$

**Table 4.2:** Parameters of the fast Fourier transformation of the diurnal variations of four reflectivity classes (Equation 4.1).

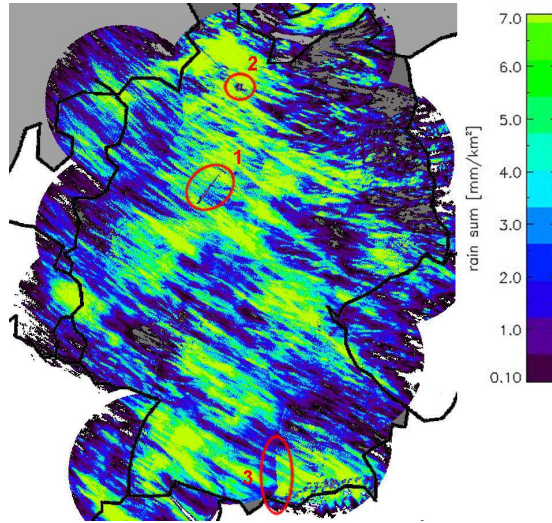


**Figure 4.2:** Daily totals of radar derived rain rates of 26 August 2004, revealing some deficiencies of the radar measurement: (1) spokes, (2) lack of data around the radar station and (3) consistency problems at the overlap of two radar stations.

at the overlap of two radar stations or spokes around a radar station (see Figure 4.2). The images of the daily totals for individual days can be found in Appendix B (Figure B.1 - B.6).

A basic evaluation of the radar derived rain sums was presented in Section 3.1.2. The comparison of the daily totals from the radar with ground based measurements revealed a considerable overestimation of precipitation amounts by radar. Nevertheless, the frequency distribution of the daily totals were calculated in classes of 1 mm per km<sup>2</sup>, showing a strong decrease toward larger rain sums (Figure 4.3 (b)). About 90 % of all pixels reveal a daily total of less than 6 mm. This is not surprising considering the rain rate frequency distribution (Figure 4.3 (a)).

## Chapter 4. Local rain rates

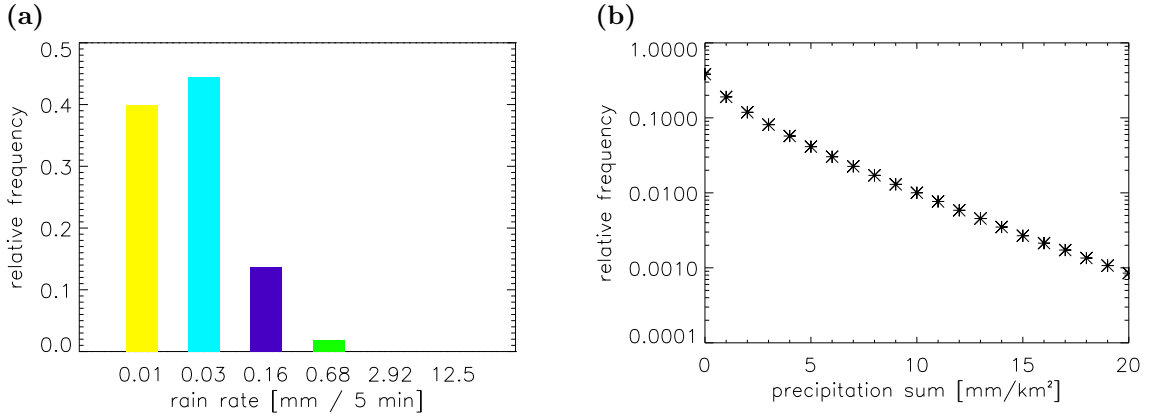


**Figure 4.3:** (a) Frequency of occurrence of the different rain rate classes for all 17 days. (b) Frequency distribution of daily totals per km<sup>2</sup> for all 17 days in a logarithmic presentation.

	dry time	$\sigma$	wet time	$\sigma$
total	1335	55	57	55
mean	377	432	18	28

**Table 4.3:** Total and mean dry and wet times [min] per pixel of 1 km<sup>2</sup>, averaged for all days with standard deviation  $\sigma$ . The calculation was done without those pixels, which are without rain all day.

### 4.3 Duration of wet and dry events

A question of common interest is how long a shower will last at a fixed point and how long the dry time between two showers may be. An answer can be given by determining the mean times locally with and without rain. Therefore, each pixel of the radar image was evaluated with respect to consecutive times with and without precipitation. This way, the total time with rain and without rain for each single pixel was determined through summation of all wet and dry times, respectively. The mean time with or without precipitation was derived through dividing the latter by the number of respective events per pixel. Table 4.3 shows the average values and the standard deviations for the whole area covered by weather radar. Obviously, the main part of the area is nearly the whole day without rain. The average total precipitation time per pixel is about 57 min for all days ranging from a mean value of 30 min up to 100 min on individual days. The average mean time with consecutive rain is just about 18 minutes, while it does not rain on average for over 6 hours. The ratio of wet and dry times for the total duration per pixel is 0.043 and for the mean duration per pixel 0.048. Although deviations are very large, it can be concluded that the time between two showers is in average about 21 times the duration of a shower event.

### 4.4 Discussion

The post-frontal precipitation field extends over a large area, but only shows relatively low precipitation amounts. While nearly 75 % of the detected rain rates have a value of 0.03 - 0.16 mm per 5 min, rain rates over 2.92 mm per 5 min are rarely detected. The daily precipitation sums are basically less than 10 mm per square kilometer. More than 90 % of all pixels with a radar detected daily rain sum  $> 0$  reveal values of 5 mm or less.

The precipitation field is governed by several hundreds of individual showers on each day. The shower duration at a given pixel of one square kilometre was found to be about 18 min in average with a large standard deviation ( $\sigma = 28 \text{ min}$ ), the mean dry time is 377 min. This means that a short shower is usually followed by an almost 21 times longer phase without precipitation.

# Chapter 5

## Geometry

The geometric structure of post-frontal shower fields was previously analysed by THEUSNER (2007) (in the following referred to as THEU07) by means of the PC composite of the DWD with a spatial resolution of 2 km x 2 km and a temporal resolution of 15 min. Besides the diurnal cycle of parameters such as the number of clusters, THEU07 calculated the cell number distribution (CND) and the cluster size distribution (CSD) and investigated the spatial variabilities of the characteristics. Furthermore, the nearest neighbour distances were determined and first attempts concerning a modelling of the investigated structures were presented.

For the present thesis, selected characteristics of the geometrical structure were recalculated with the higher resolution RZ composite, which has a resolution of 1 km x 1 km and 5 min. The results including the diurnal cycles, the CND and the CSD are presented in Section 5.1. Besides the advantage of a higher resolution, the RZ composite provides radar derived rain rates which were calculated from measured radar reflectivities by means of an advanced Z-R-relationship (see Section 2.2.3). This new data source, which is available since 2004, enables additional investigations of, for example, the rain rate characteristics of the precipitation field (Chapter 4). The recalculation of structural characteristics is done to show the comparability of the two radar products with the different resolutions and clarify if the results presented here and in WEUSTHOFF AND HAUF (2008b) and WEUSTHOFF AND HAUF (2008a) can be used together with those of THEU07 to provide a thorough description of the small-scale convective precipitation field.

The analyses presented in this chapter are based on the instantaneous values of the RZ composite and include no tracking information. In addition to the recalculations presented in Section 5.1, Section 5.2 deals with the clusters' orientation and motion. In Section 5.3, cell related properties are investigated, followed by a short discussion on the results of this chapter in Section 5.4.

## 5.1 Recalculation of selected structural characteristics

In the previous study of THEU07, the geometrical structure was analysed based on the PC composite of the DWD for a data set of 39 days in the years 1997 and 1998. In the present study, a recalculation of selected characteristics by means of the higher resolution RZ composite is presented. As the RZ composite has only been available since 2004, a new data set was applied comprising 17 days in the years 2004 and 2006. Although fewer days were investigated, the higher temporal resolution of 5 min compared to the 15 min temporal resolution of the PC composite leads to a higher number of analysed images. THEU07 analysed 3258 individual radar images, whereas in the present study 4716 radar images were evaluated.

### 5.1.1 Diurnal cycles

The average diurnal variation of the number of clusters identified within the post-frontal precipitation field shows a typical diurnal cycle of convective activity with a maximum of about 400 clusters around 13 UTC and a minimum of about 100 clusters at night (Figure 5.1 (a)). The average total precipitation area reveals a similar diurnal variation, but the maximum with a value of nearly 30 000  $km^2$  is reached about two hours later at approximately 15 UTC (Figure 5.1 (b)). The decline in the evening is sharper than the increase in the morning. In the early morning hours a slight plateau is observed where the precipitation area stays nearly constant for approximately three hours followed by an increase after sunrise. These observations mirror the convective cycle of precipitation over land, as for example reported by LIN ET AL. (2000), with a maximum in the afternoon. According to GRABOWSKI ET AL. (2006), this is also the time when an increased organization of convection into mesoscale features is observed. Such convective variability is basically driven by surface heating as displayed in Figure 5.2. The diurnal cycles presented here represent the average of all analysed days without consideration of the time of the frontal passage. Nevertheless, a typical diurnal cycle of convective activity was observed. This leads to the conclusion that the time of the cold front passing apparently does not play a significant role, but that, instead, the post-frontal shower activity is mainly governed by the overlying convective cycle. Certainly, the timing of precipitation is also influenced by regional characteristics such as local orography and mesoscale circulations (BECHTOLD ET AL. 2004). THEUSNER AND HAUF (2004) analysed regional characteristics of the post-frontal precipitation field and found, besides a preferred occurrence of larger clusters along the North Sea coast, that mountain ranges preferably trigger convection, but do not change the spatial structure of the precipitation field.

The shape of the diurnal variations fits well with the observations reported by THEU07 for the same synoptic situation as well as with those of LÓPEZ ET AL.



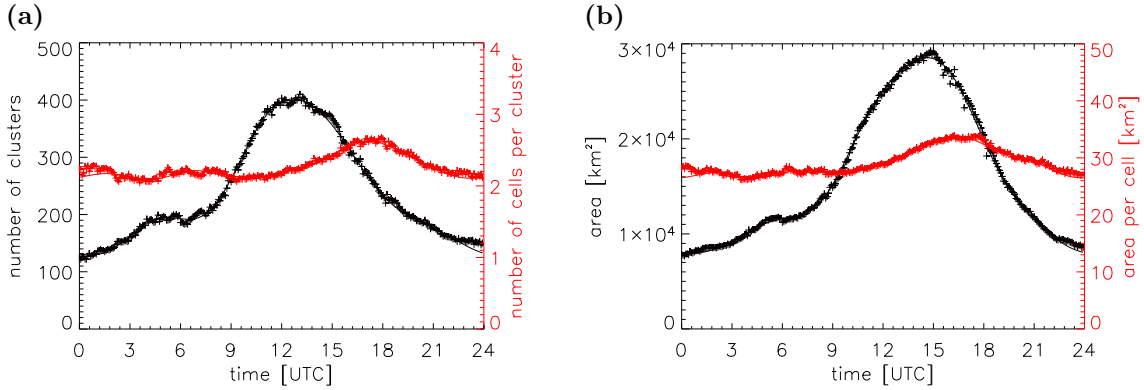


**Figure 5.1:** Diurnal cycles of (a) the number of clusters (black) and the mean number of embedded cells per cluster (red) and (b) the precipitation area (black) and the mean area per cell (red) for all 17 days. The mean number of cells per cluster is  $p \approx 2.3$  and the mean area per cell  $A \approx 30 \text{ km}^2$ .

(1983) (in the following referred to as LOP83) for radar data from the Florida Area Cumulus Experiment (FACE-2). Only the total number of clusters is larger with the RZ composite compared to THEU07 for the same investigation area, which is certainly caused by the higher resolution of the radar data. The absolute values of LOP83 are not comparable to the values presented here as the former only analysed data from one single radar station in contrast to the network of 16 radar stations providing the data for this thesis. For the number of embedded cells within a cluster, a mean value of 2.3 was found with a slight maximum in the afternoon (Figure 5.1 (a)). LOP83 reports a similar diurnal cycle but larger variations ranging from about 1.7 to 4 cells per cluster. THEU07 found a mean number of about 1.6 cells per cluster and rarely a variation over the day. Thus, with the higher resolution radar data not only more clusters were detected but also more individual, embedded convection cells.

The area occupied by an individual convection cell within a cluster shows nearly the same diurnal variation as the number of cells per cluster (Figure 5.1 (b)). Despite a maximum in the afternoon, the ratio stays almost constant over the day with a mean value of  $29 \text{ km}^2$  per cell. While LOP83 reports a comparable average area per cell of 18 to about  $55 \text{ km}^2$  with the maximum around the time of maximum convective activity, THEU07 found a much larger value for the mean area per cell (about  $230 \text{ km}^2$ ). This is due to the fact that a pixel in the PC composite represents an area of  $4 \text{ km}^2$  while a pixel in the RZ composite covers only  $1 \text{ km}^2$ . In addition, the number of detected cells within a cluster is larger for the higher resolution RZ composite (rain rate in steps of  $0.01 \text{ mm}$  per  $5 \text{ min}$ ) compared to the PC composite (6 reflectivity classes). This leads, consequently, to a smaller area assigned to each embedded convection cell in the RZ composite.

Similar to the diurnal variations of the reflectivity classes (see Section 4.1), the diurnal variations of the number of clusters and total precipitation area size presented here are well described by the first five frequencies of the fast Fourier transforma-

## Chapter 5. Geometry

---

tion as given in Equation 4.1. The scaling parameters  $a_0$  and  $a_n$  and the offset parameters  $\phi_n$  can be found in Table 5.1.

	$\mathbf{a}_0$	$\mathbf{a}_1$	$\mathbf{a}_2$	$\mathbf{a}_3$	$\mathbf{a}_4$	$\mathbf{a}_5$	$\phi_1$	$\phi_2$	$\phi_3$	$\phi_4$	$\phi_5$	$\mathcal{R}$
<b>I</b>	32238.7	0.60	0.17	0.03	0.02	0.01	0.53	1.42	1.26	-1.50	-1.30	$\cong 1.00$
<b>II</b>	57.9	0.10	0.05	0.01	0.01	0.01	1.12	-0.68	0.26	-0.81	-0.53	0.98
<b>III</b>	478.3	0.50	0.14	0.08	0.03	0.01	0.25	0.66	0.39	1.54	0.83	$\cong 1.00$
<b>IV</b>	4.5	0.08	0.06	0.02	0.01	0.01	1.33	-0.40	0.75	0.72	-0.45	0.97

**Table 5.1:** Parameters of the fast Fourier transformation for the diurnal variations of area (I), area per maximum (II), number of clusters (III) and maxima per cluster (IV).

### 5.1.2 Cell number distribution

A cluster is assumed as being comprised of one or more individual convection cells, each of which is represented by a local maximum of rain rate (see Section 2.1.2). The number of cells embedded in a cluster is referred to as the cell number  $p$ . The cell number distribution (CND), i.e. the frequency distribution of the number of cells per cluster (normalized with the total number of clusters identified) is displayed in Figure 5.3 (a) for the whole data set of 17 days. The distribution can be approximated by a power law of the form given in Equation 5.1 with a correlation coefficient of  $\mathcal{R} \cong 1.00$ . For the fit, only data with a relative frequency of more than  $5 \cdot 10^{-4}$  were used. The maximum cell number with a frequency above that value was  $p = 25$ .

$$N(p) = a \cdot p^b \tag{5.1}$$

The coefficient  $a$  of Equation 5.1 represents the fraction of single cells which is in this case  $a = 0.69$ . For the parameter  $b$ , the slope of the regression in the double-logarithmic representation, a value of  $b = -2.24$  was derived (see also WEUSTHOFF AND HAUF (2008b)), ranging from -1.92 to -2.50 for individual days (see Figure 5.3 (b)). The value found by THEU07 for a comparable cut-off (cf. Section 3.1) of 19 dBZ lies at the very end of this range with  $b = -2.46$ . MESNARD AND SAUVAGEOT (2003) (hereafter referred to as MES03) investigated the structural characteristics for much smaller areas but with higher resolution data. The slope values for two French regions, Bordeaux at the Atlantic coast and Toulouse more inland, were  $b = -2.48$  and  $b = -1.78$ , respectively, for a cut-off of 23 dBZ. Both authors investigated the dependency of the slope on the cut-off and reported an increasing absolute value of the slope with increasing cut-off.

Except for the case of Toulouse, all slope values are very close together. The remaining differences may be explained with the different data used for the analysis and

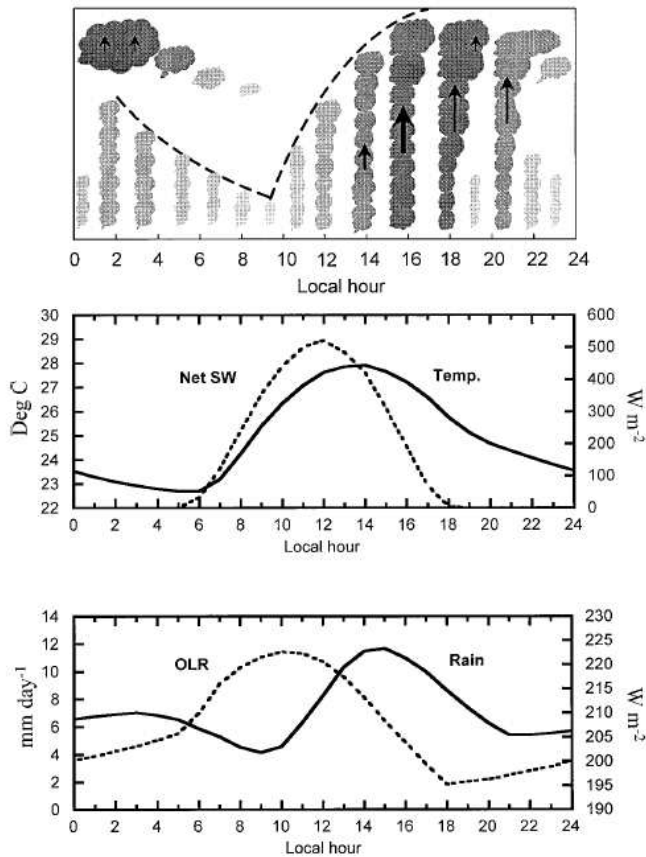


**Figure 5.2:** Descriptive model of the diurnal cycle of convective activity over tropical summer continents (LIN ET AL. 2000) based on satellite and surface observations. *OLR* stands for outgoing longwave radiation and *Net SW* for the net shortwave flux. The maximum of rain is reached about 3 hours after local noon.

the methodical differences in identifying the maxima. While for the present study all local maxima were identified, MES03 only used local maxima which exceeded all their neighbouring pixels by a given threshold. The latter procedure leads to a smaller number of maxima and, consequently, to fewer maxima within a cluster. The procedure of THEU07 concerning the maxima identification is constrained by the fact that the PC composite is given in six classes which implies a certain threshold.

The diurnal variation of the slope  $b$  for the whole data set, as displayed in Figure 5.3 (c) for 3h-intervals, is smaller than the day-to-day variation (Figure 5.3 (b)). Aside from a minimum in the morning and a maximum in the evening the slope is almost constant over daytime. This means that there are more smaller clusters in the morning and more larger ones in the evening while the distribution is self-similar over the rest of the day. Only the total number of maxima changes according to the diurnal cycle (see Section 5.1.1). Due to limited sample statistics, the variation for single days is usually larger as can be seen in Figures 5.4 (a)–(c) for three individual days.

## Chapter 5. Geometry

In summary, the CND was found to be scale-invariant, i.e. the ratio of clusters with  $n$  embedded cells and clusters with  $m$  embedded cells stays constant for arbitrary values of  $n$  and  $m$ . Besides large day-to-day variations of the parameter  $b$  of the power law, the diurnal variation of that parameter rarely shows a variation over daytime. Based on those observations, an influence of the air mass characteristics of different post-frontal situations on the CND is assumed. This was investigated by WITHA (2007) by means of various stability indices and parameters such as the maximum cloud height, but so far no unambiguous dependencies could be identified.

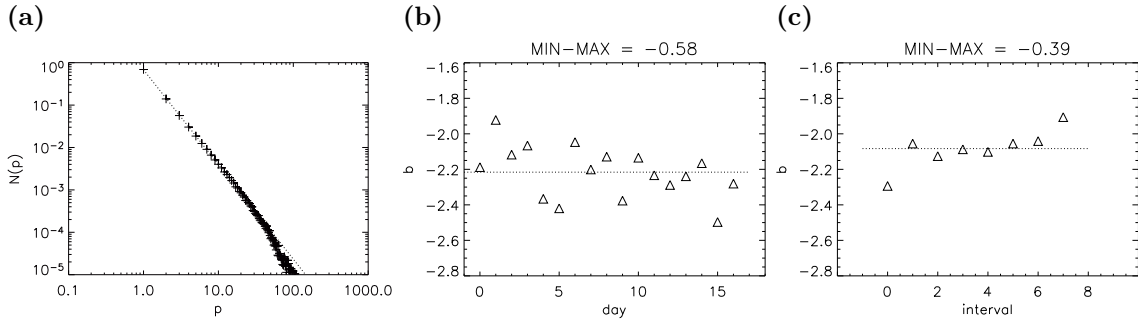


**Figure 5.3:** (a) Cell number distribution (CND) for all days, fitted by a power law (Equation 5.1), (b) day-to-day variation of the slope  $b$  and (c) diurnal variation of the slope  $b$  for 3h-intervals.

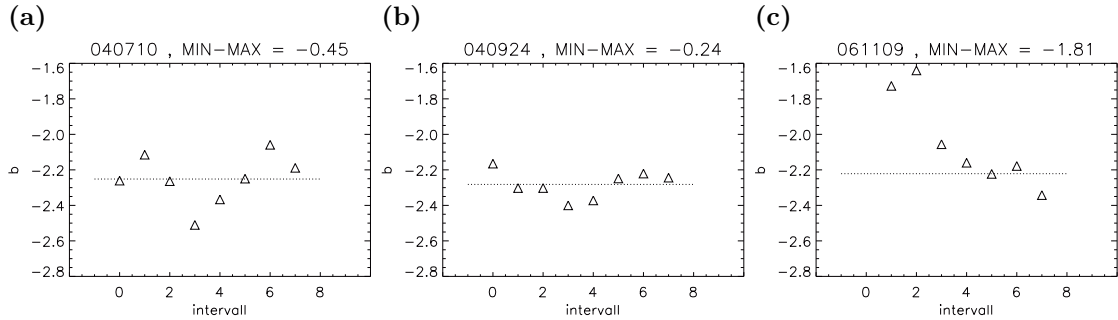


**Figure 5.4:** Diurnal variation of the parameter  $b$  of the cell number distribution by means of 3h-intervals for three individual days: (a) 10 July 2004, (b) 24 September 2004 and (c) 9 November 2004.

### 5.1.3 Cluster size distribution

The cluster size distribution (CSD)  $N(D_p)$  was calculated for each fixed cell number  $p$ . The size of a cluster is hereby represented by the equicircle diameter  $D_p$  following the procedure of THEU07. The data for each cell number can be fitted by a lognormal distribution (Figure 5.5, Equation 5.2). The mean and the standard deviation of  $\ln(D_p)$ ,  $\mu_p$  and  $\sigma_p$ , respectively, depend on the cell number  $p$  and can - like in previous studies - be described by power laws. The variations of  $\sigma_p$  with cell number  $p$  are well represented by a simple power law (Equation 5.3) with a

## Chapter 5. Geometry

---

correlation coefficient of  $\mathcal{R} \cong 1.00$  (fit for  $2 \leq p \leq 10$ , see Figure 5.6 (b)). The parameters of the power law are given in Table 5.2. They are in line with those reported by THEU07 for the lower resolution radar data and almost the same MES03 derived for a smaller investigation area. The variation of  $\mu_p$  with respect to the cell number  $p$  was fitted to a modified power law (Equation 5.4) as it apparently is not best represented by a simple power law which would give a straight line in the double logarithmic presentation (Figure 5.6 (a)). Despite a correlation coefficient of 0.98 for the simple power law, the modified power law gave a better fit with a correlation coefficient of  $\mathcal{R} \cong 1.00$ . While MES03 applied a simple power law for the fit, THEU07 used a modified power law which differs slightly from Equation 5.4.

$$N(D_p) = \frac{\exp\left(-\frac{(\ln(D_p) - \mu_p)^2}{2\sigma_p^2}\right)}{\sqrt{2\pi} \cdot D_p \cdot \sigma_p} \quad (5.2)$$

$$\sigma_p = c_1 \cdot p^{d_1} \quad (5.3)$$

$$\mu_p = c_2 \cdot p^{d_2} \cdot \left(1 - c_3 \cdot p^{d_3} - \frac{c_4}{p}\right) \quad (5.4)$$

The first moment of the lognormal distribution as given in Equation 5.5 represents the expected value of the variable, i.e.  $\bar{D}_p$ . Inserting Equation 5.3 for  $\sigma_p$  and Equation 5.4 for  $\mu_p$  into Equation 5.5 gives the mean equicircle diameter as a function of  $p$  (Equation 5.6).

$$\bar{D}_p = \exp\left(\mu_p + \frac{1}{2}\sigma_p^2\right) \quad (5.5)$$

$$= \exp\left(c_2 \cdot p^{d_2} \cdot \left(1 - c_3 \cdot p^{d_3} - \frac{c_4}{p}\right) + \frac{1}{2}(c_1 \cdot p^{d_1})^2\right) \quad (5.6)$$

Thus, it is possible to calculate the mean equicircle diameter  $\bar{D}_p$  for a given value of  $p$ . From this mean equicircle diameter the mean area  $\bar{A}_p$  of a cluster with cell number  $p$  can be deduced:

$$\bar{A}_p = 2 \cdot \pi \cdot \left(\frac{\bar{D}_p}{2}\right)^2 \quad (5.7)$$

Together with the above presented cell number distribution  $N(p)$  the here derived CSD  $N(D_p)$  can be used to determine the cell independent size distribution  $N(D)$ :

$$N(D) = \sum_{p=1}^{p_{max}} N(D_p) \cdot N(p) \quad (5.8)$$

$c_1$	$c_2$	$c_3$	$c_4$	$d_1$	$d_2$	$d_3$
0.38	4.32	0.61	0.14	-0.33	0.33	0.06

**Table 5.2:** Parameters of the equations for  $\sigma_p$  (Equation 5.3) and  $\mu_p$  (Equation 5.4) as a function of cell number  $p$ .

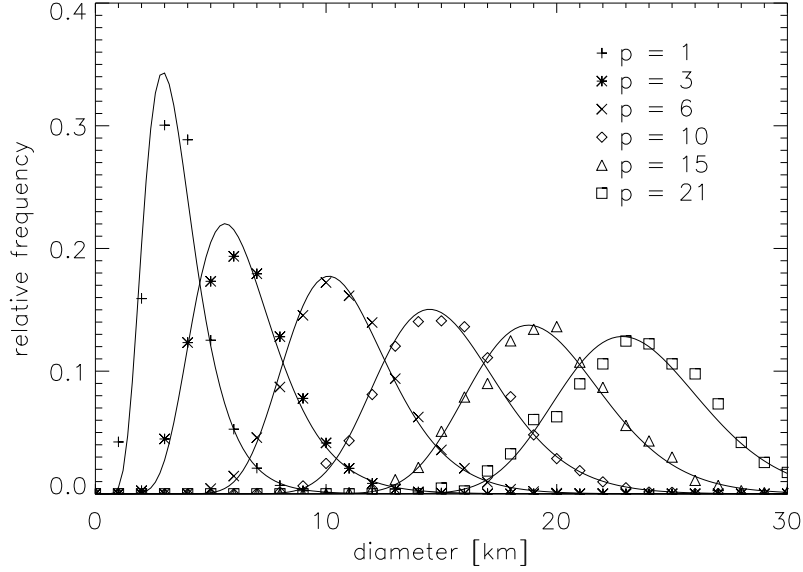


**Figure 5.5:** Cluster size distribution  $N(D_p)$  and lognormal distribution fit for different cell numbers  $p$ . The cluster size is hereby represented by the equicircle diameter  $D_p$ .

In the same way, the size distribution with respect to the areal extent  $N(A)$ , as displayed in Figure 5.7, can be determined. This was successfully done by THEU07 yielding very good agreement between the calculated distributions and those directly determined from the radar data. The area size distribution without cell number distinction can be approximated by a power law with large deviations occurring for small area sizes ( $< 11 \text{ km}^2$ ).

The main conclusion from the here presented observations is that the results obtained by means of the new RZ radar composite are to a high degree comparable to those of previous studies using the lower resolution PC composite. The results of THEU07 can, consequently, be taken as the basis for a description of the post-frontal precipitation field. By using the higher resolution radar composite and the rain rate values given therein this basic characteristics can be extended by rain rate characteristics and the temporal development of the individual clusters to provide a more detailed picture of the shower field.

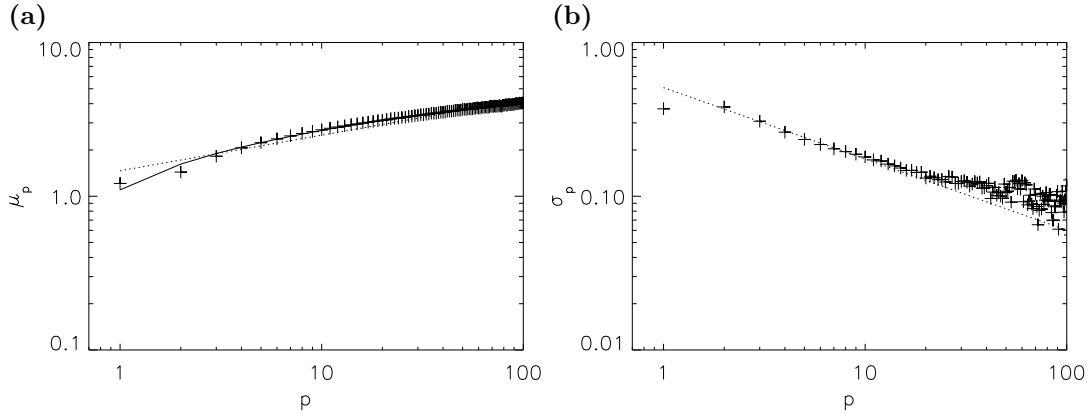


**Figure 5.6:** Parameter (a)  $\mu_p$  and (b)  $\sigma_p$  of the lognormal distribution. While  $\mu_p$  was fitted to a modified power law (Equation 5.4),  $\sigma_p$  is well represented by a normal power law (Equation 5.3).

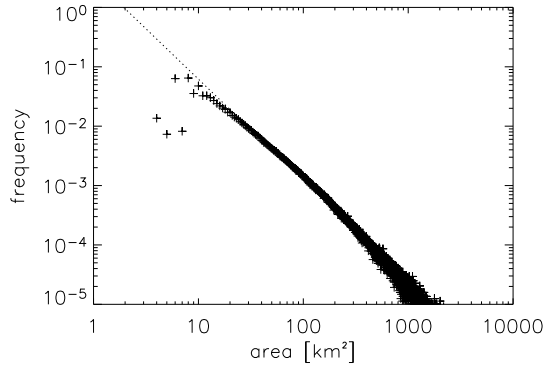


**Figure 5.7:** Frequency distribution of the cluster area  $A$  for the whole data set without cell number distinction. The dotted line gives the power law which was fitted to the data with a linear correlation coefficient of  $\mathcal{R} = -0.99$  for areas of more than  $10 \text{ km}^2$  in size. Smaller clusters show significant deviations from the power law.

## 5.2 Cluster orientation and motion

Locally measured rainfall is influenced by precipitating cells that move with the present flow and also follow their individual life cycles. While investigations into the life cycle of individual clusters are presented in Section 2.1.2 and 3.2 as well as in Chapter 6, this section deals with the shape of individual clusters and their orientation relative to the mean flow. The shape of rain cells is relevant to many applications in meteorology and hydrology, such as stochastic point-process models for intense precipitation events (e.g. WHEATER ET AL. (2000) assuming circular shape and VON HARDENBERG (2003) assuming elliptical shape), nowcasting systems like those discussed by WILSON ET AL. (2004) or rain-runoff modelling (FERAL ET AL. 2000). According to KARKLINSKY AND MORIN (2006), the hydrological response of a drainage basin is sensitive to the spatial characteristics of the rain cells. HAUF ET AL. (2001) additionally found a strong dependence of precipitation distribution

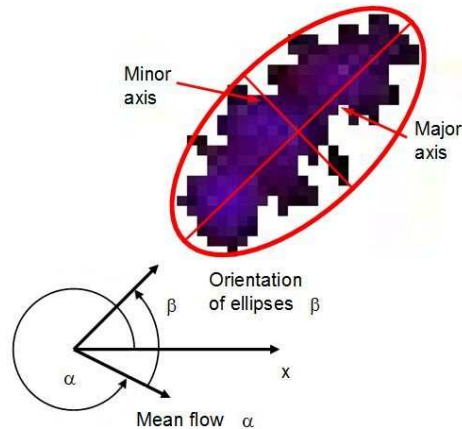


**Figure 5.8:** Definition of the ellipses' parameter: major axis, minor axis and orientation  $\beta$  of the ellipse relative to the mean flow ( $\alpha$ , counter-clockwise, starting from x-direction).

on the formation of rain cells. In that study, a circular shape was assumed for individual cells. If the circular shape turned out to be a good approximation for the clusters as well, the orientation of the latter relative to the flow would have no influence on the local rain amount. Assuming an elliptic shape, significant differences would be observed locally between a cell which is oriented parallel to the flow and a cell which has an orientation perpendicular to the flow.

The rain cell shape and orientation were previously investigated, for example, by FERAL ET AL. (2000) for South-West of France and KARKLINSKY AND MORIN (2006) for the area of Southern Israel. The latter analysed both features for every single cell whereas in the present study clusters including one or more individual convection cells are considered. Each of those clusters was approximated by an ellipse (see Figure 5.8). The major and minor axes were determined as well as the orientation of the ellipses with respect to the mean flow direction. The ellipticity, defined as the minor axis divided by the major axis, was calculated and the frequency distributions and mean and median values of the various parameters were determined for the whole data set (Figure 5.9).

The results are comparable to those of the authors cited above. Both authors found lognormal distributions for minor and major axes and a normal distribution for the ellipticity. These distribution functions were also fitted to the present data set (see Figure 5.9) with correlation coefficients of 0.77 (minor axis), 0.67 (major axis) and 0.46 (ellipticity). The orientation of the clusters in the present study was relatively uniformly distributed, like in the study of FERAL ET AL. (2000). KARKLINSKY AND MORIN (2006), in contrast, found a preferred orientation perpendicular to the mean wind direction. The mean value for the ellipticity factor is 0.58, which means that the ellipses are in average about twice as long as wide. This value is a bit lower than that of KARKLINSKY AND MORIN (2006), who found 0.63 for the single



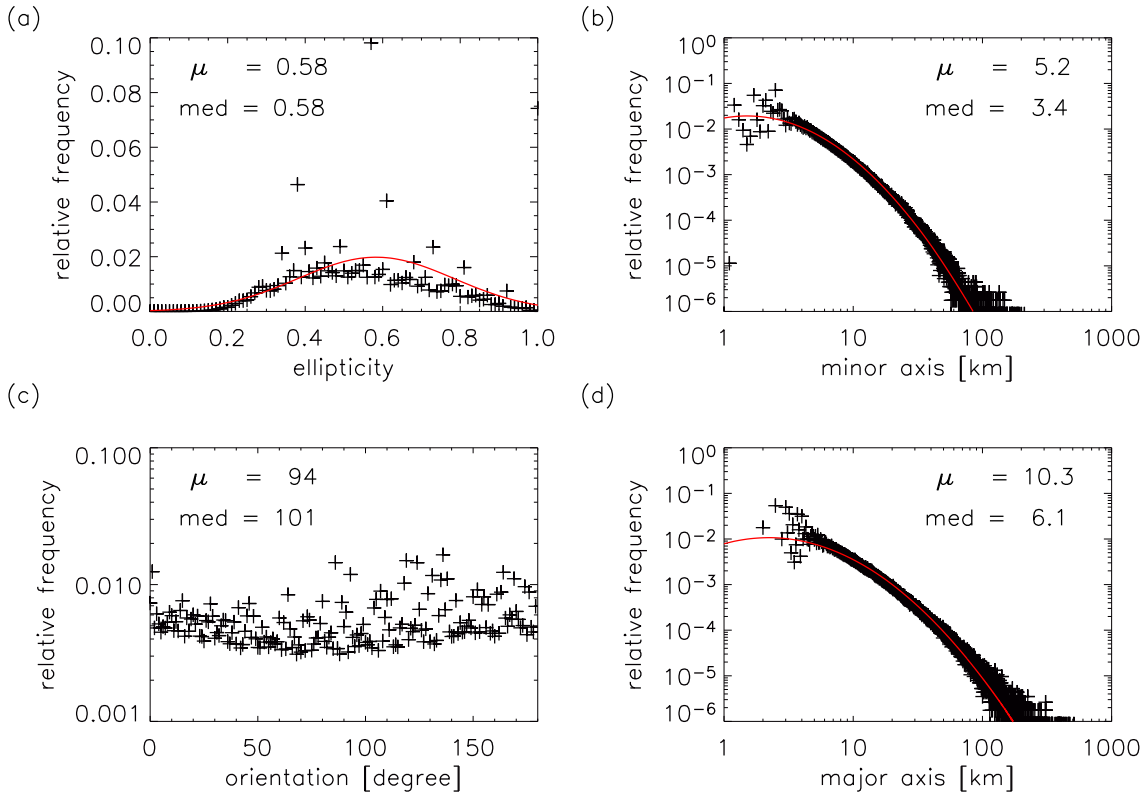


**Figure 5.9:** Frequency distributions of (a) ellipticity, defined as minor axis divided by major axis, (b) minor axis, (c) orientation  $\beta$  and (d) major axis. The red lines give the distributions found by other authors for the same parameters.

cells, and nearly the same as that of FERAL ET AL. (2000) with 0.57 for the total clusters. The distributions for minor and major axes both show skewness to the left with a mean value of 5.2 km (minor axis) and 10.3 km (major). KARGLINSKY AND MORIN (2006) found lower values for the axes (minor: about 3 km, major: about 5 km) which is probably due to the fact that they consider single cell features. Interestingly, the median values of the distributions presented here are nearly the same (minor: 3.4 km, major: about 6.1 km). The reason is probably the dominance of single cells in the considered post-frontal situation.

The picture changes when only large clusters are considered. The frequency distributions for clusters which occupy an area of more than  $100 \text{ km}^2$  are displayed in Figure 5.10. Assuming a mean area of  $30 \text{ km}^2$  per cell (see Section 5.1.1), a cluster then would include at least three individual cells. The distributions show less scatter than those including all clusters. The ellipticity is normally distributed with skewness to the left with a mean value of approximately 0.5. Minor and major axes are consequently larger compared to the values given above, with mean values of 16.5 km and 36.1 km, respectively. The most noticeable difference can be seen in the frequency distribution of the orientation. While no preferred orientation is identifiable when all clusters are included in the analysis, clusters  $> 100 \text{ km}^2$  show a

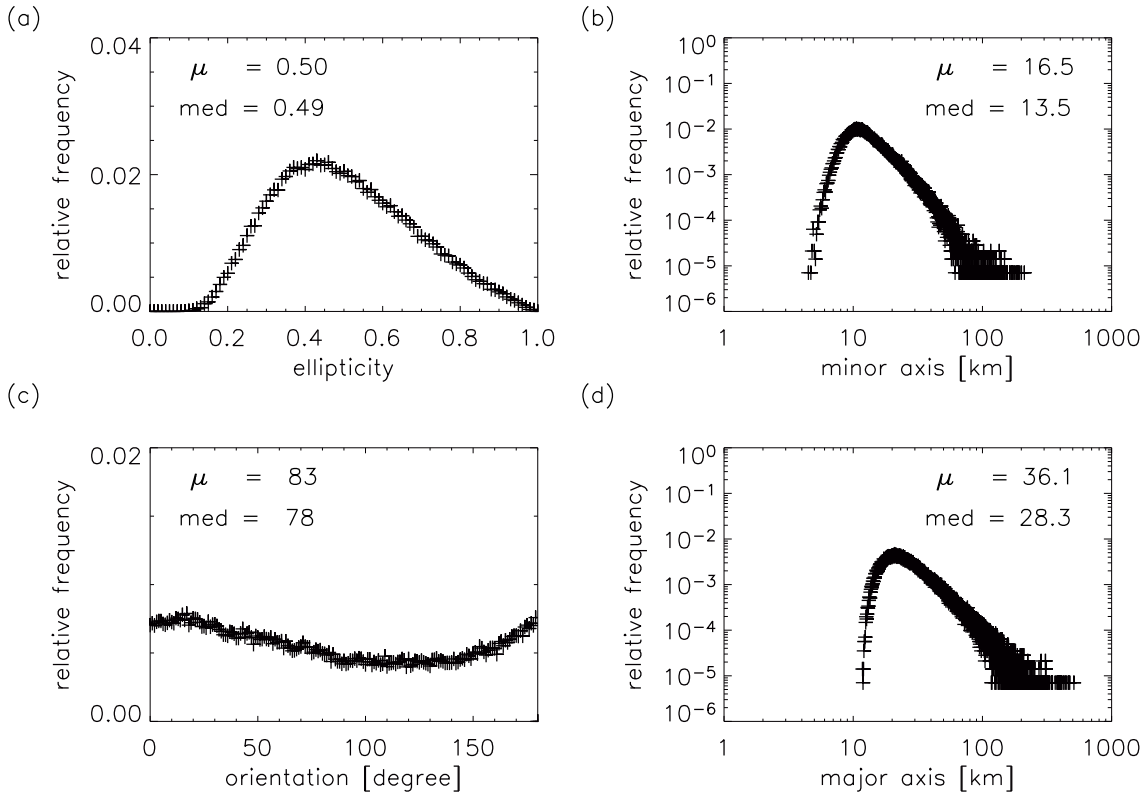


**Figure 5.10:** Frequency distributions of (a) ellipticity, defined as minor axis divided by major axis, (b) minor axis, (c) orientation  $\beta$  and (d) major axis for clusters with an area of more than 100 km<sup>2</sup>.

preferred orientation around 20°, i.e. nearly parallel to the mean flow, with a slight deviation to the left.

The movement of the individual clusters within the precipitation field follows approximately the 925 hPa wind direction. This movement can be derived from the total daily precipitation but also from a plot of the tracks indicated by path lines from the tracking of the clusters. Figures 3.6 and 3.7 shows such tracks with a track length of 50 to 100 min with starting times classified into four time periods on 26 August 2004 in comparison with the 925 hPa wind field at the beginning of each time period (00 UTC, 06 UTC, 12 UTC, 18 UTC). The comparison reveals nearly the same directions for wind arrows and tracks. They are aligned in south-westerly directions with slight variations in the course of the day. A comparison of tracks with a life spans of 50 - 100 min with the 12 UTC wind field can be found for all 17 days in Appendix B (Figures B.1 - B.7).

In summary, individual clusters within the precipitation field are apparently well represented by ellipses with the major axis about twice as long as the minor axis. Although visual inspection of the radar images lead to the assumption that the individual clusters have a preferred orientation, which was also reported in previous studies, this could not be observed for the investigated data set. Instead, the

orientation of the clusters was nearly equally distributed. Only if small clusters ( $< 100 \text{ km}^2$ ) are eliminated, is a preferred orientation observable directed at around  $20^\circ$  relative to the mean flow. The steering level controlling the movement of the individual clusters is located in heights of approximately 925 hPa. Thus, important information could be derived in preparation of a modelling of the post-frontal precipitation field.

### 5.3 Cell based characteristics

Relating the quantities of the clusters to the individual cells they contain gives additional information on the precipitation field. One of those quantities is the area integrated rain rate (AIRR), which was determined as a function of the number of embedded cells  $p$  (WEUSTHOFF AND HAUF 2008a). Normalisation with the respective cell count gives the AIRR per cell;  $AIRR(p)/p$ . This analysis was done for all clusters identified in the radar data of the 17 analysed days. The average values are plotted in Figure 5.11 (a). In the same way, the area per cell  $A(p)/p$  was determined (Figure 5.11 (b)) as well as the ratio of those two quantities, i.e.  $AIRR(p)/A(p)$  (Figure 5.11 (c)).

Both the AIRR per cell and the area per cell increase with the number of embedded cells. Obviously, the formation of cells in clusters leads to an increased efficiency of the individual cells. At a specific cell count saturation effects appear. This is the case at  $p \approx 20$  for the AIRR per cell with a maximum value of about 11 mm per 5 min, after which the AIRR even decreases. For the area per cell, the increase slows down already at a cell number of 10, which was also observed by THEU07, and becomes saturated when a cell number of about 40 is reached with a mean cluster size of  $A \approx 45 \text{ km}^2$ . It can be concluded that cells embedded in a cluster are more efficient in terms of rain rate. Similarly, the area per cell increases with the number of embedded cells. This means, a cluster of  $i$  enclosed cells produces more precipitation than  $i$  single cells and, similarly, covers a larger area than the respective number of single cells do. This corresponds to the common experience that within a larger cluster the rain rate to be expected is higher than within a single cell.

The highest AIRR per area, i.e. the rain density in mm per 5 min per  $\text{km}^2$ , appears for a cluster with  $p = 25$ . This is caused by the fact that the area per cell shows a continuous increase with the cell number, while the AIRR per cell reaches a critical size at  $p = 20$  embedded cells after which it stays nearly constant and then decreases for higher cell numbers than  $p = 25$ .

In summary, both AIRR per cell and area per cell increase through the formation of clusters where the AIRR shows saturation effects for lower cell numbers than the area. The maximal efficiency in terms of rain rate at a cell number of  $p \approx 20$  has not been observed before.

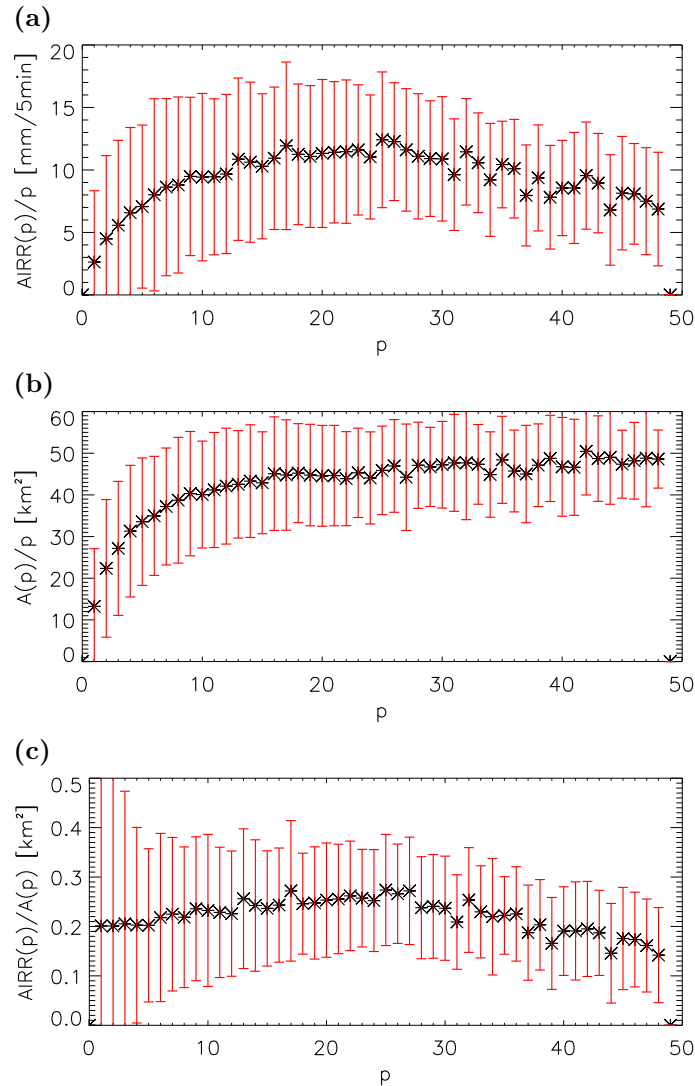


**Figure 5.11:** (a) Mean area integrated rain rate per cell and (b) mean area per cell as a function of total cell number. (c) Mean ratio of area integrated rain rate per area with respect to the cell number. The error bars represent the standard deviations, which are lower for the area than for the AIRR. The mean coefficients of variation are 0.62 for the AIRR, 0.30 for the area and 0.59 for the AIRR per area.

## 5.4 Discussion

The geometrical structure of the post-frontal precipitation field has previously been analysed by THEU07 by means of radar data from the PC composite of the DWD. It was found that a small number of parameters is sufficient to describe the basic characteristics of the shower field. A recalculation of selected characteristics with higher resolution radar data, which is presented in this thesis, reveals comparable results. Thus, the results of THEU07 provide the basic description of the investigated small-scale structure which can now be extended by rain rate characteristics (see

## Chapter 5. Geometry

---

Chapter 4) and the description of the structures' temporal development (see Chapter 6). In addition, new investigations on the geometrical structure, which are presented in this chapter, provide additional information for a thorough description of the post-frontal precipitation field.

The geometric structure of the post-frontal precipitation field is basically governed by power laws and lognormal distributions as was already shown in previous studies. THEU07 speculates on self-organised criticality (SOC) as a possible explanation for the evolution of the observed ordered structures within the post-frontal precipitation field. The theory says that some dynamical systems naturally develop into a critical state with no characteristic time or length scales, evident as a power law shaped frequency distribution (BAK ET AL. 1988). However, the presence of the temporal signature of SOC, i.e.  $1/f$  noise (a power spectral density proportional to the reciprocal of the frequency), could not be detected so far for the case of post-frontal shower structures.

The area size distribution has been analysed by several authors, for cloud fields by means of satellite data and for rain areas based on radar data. CRAIG AND COHEN (2006) give a brief overview over published studies and the fitting functions found by those authors. Besides exponential and lognormal distributions, more recent studies report power law distributions, often with a scale break. According to that review, exponential distributions are frequently observed for *young* cloud fields while the more mature cloud fields rather fit a power law. The latter was also found in the current thesis for the total area size distribution without peak number distinction. For the cluster size distribution of each distinct cell number, a lognormal distribution was found. Such a distribution is often observed in systems that grow by the law of proportionate effects (LÓPEZ ET AL. (1983), LÓPEZ (1977)). This means, that the development of the observed systems, here the clusters, is proportional to their actual growth stage. As an explanation, two hypotheses are proposed by LÓPEZ (1977). One of them is related to the growth process of cloud parcels where growth occurs by a random process that obeys the law of proportionate effects, i.e. growth is a random proportion of the element's size. The other hypothesis refers to a formation process for clouds, in which clouds are formed by a merging of convective elements. This implies that larger elements grow more rapidly than smaller ones which again constitutes a growth process according to the law of proportionate effects. Both mechanism produce populations whose size is lognormal distributed.

The observed power-law distribution for the total area size may, according to CRAIG AND COHEN (2006), result from non-ideal behaviour in the mass flux but also from different processes affecting cloud size, including interactions of clouds.

The shape of the individual clusters is well represented by ellipses with a mean ellipticity of 0.58. This was previously reported by other authors such as FERAL ET AL. (2000). While the individual clusters move with the mean wind field, they are not oriented in a specific way. The frequency distribution of orientation with respect to the mean wind flow shows no preferred direction. Only if clusters  $< 100 \text{ km}^2$  are eliminated, a preferred orientation is observable, rotated at around  $20^\circ$

## Chapter 5. Geometry

---

relative to the mean flow (counter-clockwise).

The AIRR per cell as well as the area per cell increase with increasing cell number. At a cell number  $p = 20$ , the AIRR per cell show saturation effects such that additional cells do not increase the AIRR per cell. For the area per cell saturation effects occur only for cell number of  $p \approx 40$ . The most effective clusters in terms of AIRR per area are those with 25 embedded cells. This saturation effect has not been observed before and may be explained with an equilibrium stage reached at that point of growth. According to EMANUEL (1997), laboratory convection is often viewed as a statistical equilibrium process in which the statistical properties of convection are regarded as having reached an equilibrium with the external forcing. Statistical equilibrium forms the basis for the assumption that the statistical properties of a small-scale process can be uniquely related to properties of a larger-scale process with which it interacts. Trade cumulus and stratocumulus boundary layers are usually modelled as equilibrium processes, but controversy remains about whether or to what extent ordinary deep precipitating convection can be regarded as equilibrium process. Two equilibrium assumptions are discussed by EMANUEL (1997): The first sees water in an equilibrium stage, which means it is processed by convection at the rate at which it is supplied by large-scale processes. The other regards the buoyant energy produced by large-scale processes being balanced by dissipation insight clouds. While the water equilibrium assumption proved to be a deficient concept, because the time scale of water vapour adjustment in a convective environment is quite long, the energy equilibrium assumption turned out to be true on sufficiently large space and time scales but, however, not for individual convection cells. The here considered clusters usually consist of several embedded convection cells, resulting in an area which might be large enough for a practicability of the energy equilibrium assumption. According to CRAIG AND COHEN (2006), a necessary condition for convection in a finite region to be in equilibrium with the average forcing over that region is that the region with a size  $\Delta x$  be larger than the mean cloud spacing  $L$  with

$$L = (A / \langle N \rangle)^{0.5} \quad (5.9)$$

$A$  is hereby the size of the area containing an average of  $\langle N \rangle$  clouds which are in the present case represented by the individual convection cells within a cluster. Considering for example a 20-cells cluster, which is the cluster size where saturation effects were observed. As a convection cell was found to be in average  $29 \text{ km}^2$  large, this results in an area of almost  $800 \text{ km}^2$  for a cluster. The mean cloud spacing  $L$  is accordingly  $3.7 \text{ km}$  and thus less than the considered region size. Thus, this precondition for the practicability of the equilibrium assumption is fulfilled, which implies that the clusters may reach their equilibrium stage when they contain at least 20 individual cells.

# Chapter 6

## Temporal development

The main part of this thesis is covered by the investigation of the temporal development of the clusters identified in the post-frontal precipitation field. The time series of properties like the area or the area integrated rain rate (AIRR) were calculated based on a tracking of clusters in the radar data. So far, only one study is known where the temporal development of convective structures in the radar data is investigated in the same way. LÓPEZ ET AL. (1983) studied the phenomenological growth and development process of radar echoes in South Florida, including growth curves for cell area and reflectivity. As in the present thesis, a cell was identified as a maximum of radar reflectivity within an area of precipitation echoes in the radar data. The data was derived from two radar stations covering a region of almost 36 000 km<sup>2</sup>. Besides the 5 min radar reflectivity values, echo heights were used for the analysis. The study of LÓPEZ ET AL. (1983) aimed at a characterisation of convective clouds in a higher latitude tropical region to provide background knowledge of convective clouds against which hypothesized effects of dynamic cloud seeding should be assessed. Amongst others, the scale interactions between different scales of convection were investigated as well as typical formation and growth mechanism of showers. The focus was thereby on undisturbed synoptic situations, i.e. days in which clouds develop in an air mass favourable for convection and were forced by the undisturbed Florida sea breeze. This way, the large day-to-day variation in the strength and extent of shower activity observed in that region was eliminated.

In the present study, the analysis is in a similar way restricted to one synoptical situation, the convective precipitation field in the rear of a cold front in the mid-latitudes which reveals a similar structure for different days. That post-frontal precipitation field has been analysed in previous studies with respect to its geometrical structure. Concerning the temporal development of the individual small-scale structures within that precipitation field, no study is known. The aim of the investigations is an analytical description of the temporal development of the precipitation structures, in addition to the simple functions which were found by THEUSNER (2007) to describe

the geometrical structure of the precipitation field. A thorough description of the precipitation structures and their temporal development could help to improve the understanding of the small-scale convection field and enable a numerical simulation, for example on a stochastic basis. The latter can be extended to develop a forecast scheme for post-frontal shower precipitation based on the findings on the geometrical structure and the temporal development.

The results on the temporal development of area and AIRR for single-cell-tracks, which grow only by areal growth without a change in the cell number, can be found in WEUSTHOFF AND HAUF (2008a). Nevertheless, the procedure and results are presented here for all three track types together. In the following, the temporal development of different variables characterising a cluster is determined. The time series for area and AIRR are presented in Section 6.1, including a description of the procedure. Section 6.2 deals with the area and time integrated rain sum which is simply the AIRR time series integrated over the respective life span. In Section 6.3, additional investigations are presented, namely the mean time series of the AIRR per normal area and those of the cell number. Finally, a short discussion on the results is given in Section 6.4.

### 6.1 Temporal development of area and AIRR for three different track types

The set of tracks that form the basis for the present analysis were identified by a tracking algorithm which was applied to the 5 min RZ composite radar data for 17 days in 2004 and 2006 (WEUSTHOFF AND HAUF 2008b). Three track types were distinguished by means of the developments' complexity (single-cell-, single-cluster- and multi-cluster-tracks). They were introduced in Section 3.2.2. Altogether, more than 81 000 tracks were analysed regarding the temporal development of the area size and the AIRR over their whole life span. Three examples of each track type are given in Appendix A (Figure A.1 to A.9), showing the individual area and AIRR development as well as the footprint of the track.

Based on the seemingly stochastic nature of post-frontal showers, it is assumed that all tracks of a specific life span are members of the same population. The mean characteristics are therefore determined with respect to the life span, noting that the latter varies largely even within each track type. For each life span  $l$ , the mean development of the respective variable (area, AIRR) is determined as described in Section 6.1.1. The result of this procedure is one averaged time series for each track type and each life span, averaged over all days. Those time series are then normalised in two steps; the time is divided by the life span  $l$  and the amplitude by the maximum amplitude  $A_{k,l}$ , i.e. respectively the maximum area or AIRR of the mean time series of track type  $k$  and life span  $l$ .



### 6.1.1 Determination of mean time series and normalisation

For each day and each track type mean time series are determined for the area integrated rain rate distribution ( $\bar{r}(t)$ ) and the area distribution ( $\bar{a}(t)$ ). The determination and normalisation of the time series is the same for both variables and is thus described in general for a function  $\bar{f}(t)$  which then has to be replaced by the respective parameter.

1. All tracks are sorted by track type  $k$ . Three different track types are distinguished (cf. Chapter 3.2.2): single-cell-tracks, single-cluster-tracks and multi-cluster-tracks ( $k = 1,2,3$ ).
2. Each of those track types is then sorted by life span  $l$ . For the analysis, only short life spans till  $l=15$ , with a relative frequency of 0.001 ( $k = 1$ ), 0.01 ( $k = 2$ ) and 0.02 ( $k = 3$ ), are investigated. Tracks with a life span  $l > 15$  were omitted for statistical reasons.
3. The number of tracks with life span  $l$  on each single day  $m$  and for track type  $k$  has to be determined:  $n_{k,l,m}$ . The sum for all days ( $n_{k,l} = \sum_{m=1}^{17} n_{k,l,m}$ ) can be found in Table 6.1.
4. Calculation of the mean development  $\bar{f}_{k,l,m}(t)$  for each track type  $k$ , life span  $l$  and day  $m$ . Thereby, one mean value for each time step  $t$  is determined (see also Figure 6.1):

$$\bar{f}_{k,l,m}(t) = \frac{1}{N} \cdot \sum_{i=0}^N f_{k,l,m,i}(t), \quad (6.1)$$

with  $N = n_{k,l,m}$ .

Thus, one mean time series for each life span, each considered day and each track type is derived.

5. Calculation of the mean time series for all days  $\bar{f}_{k,l}(t)$ , for each track type  $k$  and each life span  $l$ , out of the mean time series for the individual days ( $\bar{f}_{k,l,m}(t)$ , see also Figure 6.3 (a)–(c)):

$$\bar{f}_{k,l}(t) = \frac{1}{M} \cdot \sum_{m=1}^M \bar{f}_{k,l,m}(t), \quad (6.2)$$

with  $M = \text{Max}(m) = 17$ .

6. Normalisation of the time  $t$  with the respective life span  $l$  and thus deletion of that discrimination; for  $l = 3, \dots, 15$ .

$$t^* = \frac{t}{l} \quad (6.3)$$

## Chapter 6. Temporal development

---

The density characteristic of  $\bar{f}(t)$  leads to an integration constraint:

$$\bar{f}_{k,l}^*(t^*) \cdot dt^* = \bar{f}_{k,l}(t) \cdot dt \quad (6.4)$$

$$\bar{f}_{k,l}^*(t^*) = \bar{f}_{k,l}(t) \cdot \frac{dt}{dt^*} \quad (6.5)$$

$$\frac{dt}{dt^*} = l \quad (6.6)$$

The normalised function then reads as follows:

$$\bar{f}_{k,l}^*(t^*) = \bar{f}_{k,l}(t) \cdot l \quad (6.7)$$

7. Normalisation of amplitude with the maximum amplitude  $A_{k,l}^*$ :

$$\langle \bar{f}_{k,l}^*(t^*) \rangle = \frac{\bar{f}_{k,l}^*(t^*)}{A_{k,l}^*} \quad (6.8)$$

with

$$A_{k,l}^* = \max(\bar{f}_{k,l}^*(t^*)) \quad (6.9)$$

$$= \max(\bar{f}_{k,l}(t) \cdot l) \quad (6.10)$$

$$= \max(\bar{f}_{k,l}(t)) \cdot l \quad (6.11)$$

$$= A_{k,l} \cdot l \quad (6.12)$$

For the sake of clarity, definitions of the variables are listed in the following:

$\bar{\mathbf{f}}_{\mathbf{k},\mathbf{l},\mathbf{m}}$  mean parameter development for track type  $k$  and life span  $l$  for individual days  $m$  [unit of  $f$ ]

$\bar{\mathbf{f}}_{\mathbf{k},\mathbf{l}}$  mean parameter development for track type  $k$  and life span  $l$  for all days [unit of  $f$ ]

$\bar{\mathbf{f}}_{\mathbf{k},\mathbf{l}}^*$  mean parameter development for track type  $k$  and life span  $l$  for all days, normalised with life span [unit of  $f$  per unitless time]

$\langle \bar{\mathbf{f}}_{\mathbf{k}}^* \rangle$  mean parameter development for track type  $k$ , normalised with life span and with maximum amplitude  $A_{k,l}^*$  [unitless]

$\mathbf{t}$  time [5 min]

$\mathbf{l}$  life span [5 min]

$\mathbf{t}^*$  time normalised with life span (Equation 6.3) [unitless]

$\mathbf{A}_{\mathbf{k},\mathbf{l}}$  maximum amplitude of  $\bar{f}_{k,l}$  for track type  $k$  and life span  $l$  [unit of  $f$ ]

## Chapter 6. Temporal development

---

$A_{k,l}^*$  maximum amplitude of  $\bar{f}_{k,l}^*$  for track type  $k$  and life span  $l$  [unit of  $f$  per unitless time]

$k$  track type,  $k = 1,2,3$

$m$  day,  $m = 1, \dots, 17$

$n_{l,k}$  number of tracks of track type  $k$  with life span  $l$

The determination of the mean temporal development of each variable is done in two steps (step 4 and 5 in the procedure). In a first instance, all tracks of a specific track type  $k$  and life span  $l$  are averaged for each day. An example is given in Figure 6.1 by means of tracks with a life span of  $6 * 5$  min on 24 September 2004. On this day, 280 tracks with the respective life span were available. The averaging was done for each time step separately, leading to five mean values in this example and consequently to five coefficients of variation. The frequency distribution of AIRR values for the five time steps of the example are shown in Figure 6.2. The frequency distributions reveal a skewness to the left. Nevertheless, the mean value was used for the analysis. The deviations from the mean values in this first averaging step provide information on the scatter around the mean for individual days. The number  $n_{l,k}$  of tracks over which the averaging was applied varies from day to day as well as between different track types and life spans (see Table 6.1).

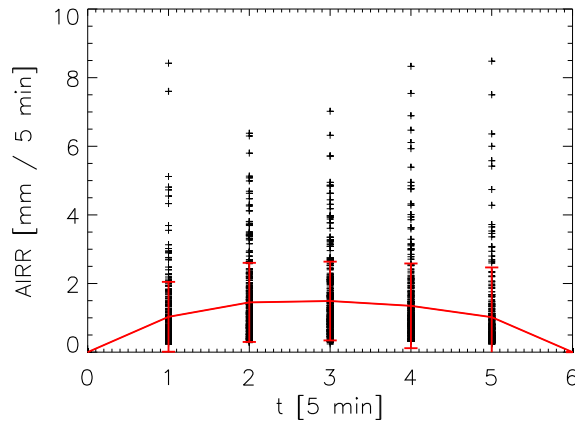


**Figure 6.1:** Example for the determination of the mean temporal development of AIRR for single-cell-tracks with a life span  $l = 6 * 5$  min, for 24 September 2004 (Step 4 in the procedure). The number of single-cell-tracks with  $l = 6 * 5$  min available for that day is 280. The red line represents the mean AIRR development, while the bars denote the standard deviations for each time step which is in average 1.2 mm per 5 min for this case.

Secondly, the whole set of mean time series derived for the individual days is averaged to determine one mean time series for each track type and life span. The scatter around that mean time series reveals the day-to-day variation. The number  $M$  of tracks over which is averaged in this step is constant ( $M = 17$ ).

## Chapter 6. Temporal development

---

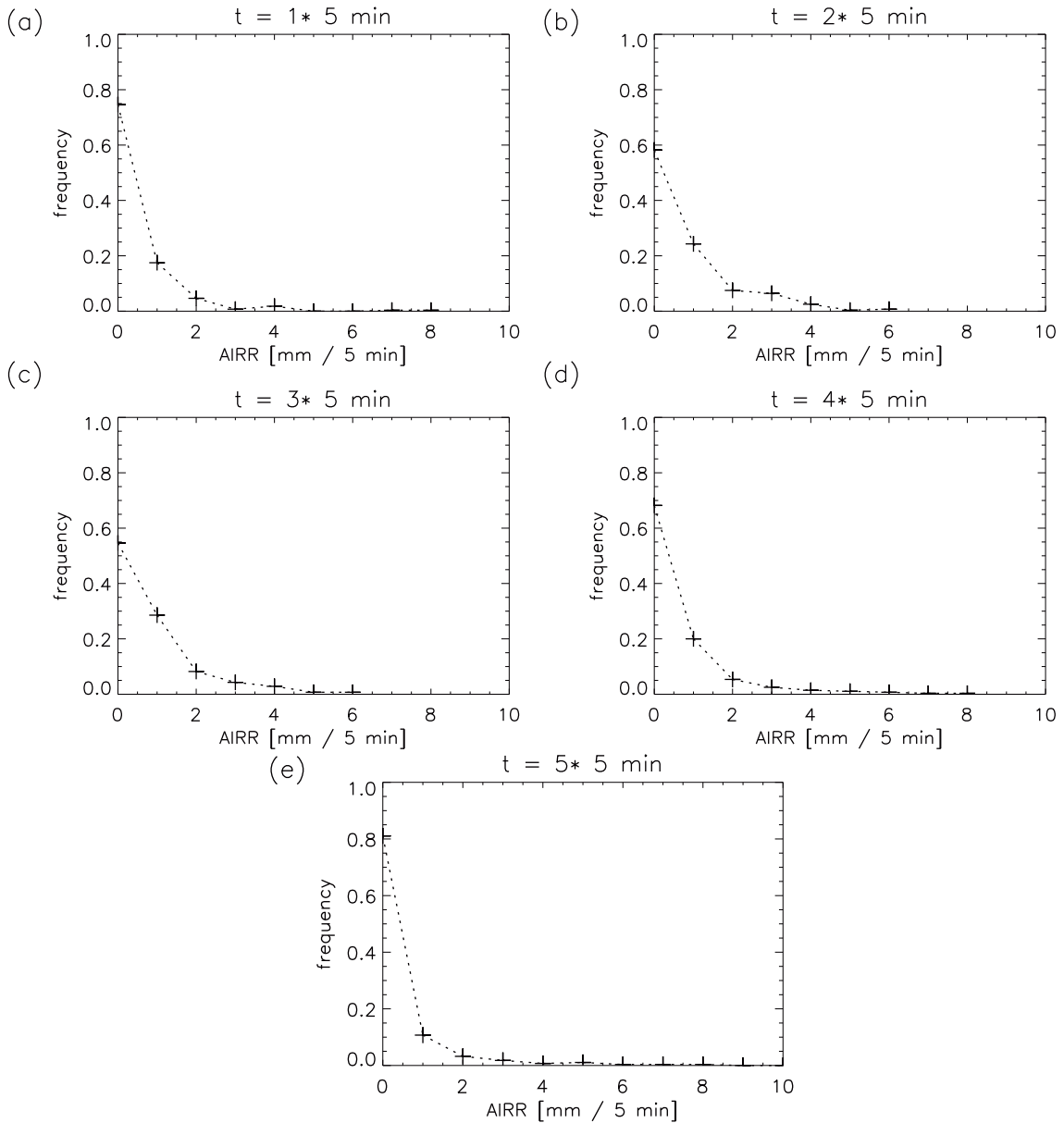


**Figure 6.2:** Frequency distribution of the AIRR values for the five different time steps ( $t = 1, \dots, 5 * 5 \text{ min}$ ) of the example presented in Figure 6.1. Based on those distributions for each time step, the mean time series were derived.

The coefficients of variation for both averaging steps are given in Appendix E in form of a frequency distribution. The typical coefficients of variation for each track type and each variable, which are presented in Table 6.2, are determined by the median as the frequency distributions show skewness to the left. Almost all coefficients of variation have values of less than 1. The values derived in the first step are larger than those obtained in the second step. Furthermore, the coefficients of variation increase with increasing track type number. The values for the area time series are lower than those derived for the AIRR time series. This leads to the conclusion

## Chapter 6. Temporal development

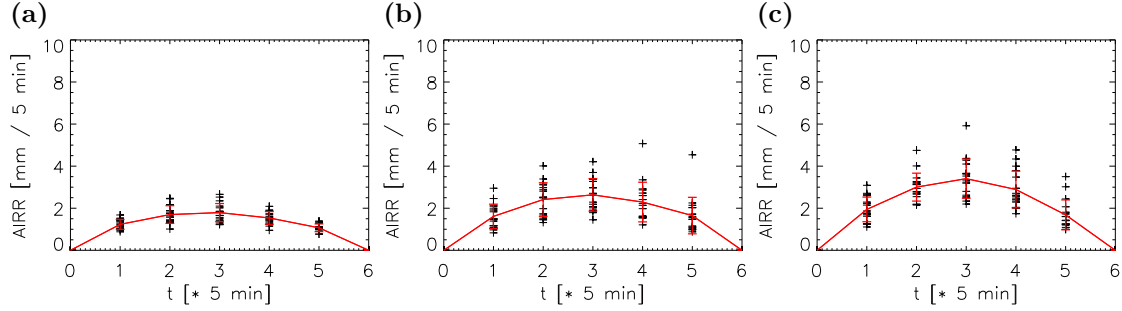


**Figure 6.3:** Example for the determination of the mean temporal development of AIRR for (a) single-cell-tracks, (b) single-cluster-tracks and (c) multi-cluster-tracks with life span  $l = 6 * 5$  min for each day and mean of all days according to Step 5 in the procedure (red line). The bars display the standard deviations. The mean standard deviation is for single-cell-tracks 0.26 mm per 5 min, for single-cluster-tracks 0.66 mm per 5 min and for multi-cluster-tracks 0.63 mm per 5 min.

that either quantitative precipitation estimation by radar is still limited in quality (see also Section 3.1.2) or the AIRR development is more variable than the area development.

In summary, the mean AIRR time series derived in the present study show variances around the mean values at each time step up to nearly the total dimension of the mean value. The area time series vary by half the total value of the mean time series.

$l$ [ $\cdot 5$ min]	$n_{1,1}$	$n_{1,2}$	$n_{1,3}$
3	28 775	2 498	969
4	11 285	1 926	1 409
5	5 447	1 466	1 420
6	2 916	1 096	1 342
7	1 742	794	1 186
8	1 051	615	1 022
9	651	478	869
10	418	385	868
11	284	307	672
12	194	224	613
13	138	195	563
14	122	165	547
15	76	129	448
$15 < l < 50$	264	615	4 998
total	53 372	10 894	16 926

**Table 6.1:** Total number of tracks  $n_{l,k}$  with life span  $l$  for the three different track types: single-cell-tracks ( $k = 1$ ), single-cluster tracks ( $k = 2$ ) and multi-cluster tracks ( $k = 3$ ).

		<b>k = 1</b>	<b>k = 2</b>	<b>k = 3</b>
<b>area</b>	Step 1	0.52	0.57	0.84
	Step 2	0.38	0.45	0.53
<b>AIRR</b>	Step 1	0.84	0.79	1.06
	Step 2	0.69	0.67	0.68

**Table 6.2:** Coefficients of variation for the two averaging steps. Displayed are the median values for the two variables area and AIRR and the three track types  $k$ .

### 6.1.2 Fitting of normalised time series

By normalising the mean area time series, which were derived for the different life spans and track types, with the respective life span  $l$  and subsequently with the maximum amplitude  $A_{k,l}^*$ , all time series reveal a surprisingly common shape. The same is observed for the AIRR time series, with the whole set of mean time series following the same parabolic shape. This has not been observed before and implies a common underlying principle governing the temporal development of the small-scale structures within the post-frontal precipitation field. The normalised time series for life spans  $l = 3, \dots, 11$  and the three different track types are plotted in Figure 6.4 (a) for the AIRR and in Figure 6.4 (b) for the area size. The basic structure of the temporal development is the same for all track types and life spans, showing in a first approximation a parabolic shape. Both the area and the AIRR time series were fitted to two different functions which are also displayed in the figures: a sinus function in a general form, involving an exponent  $d_k$  of the sinus (Equation 6.13), and a standard parabola without an independent parameter (Equation 6.14).

$$\langle \bar{\mathbf{f}}_k^*(\mathbf{t}^*) \rangle = \sin(\pi \cdot \mathbf{t}^*)^{d_k} \quad (6.13)$$

$$\langle \bar{\mathbf{f}}_k^*(\mathbf{t}^*) \rangle = 4 \cdot (\mathbf{t}^* - \mathbf{t}^{*2}) \quad (6.14)$$

The exponent  $d_k$  in Equation 6.13 was determined by a least-squares fit for each track type. The values are given together with the standard deviation and the correlation for both AIRR and area in Table 6.3. The normalised time series of the mean AIRR development as well as that of the area development are nearly equally well represented both by a sinus function and a parabola. This can be seen from Figures 6.4 (a) and (b) and from the values for the coefficient of determination  $R^2$  (Table 6.3). Although the  $R^2$  values for the sinus function are in both cases superior, the parabola was chosen to represent the AIRR development  $\bar{r}_{k,l}(t)$  as it

## Chapter 6. Temporal development

---

is easier to handle and the differences in the  $R^2$  values are marginal. In the case of the area development  $\bar{a}_{k,l}(t)$ , the time series is apparently better represented by a sinus function with  $R^2 \approx 0.99$  for all three track types. Thus, for the temporal development of each of the two parameters (AIRR, area) one simple function was found to describe all three track types and all considered life spans, if normalised by life span and maximum rain rate. Despite the variety of individual developments (see for example Appendix A) and the different characteristics of the three track types (see Section 3.2), all track types can obviously be attributed to the same underlying principles.

Through the normalisation of the time series, it was possible to find a description for the temporal development of different parameters for all track types and different life spans together. The normalisation thus served the purpose of identifying a common structure for the whole set of tracks. For an exact approximation, the non-normalised functions will be considered in the following. Therefore, the close match of the normalised time series is ignored and additional parameters are included in the equations (see Equations 6.15 and 6.20). Assuming a dependency of the total values for the area and AIRR development on the life span and the track type, the additional parameters ( $c_k$ ,  $g_k$  and  $h_k$ ) will be determined by fitting the mean time series of the respective life span for each track type to the respective equations. The results are presented in the following Section 6.1.3.

	sinus		parabola		
<b>area</b>	<b><math>d_k</math></b>	<b><math>\sigma</math></b>	<b><math>R^2</math></b>	<b><math>\sigma</math></b>	<b><math>R^2</math></b>
1) single-cell-tracks	0.45	0.037	0.992	0.136	0.936
2) single-cluster-tracks	0.63	0.041	0.990	0.090	0.971
3) multi-cluster-tracks	0.73	0.045	0.988	0.058	0.982
<b>AIRR</b>	<b><math>d_k</math></b>	<b><math>\sigma</math></b>	<b><math>R^2</math></b>	<b><math>\sigma</math></b>	<b><math>R^2</math></b>
1) single-cell-tracks	0.62	0.097	0.944	0.120	0.917
2) single-cluster-tracks	0.76	0.065	0.974	0.070	0.972
3) multi-cluster-tracks	0.72	0.070	0.970	0.080	0.963

**Table 6.3:** The parameters for curve fitting with sinus (Equation 6.13) and parabola (Equation 6.14) for normalised time series (i.e.  $l = 1$ ,  $A_k = 1$ ). The parameter  $d_k$  of the sinus, which is constant for each track type, was revealed by a least-squares fit. Shown are standard deviation  $\sigma$  and coefficient of determination  $R^2$  for the different track types.

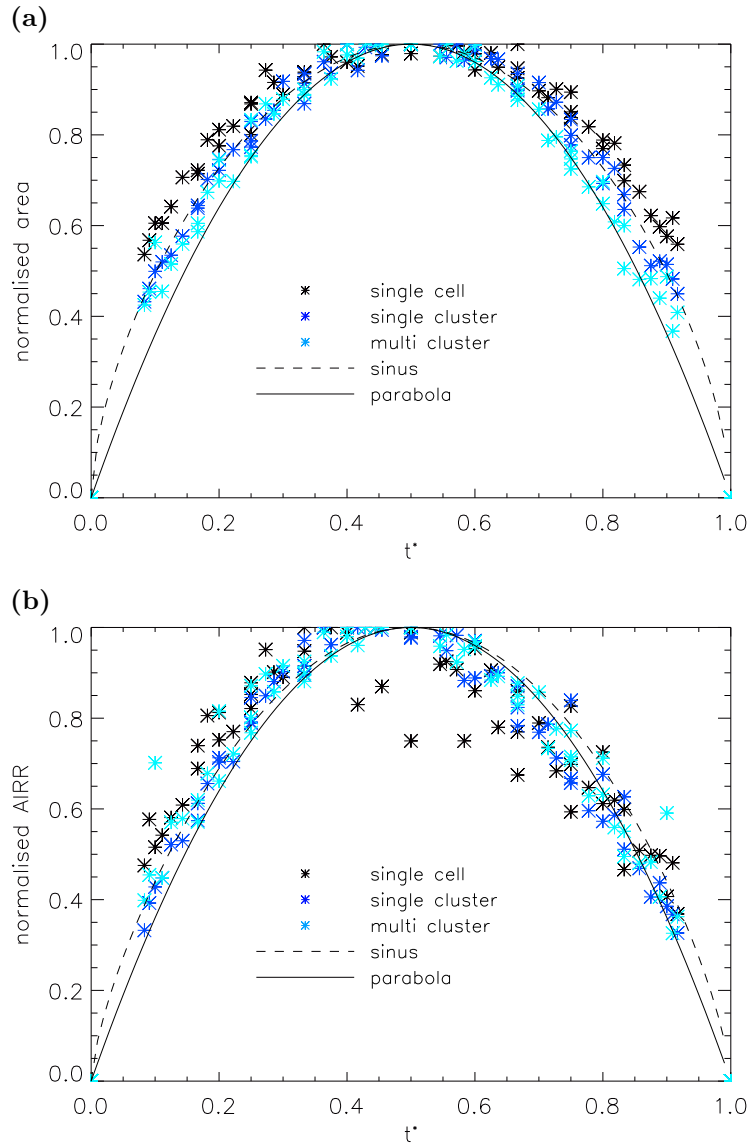


**Figure 6.4:** Average temporal development of (a) area and (b) AIRR for the different track types, normalised with life span and maximum amplitude. The sinus is plotted with  $d_k = 0.60$  for area and  $d_k = 0.70$  for AIRR.

### 6.1.3 Life span dependency of non-normalised functions

For an exact approximation of the mean AIRR and area time series determined for the different track types and life spans, the **non-normalised** versions of the basic equations found by means of the normalised time series are considered now:  $\bar{a}_{k,l}(t)$  (Equation 6.15) and  $\bar{r}_{k,l}(t)$  (Equation 6.20). Those non-normalized functions include additional parameters, which were determined for each life span in order to evaluate the dependencies of the above derived basic functions on the track type and the life span. The additional parameters  $c_k$  for the sinus and  $g_k$  and  $h_k$  for the parabola



## Chapter 6. Temporal development

---

were determined separately for each track type and each variable (AIRR, area) as a function of life span. The values for individual life spans are given in Appendix D (Table D.1 – D.6). The parameters were calculated for each of the variables fitted to both the sinus and the parabola. In the following, for each of the two variables only the function is introduced that was found to describe the time series best. Thus, the area development is described by the sinus, while the AIRR development is approximated by the parabola.

### Area development

For the area development  $\bar{a}_{k,l}(t)$ , the sinus was chosen because the correlation revealed higher values than that for the parabola fit. This is especially true for single-cell-tracks and single-cluster-tracks (see Table 6.3). The mean temporal development of the area for track type  $k$  and life span  $l$  can hence be described by a sinus function of the form

$$\bar{a}_{k,l}(t) = c_k(l) \cdot \sin\left(\pi \cdot \frac{t}{l}\right)^{d_k} \quad (6.15)$$

with  $t \leq l$ . The exponent  $d_k$  is constant for each track type (see Table 6.3). In a different approach, where  $d_k$  was determined as a function of life span, the exponent was also found to be constant for each track type revealing nearly the same values as derived in Section 6.1.2. The respective values of  $d_k$  can be found in Appendix D (Table D.4 - D.6). The additional parameter  $c_k$  is equivalent to the maximum amplitude  $A_{k,l}$  (see Figure 6.5 (b)). The values for the specific life spans derived by a least-squares fit and the quality measures can again be found in Appendix D (Table D.4 - D.6). For  $c_k(l)$ , which is equivalent to the maximum amplitude  $A_{k,l}$ , a quadratic function was derived (Equation 6.16, Figure 6.5 (a)). The constants  $\alpha_{i,k}$  are given in Table 6.4.

$$c_k(l) = \alpha_{1,k} + \alpha_{2,k} \cdot l + \alpha_{3,k} \cdot l^2 \quad (6.16)$$

$$= A_{k,l} \quad (6.17)$$

As a consequence, the mean temporal development of the area of a track can be described by a simple sinus function of only life span  $l$  and track type  $k$ . The final equation for the area time series reads:

$$\bar{a}_{k,l}(t) = A_{k,l} \cdot \sin\left(\pi \cdot \frac{t}{l}\right)^{d_k} \quad (6.18)$$

$$\bar{\mathbf{a}}_{\mathbf{k},\mathbf{l}}(\mathbf{t}) = (\alpha_{1,\mathbf{k}} + \alpha_{2,\mathbf{k}} \cdot \mathbf{l} + \alpha_{3,\mathbf{k}} \cdot \mathbf{l}^2) \cdot \mathbf{sin}\left(\pi \cdot \frac{\mathbf{t}}{\mathbf{l}}\right)^{d_{\mathbf{k}}} \quad (6.19)$$

## Chapter 6. Temporal development

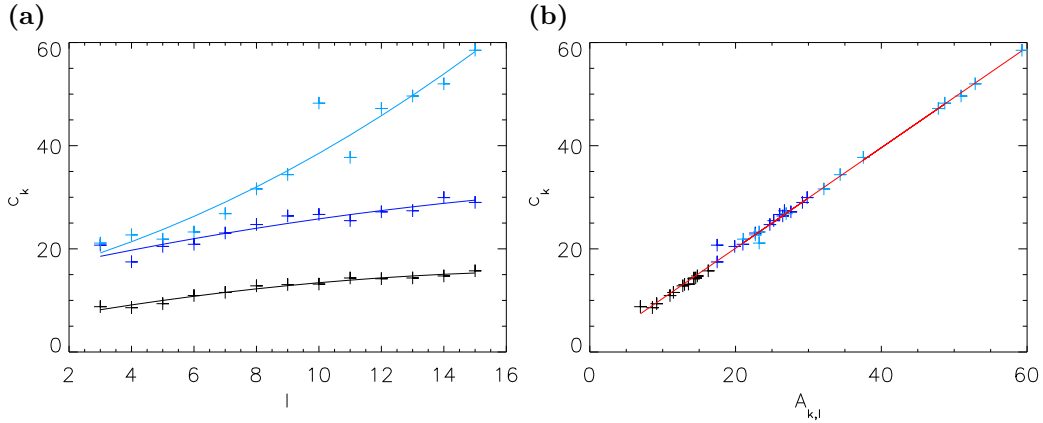


**Figure 6.5:** (a) Parameters  $c_k$  for the three different track types as a function of life span. (b) Parameter  $c_k$  of the least-squares fitted functions for each life span  $l$  plotted against empirical determined amplitudes  $A_{k,l}$  of the mean time series. The slope of the regression is approximately 1 and the correlation coefficient  $\mathcal{R} = 0.998$ .

$\mathbf{k}$	$\alpha_{1,\mathbf{k}} [km^2]$	$\alpha_{2,\mathbf{k}} [km^2/5min]$	$\alpha_{3,\mathbf{k}} [km^2/(5min)^2]$
1) single-cell-tracks	5.02	1.15	-0.03
2) single-cluster-tracks	14.65	1.38	-0.03
3) multi-cluster-tracks	13.92	1.47	0.10

**Table 6.4:** The parameters of the area time series fitted to a sinus function for individual life spans (Equations 6.19).

### AIRR development

The AIRR time series was found to be best described by the parabola. The correlation was rarely different for the fit with both functions (sinus, parabola), except for single cells where the sinus would have been slightly better. Despite that, the parabola was chosen as it is easier to handle, for example concerning the integration in Section 6.2.

The basic equation for different life spans and all track types includes the two additional parameters  $g_k$  and  $h_k$ :

$$\bar{r}_{k,l}(t) = 4 \cdot \frac{g_k}{h_k^2} \cdot (h_k \cdot t - t^2) \quad (6.20)$$

The parameter  $g_k$  represents the maximum amplitude  $A_{k,l}$  of the AIRR time series (cf. Figure 6.6 (c)). Its dependency on the life span was determined for the mean time series of each life span by the least-squares method. The values for the specific life spans and the quality measures can be found in Appendix D (Table D.1 - D.3).

## Chapter 6. Temporal development

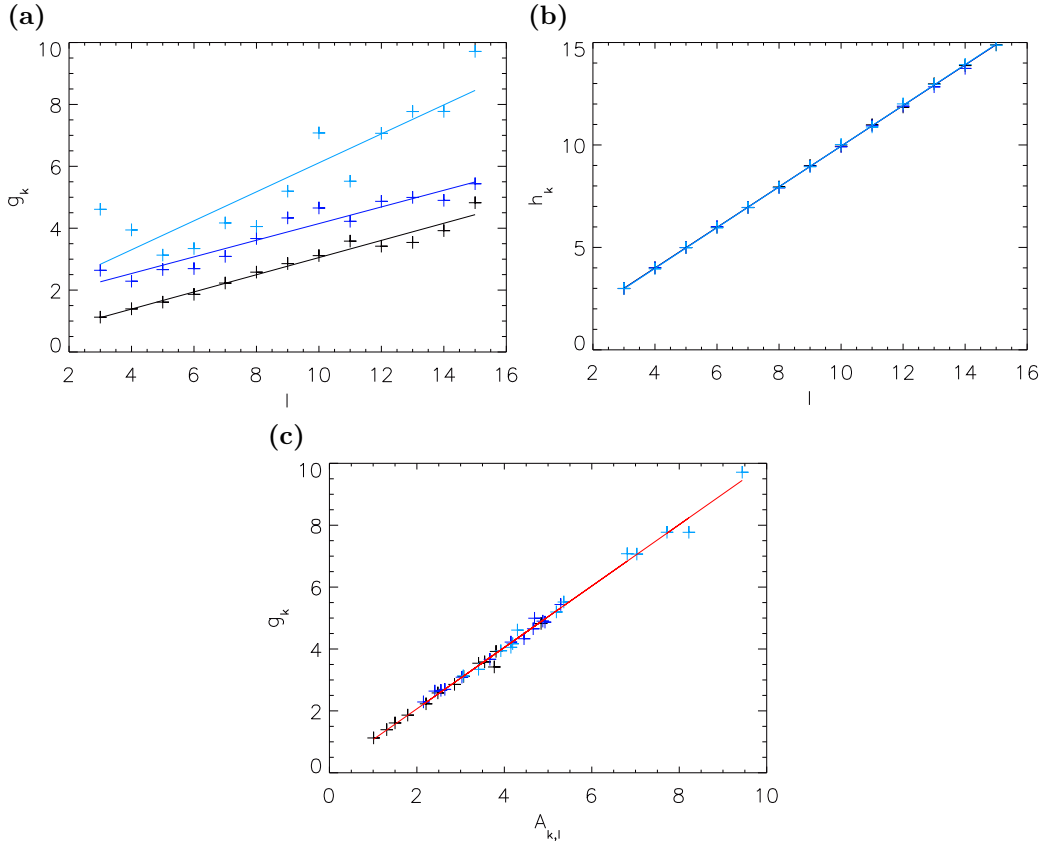


**Figure 6.6:** (a) and (b) Parameters  $g_k$  and  $h_k$ , respectively, of the AIRR time series (Equation 6.20) for the three different track types as a function of life span. (c) The parameter  $g_k$  of the least-squares fitted functions for each life span  $l$  plotted against empirical determined  $A_{k,l}$  of the mean AIRR time series. The regression has a slope of approximately 1 with a correlation coefficient of  $\mathcal{R} = 0.997$ .

It was found that  $g_k$  increases linear with  $l$  (cf. Fig. 6.6 (a), Equation 6.23) for each track type. The respective constant  $\beta_k$  is given in Table 6.5. As already stated above, the regression was hereby only fitted to tracks with a life span of less than  $16 \cdot 5$  min. Not surprisingly, the parameter  $h_k$  agrees with the life span  $l$  with a correlation coefficient of  $\mathcal{R} \cong 1.00$  (Equation 6.21, Figure 6.6 (b)).

$$h_k = l \quad (6.21)$$

$$g_k = A_{k,l} \quad (6.22)$$

$$= \beta_k \cdot l \quad (6.23)$$

Finally, the mean time series of the AIRR can be described as a function of life span only:

$$\bar{r}_{k,l}(t) = 4 \cdot \beta_k \cdot t \cdot \left(1 - \frac{t}{l}\right) \quad (6.24)$$

## Chapter 6. Temporal development

---

$$\bar{r}_{k,l}(t) = 4 \cdot \beta_k \cdot l \cdot \left( \frac{t}{l} - \frac{t^2}{l^2} \right) \quad (6.25)$$

The second version of the final equation reveals the basic result that the temporal development of the AIRR can be reduced to the life span. The time dependency as well as the amplitude are scalable with the life span and thus a reduction of variables is achieved. The only parameter determining the temporal development is the life span of the track.

	$\beta_1$	$\mathcal{R}$	$\beta_2$	$\mathcal{R}$	$\beta_3$	$\mathcal{R}$
(i)	0.28	0.984	0.27	0.962	0.47	0.892
(ii)	0.25	0.997	0.33	0.992	0.51	0.955

**Table 6.5:** Constant  $\beta_k$  [mm per (5 min)<sup>2</sup>] for the three track types, derived (i) from the AIRR time series (Equation 6.25) by means of the regression of  $g_k$  as a function of life span (Equation 6.23) and (ii) from the empirically derived values for the ATIRS (Section 6.2, Equation 6.30).

## 6.2 Area and time integrated rain sum

The integration of the mean AIRR time series as given in Equation 6.25 over the whole life span yields the mean area and time integrated rain sum (ATIRS)  $\bar{R}_{k,l}$ :

$$\bar{R}_{k,l} = \int_{t=0}^l \bar{r}_{k,l}(t) \cdot dt \quad (6.26)$$

$$= 4 \cdot \beta_k \cdot \int_{t=0}^l \left( t - \frac{t^2}{l} \right) \cdot dt \quad (6.27)$$

$$= 4 \cdot \beta_k \cdot \left[ \frac{1}{2} \cdot t^2 - \frac{1}{3 \cdot l} \cdot t^3 \right]_{t=0}^l \quad (6.28)$$

$$= 4 \cdot \beta_k \cdot \frac{1}{6} \cdot l^2 \quad (6.29)$$

$$\bar{R}_{k,l} = \frac{2}{3} \cdot \beta_k \cdot l^2 \quad (6.30)$$

$$= \frac{2}{3} \cdot A_{k,l} \cdot l \quad (6.31)$$

with

$\bar{\mathbf{R}}_{k,l}$  mean area and time integrated rain sum (ATIRS) for track type  $k$  and life span  $l$  [mm]

## Chapter 6. Temporal development

---

The analytically derived ATIRS shows a quadratic dependency on the life span (Equation 6.30). Consistently, the same quadratic function was found for the regression of the empirically derived precipitation sum as a function of life span, which is displayed in Figure 6.7. The values derived for the parameters  $\beta_k$  this way are given in Table 6.5. They only differ slightly from those calculated by means of the AIRR time series in Section 6.1.3.

In conclusion, the total rain sum a track produces in the course of its life only depends on the track type and within each track type on the life span in a simple quadratic form.

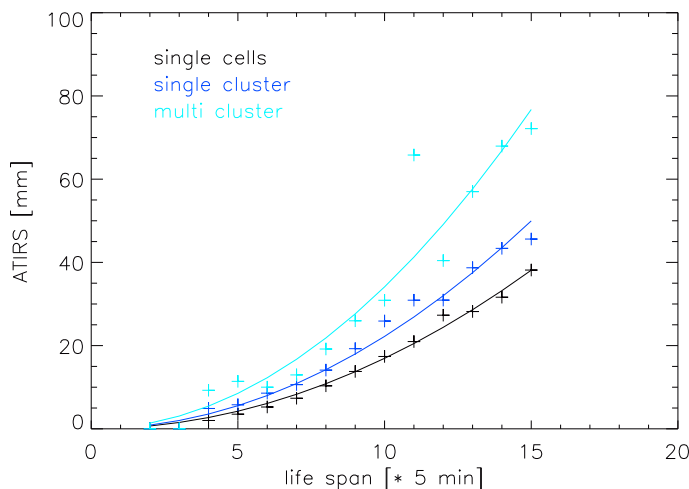


**Figure 6.7:** ATIRS plotted against life span for all three track types with quadratic regression plotted as solid lines (Eq. 6.30).

## 6.3 Additional investigations

In this section, some additional phenomenological investigations on the temporal development of post-frontal small-scale precipitation structures are presented. In the first part, the time series of the AIRR per area for all track types are described, followed by the cell number time series for single-cluster-tracks and multi-cluster-tracks.

### 6.3.1 AIRR per area

Both the area and the AIRR time series reveal a very similar shape. This raises the question whether the AIRR development may be caused mainly by areal growth. To test this hypothesis, the AIRR is normalised by the respective area, revealing the ratio  $q$  of those two variables:

$$q = \frac{r}{a} \tag{6.32}$$

## Chapter 6. Temporal development

---

From this ratio, the relation between the development processes of the parameters AIRR and area can be deduced. Figure 6.8 displays the average normalised time series of the AIRR per area  $\langle \bar{q}_k^*(t^*) \rangle$  for the different track types and life spans. It should be noted that the mean normalised time series of the ratio is derived through dividing the AIRR by the area, yielding the ratio  $q$ , before the averaging and normalisation is processed. However, assuming a similar development for both quantities, one would expect the ratio being constant over the whole time range. Instead, a variation is observable with skewness to the left, i.e. all track types show a strong increase of the AIRR per normal area in the beginning of the growth process, while the decrease of the ratio is apparently slower. The maximum AIRR per normal area is reached significantly before half the life time, i.e. earlier than the AIRR and the area itself reach their maximum values.

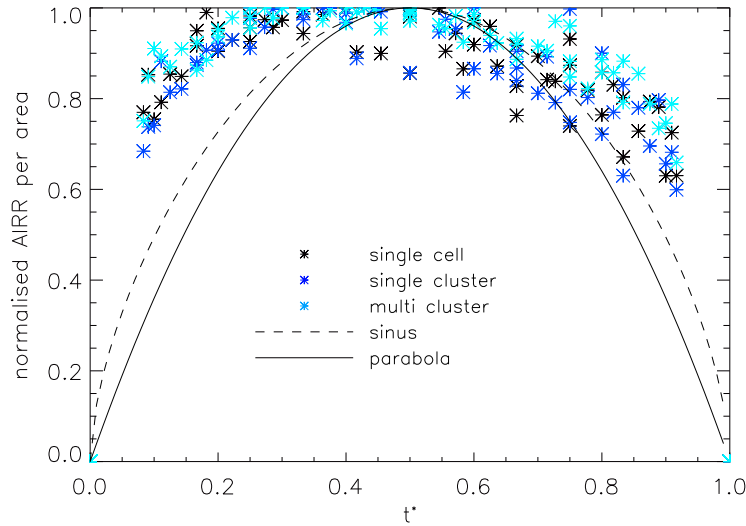


**Figure 6.8:** Average temporal development of the normalised AIRR per area ( $\langle \bar{q}_k^*(t^*) \rangle$ ) for the different track types.

One may conclude from these observations that AIRR and area grow differently during a life cycle. Rain intensity grows slightly faster than area size, while area size decreases slower than rain intensity. This asymmetry is hidden in the symmetric representation in Equations 6.13 and 6.14 and appears only if the ratio of both quantities is considered. The slight differences in the curves lead to an enhanced skewness with respect to the ratio of the two quantities.

### 6.3.2 Cell number development

In Section 2.1.2 the cluster growth was described in terms of cell number variations (*number growth*). Thus, the cell number is an important parameter with respect to the growth process. Therefore, a short discussion on the cell number development for the different track types is given. As single-cell-tracks are defined as being

## Chapter 6. Temporal development

---

composed of only one convection cell over their whole life span, the investigation is here restricted to the two other track types. The average time series for life spans of  $l = 3, \dots, 15$  are displayed in Figures 6.9 (a) and (b). Both track types show in average only a small number of embedded convection cells. While for the single-cluster-tracks the maximum cell number within a track is about 1.6, the multi-cluster-tracks reach a maximum cell count of about 2.7 cells.

Both track types show an increase in the maximum cell count for increasing life span. Especially the temporal development of the cell count for multi-cluster tracks-reveals a shape which is in line with that of the AIRR and the area time series. Only the mean curve for the life span  $l = 3 * 5$  min shows a little different behaviour reaching a maximum cell count of  $p = 2$ . The cell number may thus be a scale parameter for the area and AIRR time series, such that by reducing the variables to the values per cell the differences due to different life spans may be scaled down.

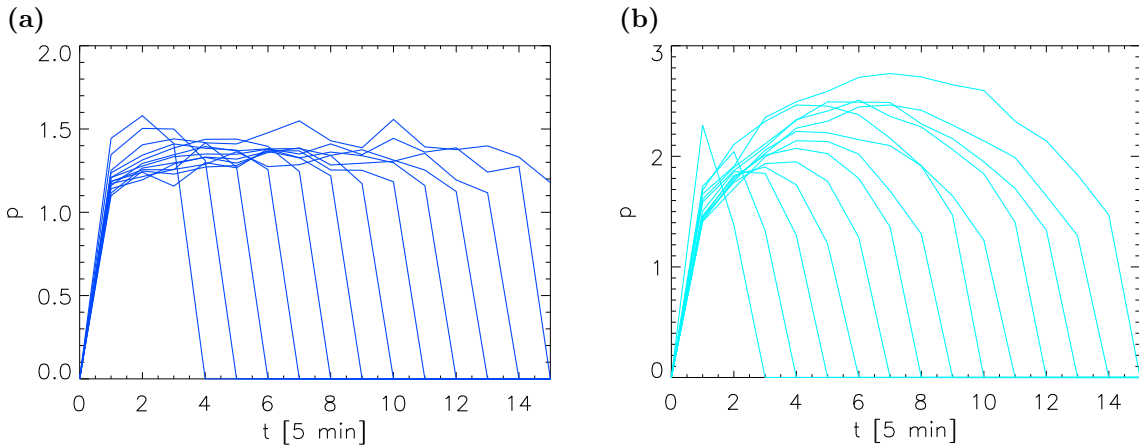


**Figure 6.9:** Average temporal development of cell number  $p$  for (a) single-cluster-tracks and (b) multi-cluster-tracks.

## 6.4 Discussion

The fact that the temporal development of convective showers depends on the life span is neither new nor surprising. LÓPEZ ET AL. (1983) already presented time series of the average area of convection cells for different life spans and observed a considerable increase of the maximum amplitude with cell duration. However, the form of this dependency has not been determined before.

Looking at individual tracks of all categories, significant differences in the time series are obvious (see Appendix A). Some of the tracks show their maximum rain rate at the end of their existence, while others have the maximum rain rate in the beginning of the development. Even some oscillating examples can be found with several maxima of rain rate occurring. Nevertheless, the mean time series show a

## Chapter 6. Temporal development

---

surprisingly smooth parabolic shape with a maximum at around half the life time. Thus, the time series reveals a symmetry with respect to the life span.

To summarise the findings, the normalised time series of the mean AIRR development as well as that of the area development are nearly equally well represented both by a sinus function and a parabola. The parabola was chosen to represent the AIRR development  $\bar{r}_{k,l}(t)$  as it is easier to handle and the differences in the quality measures for the fit with both functions (sinus, parabola) are marginal. In the case of the area development  $\bar{a}_{k,l}(t)$ , the time series is apparently better represented by a sinus function. The resulting non-normalised functions for both time series, including one additional parameter  $c_k$  for the sinus and two additional parameters  $g_k$  and  $h_k$  in the case of the parabola, finally depend only on the life span of the track. This way, simple equations for the temporal development of the AIRR (Equation 6.25) as well as of the area size (Equation 6.19) for all life spans were derived.

Apparently, the organisation scheme chosen for the analysis, i.e. (1) sorting the tracks by track type and then (2) each track type again by life span, turned out to be well chosen. The life span is the basic parameter for a description of the temporal development. It not only scales the time but also the amplitude of the time series, the latter of which is a simple function of life span  $l$ . Furthermore, the parabolic shape of the AIRR time series yields a simple relation between the ATIRS, the maximum amplitude and the life span of a track (Equation 6.31). Thus, the life span is the only parameter to be known. It can be estimated from the frequency distributions of life span for the individual track types which basically follow power laws.

The results enable an improved description of an ensemble of convective precipitation structures consisting of one or more individual convection cells and varying in space and time. The fundamental parameter of the simple functions found for the time series of area and AIRR is the life span which represents the only independent variable therein.

In addition, different slopes in the beginning of a tracks' development may be an indicator for the further cluster development. In the presentation of the non-normalised time series for the AIRR (see Figure 8.1), considerable differences in that growth stage are evident.



# Chapter 7

## Summary and conclusions

This thesis presents a phenomenological study of the complex structure of the convective precipitation field in the rear of cold fronts. The post-frontal convective precipitation field was analysed in an Eulerian approach (cell number distribution, cluster size distribution, area integrated rain rate per cell, cluster shape and motion) as well as in a Lagrangian-type analysis (temporal development of area integrated rain rate and area size, growth processes). The instantaneous radar data were analysed with respect to the geometrical structure and precipitation rate characteristics were determined. Diurnal cycles of specific parameters were calculated revealing a dominance of the typical diurnal variation of convective activity. In addition to such analyses of instantaneous data, the growth processes of clusters with respect to the number of embedded cells and the temporal development of their characteristics like size and rain rates were investigated. Although only Germany was considered, it is hypothesised that the results are also applicable to other areas within Central Europe. A difference in the spatial structure was observed in a previous study by THEUSNER (2007) for the German North Sea coast where coastal effects lead to a marked enhancement of convective activity.

As a reminder, the objectives of this thesis identified in Chapter 1 are repeated. In the following, the conclusions are presented beginning with the last objective.

1. Is it possible to derive a set of equations which describe the characteristics of the post-frontal precipitation field? What are the governing parameters?
2. How do the characteristics of the individual areas, like area size and rain rate, develop with time? Which analytical functions can be derived for the mean time series?
3. How can the rain rate characteristics be described?
4. Which shape can be assumed for the individual clusters in the precipitation field? And how are they related to the wind field?

5. Are the results of previous studies concerning the geometrical structure reproducible with the higher resolution RZ-composite?

### Geometry

It was shown that previous results on the geometric structure of post-frontal precipitation fields as presented by THEUSNER (2007) can be accurately reproduced with the higher resolution radar composite employed in the present study: the cell number distribution could be described by a power law and the cluster size distribution revealed a lognormal distribution for each cell number. The findings of both studies can thus be combined to provide a thorough description of the precipitation field. The question addressed in objective 5 can thus be answered positively.

Objective 4 dealt with the shape and orientation of the clusters within the precipitation field. The post-frontal precipitation field comprises several hundred clusters on each day, scattered over whole Germany. The individual clusters are well represented by ellipses with a mean ellipticity of 0.58. While for the whole set of clusters no preferred orientation was observed, clusters which occupy an area of more than 100 km<sup>2</sup> are preferably aligned in a direction around 20° relative to the mean flow (counter-clockwise). The small-scale structures within the precipitation field basically move with the mean 925 hPa wind field which was observed by visual inspection of the tracks path and comparison to the wind field.

The cell related area integrated rain rate (AIRR), defined as the total AIRR of a cluster divided by the number of embedded cells, and the equally defined area per cell showed an increase with the total cell number until an equilibrium stage was reached at  $p \approx 25$  for the AIRR and  $p \approx 40$  for the area size. This implies that individual cells enhance each other's productivity until beyond a certain cluster size saturation effects appear and additional convection cells show no cumulative effect. The prevailing convective activity is obviously in equilibrium with the average forcing over the considered region.

### Rain rates

The utilisation of the quantitative radar composite RZ allowed for a qualitative evaluation of rain rate characteristics within the precipitation field which was asked for in objective 3. The radar derived precipitation amounts were relatively low. Nearly 75 % of the detected rain rates had a value of 0.05 - 0.16 mm per 5 min while rain rates of more than 2.92 mm per 5 min were rarely observed. The daily precipitation sums revealed mainly values of less than 10 mm per square kilometre. The shower duration at a given pixel of one square kilometre was found to be about 18 min on average, the total precipitation time almost one hour. A shower was usually followed by a nearly 21 times longer period without precipitation.

### Growth processes

The growth process of convective clusters was analysed in terms of embedded convection cells, each of them represented by a maximum in rain rate. It is a combination of individual growth and interactions amongst different clusters such as merging and splitting. A simple growth model was proposed by WEUSTHOFF AND HAUF (2008b) based on transition probabilities from a cluster with  $n$  embedded convection cells to a cluster comprising  $m$  cells. Clusters were found to form as a single convection cell and grow by gaining one additional cell within a time step of 5 min. After a stage of stagnation, where the number of embedded cells does not change, they grow further or decrease in the same way by one maximum within a time step of 5 min. The disappearance of the clusters again takes place via the stage of single cells. The frequency distribution of the cell number for all clusters as well as those for new developed and dissolving clusters can be fitted by a power law (WEUSTHOFF AND HAUF 2008b); the same was observed for the life span. The occurrence of a power law is an indicator for scale invariant behaviour. This means, the characteristics of the distributions do not change when the scales are modified. One also speaks of self-similarity in this context.

The observations concerning the growth of clusters generally fit the properties of a Yule process, which is a widely applicable mechanism for generating power laws (CONCAS ET AL. 2006). The Yule process describes a mechanism for generating a population of entities, each having a property, which is characterized by an integer numeric value, like the cell number in the present case of the convective clusters. The key feature of this process is that entities increase their value at each time step with a certain probability in proportion to the value itself. Physically the growth may be explained by the cell dynamics which show updraughts that favour neighbouring growing cells but suppress those further away. In the case of the shower clouds this would imply that new shower cells grow preferably in the vicinity of existing cells or within an already existing cluster (WEUSTHOFF AND HAUF 2008b). However, the existence of preferred locations for the genesis of new cells was beyond the scope of this thesis and has therefore been left for future studies.

### Temporal development

The temporal development of characteristics like the area integrated rain rate and the area size of a cluster was analysed by means of radar data. This was done based on a tracking of individual clusters with time. A set of over 81 000 tracks was classified into three track types according to the complexity of their development: single-cell-tracks that stay single over their whole life span represent about 66 % of all tracks; single-cluster-tracks which only grow by internal growth by means of increasing or decreasing their cell number are the smallest group with 13 %; multi-cluster-tracks, with 21 % of all tracks the second largest group, show the most complex growth process including interactions amongst different clusters. Assuming

## Chapter 7. Summary and conclusions

---

that clusters with the same life span are members of the same population, each of those track types was additionally sorted by means of life span.

It was found that the mean temporal development of the AIRR and the area within a track is a simple function of track type and life span only. Hereby, the AIRR development is described by a parabola (Equation 6.25), while the area development is well represented by a sinus with an additional exponent, which is constant for each track type (Equation 6.19). Considering the variety of different individual time series (some examples are presented in Appendix A), the mean time series show a surprisingly smooth shape. Apparently, the life span is the basic parameter controlling the development of clusters within the post-frontal precipitation field.

As stated above, the frequency distribution of the life span fits a power law for the whole set of tracks. Considering the life spans of the individual track types only, the single-cell-tracks are also well represented by a power law with a correlation coefficient of nearly 1.00 but with a steeper slope, which is an indicator for the enhanced dominance of short life spans. The other two track types are better represented by a modified power law (Equation 3.2). Altogether, it can be summarised that the life span of all three track types as well as the whole track data set show frequency distributions which basically follow a power law. Short life spans clearly dominate in all track type classes. The parameter  $b$ , i.e. the exponent of the power law, varies from day to day. This variance was determined for the whole set of tracks without track type distinction. For a detailed sensitivity study based for example on the season, the number of analysed days is too low. Therefore, this is left for further studies. For the limited number of cases studied here, largest deviations from the average value were found for the two winter events.

The total rain sum produced by a track was derived by integrating the AIRR over the whole life span of the track. The so determined ATIRS shows a quadratic increase with the life span for each track type (Equation 6.30).

### **Analytical equations for the mean characteristics**

The structural characteristics of the precipitation field can be described by a set of simple equations and distributions involving only a small number of parameters, for example eight parameters are needed to describe the cluster size distribution and three parameters for the distances between peaks (THEUSNER 2007). Together with the diurnal variations described by the first few frequencies of the fast Fourier transformation, this sums up to a number of approximately 20 parameters. Selected distributions were recalculated in this thesis with the higher resolution RZ composite and it was shown that the results of the geometrical structure are reproducible with this new data. The analysis was then extended by a Lagrangian-type analysis aiming at an analytical description of the temporal development of the individual clusters within the precipitation field. Following an organisation scheme which classifies the tracks (equivalent to the life cycle of a cluster) by track type and life span, simple

## Chapter 7. Summary and conclusions

---

functions for the mean time series of the area integrated rain rate (AIRR) as well as the area size for those classes were derived. The mean temporal development of the area  $\bar{a}_{k,l}(t)$  can be described by a sinus, while the AIRR time series  $\bar{r}_{k,l}(t)$  follows a parabolic shape:

$$\bar{a}_{k,l}(t) = (\alpha_{1,k} + \alpha_{2,k} \cdot l + \alpha_{3,k} \cdot l^2) \cdot \sin\left(\pi \cdot \frac{t}{l}\right)^{d_k}$$

$$\bar{r}_{k,l}(t) = 4 \cdot \beta_k \cdot l \cdot \left( \frac{t}{l} - \frac{t^2}{l^2} \right)$$

Both equations have the life span  $l$  as the only free variable, the time  $t$  runs from 0 to life span  $l$ . The only information given on the unknown life span of the tracks is the frequency distribution for each track type as well as for the whole set of tracks. The life span frequency distribution is for single-cell-tracks given by a power law:

$$N(l) = a \cdot l^b,$$

and for single-cluster-tracks and multi-cluster-tracks by a modified power law:

$$N(l) = c_2 \cdot l^{d_2} \cdot \left( 1 - c_3 \cdot l^{d_3} - \frac{c_4}{l} \right)$$

The total rain sum a track produces in the course of its life also depends only on the track type and within each track type on the life span in a simple quadratic form:

$$\bar{R}_{k,l} = \frac{2}{3} \cdot \beta_k \cdot l^2$$

Finally, the problem of an analytical description for the temporal development of the AIRR and the area has been reduced to the life span as the only free variable, which is primarily unknown. Nevertheless, frequency distributions for all three track types can be provided as well as for the whole set of tracks. All those distributions can basically be described by power laws. For the analyses presented here, two approaches were followed. In an Eulerian-type approach the instantaneous radar derived rain rates at each time step were analysed concerning their geometrical structure and rain amounts. The Lagrangian-type approach concentrated on the individual structures within the precipitation field and their temporal development. Still open questions are: how do the results of both types of analysis (Eulerian, Lagrangian) fit together and how does a combination give the possibility to learn more about the underlying processes? Are the results in line with each other? For a detailed answer to these questions it would be helpful to simulate the precipitation

## Chapter 7. Summary and conclusions

---

field by means of the equations presented here and in previous studies. Only a short discussion is given here with respect to the growth process. The power laws identified for the cell number distribution (Eulerian-type approach) and the life span yielded the assumption of a underlying Yule process. The investigations on the growth processes (Langrangian-type approach) revealed indeed an incremental growth for the clusters with respect to the cell number (*number growth*), which is the key process of such a Yule process. Clusters were found to form as single cells and gain preferably one additional cell within each time step. The probability with which this growth occurs is different for different cell numbers.

In response to objectives 1 and 2, it is hypothesised that the results presented in this thesis, including an Eulerian- and an Lagrangian-type analysis of the post-frontal precipitation field, provide in combination with the results of THEUSNER (2007) a thorough description of the post-frontal convective precipitation field. Only a small number of parameters is sufficient to describe the precipitation structure and its temporal development. This includes approximately 20 parameters for the geometrical structure and the diurnal cycles and another 25 for the temporal development of the individual clusters. The latter are composed of four parameters for the area development of each track type (see Table 6.3 and 6.4), one parameter for the rain rate development of each track type (see Table 6.5) and altogether ten parameters for the life span distributions for the different track types (see Table 3.2 and 3.3).

The main results of this study can finally be summarised as follows: Enabled (1) by the assumption that post-frontal showers are generated by a stochastic process and (2) by the restriction to one synoptic situation, the average characteristics and their temporal development can be described by simple analytical equations. The only free variable in those equations is the life span  $l$ . This way, the problem is reduced to only one free parameter, for which only the frequency distribution is known.

# Chapter 8

## Limitations and Outlook

### Constraints and Limitations

The present study is limited by the rarely known quality of the radar derived precipitation amounts. A basic evaluation of the daily totals revealed a significant overestimation of rain sums derived by radar compared to ground based measurements. This observation is well in line with an evaluation presented by PAULAT (2007) for the period from 2001 to 2004, where the radar reflectivities of the PC composite were converted into rain rates by means of the standard Z-R-relationship. Although the data basis of the present study is too small for a meaningful evaluation, the preliminary results reveal rarely an improvement through the advanced Z-R-relationship. However, future advancements in rain rate determination can easily be adapted to the results presented here.

The evaluation of the precipitation rates are not only limited by the quality of the radar derived rain rates but also by remaining clutter and attenuation effects, which may have significant impact on the radar derived rain amounts. The uncertainty concerning the absolute rain rates might not be that crucial as, especially for the time series, no point data is used but areal sums instead. The determination of statistical means additionally compensates the uncertainties. The determined rain sums and their development can be seen as a hint on the probable mean development of a cluster. The effective precipitation rates may significantly deviate from that mean.

Aside from those radar related limitations, the analysis reveals several other types of constraints. Remaining questions concern for example seasonal and orographic dependencies. The latter was partly investigated in previous studies with respect to the geometric structure, revealing an enhanced convective activity at the North Sea coast. However, more research is necessary to evaluate the influence of orography

## Chapter 8. Limitations and Outlook

---

on the shower characteristics. Especially with a focus on the land-sea differences, it would be interesting to investigate the change in the structure which is observed at the coast. While over the ocean, open and closed cells prevail, convection is often enhanced when it is advected onto land leading to a significant change in the structure.

For a determination of seasonal dependencies, the data set analysed in the present study is too small. Although the analysis was not restricted to a specific season, most of the considered days are spring or summer days. Nevertheless, the life span distributions for all tracks on the individual days show the largest deviations from the mean for the only two winter days. Whether this is caused by random effects or if the characteristics actually show seasonal dependencies could not be evaluated with the present data set.

Finally, the influence of the total precipitation coverage on the clusters' growth process could not be investigated due to the procedure of determining the area of interest. The post-frontal shower field was selected by a semi-automatic algorithm in which a polygon was drawn manually around the precipitation field, which is to a certain degree a subjective procedure. A measure for the precipitation coverage cannot be reasonably determined with respect to the area of interest. Better results may be derived by determining the minimum area which encloses all clusters selected in the primary selection process. However, this is not presented in this thesis.

Related to the subject of precipitation coverage is the question whether locations exist where new shower cells preferably grow. The Yule process implies preferred growth in the vicinity of existing cells. This has not been investigated so far and may be additionally influenced by the precipitation coverage.

## Outlook

Despite the restriction to one specific synoptic situation, the results may be beneficial for hydrological modelling. The characteristics of the ensemble of showers provide a huge set of information which can be used for a stochastic modelling of the post-frontal shower field. As the individual clusters have a spatial and temporal scale which lie below the resolution of operational deterministic weather forecast models, a shower forecast scheme may also be constructed as an application which might be switched on when a cold front passage is forecast. The development of such a forecast scheme for post-frontal shower precipitation has been the objective of the shower project (see Chapter 1). The planned scheme will combine a deterministic forecast of the post-frontal precipitation field location with a probabilistic forecast of the individual rain areas contained therein. To determine precipitation probabilities, the distribution functions derived for the cell number, area size and other quantities shall be used in combination with the analytical functions revealed for the precipitation rate and area development. The output of the scheme will consist of statistical means of the various quantities like for example the number of convective rain areas and the areal precipitation. The realisation of the forecast scheme is subject of



## Chapter 8. Limitations and Outlook

---

ongoing research.

In the following, some aspects are listed which should be addressed in future studies in preparation of the envisaged forecast scheme.

The day-to-day variability which was observed both for the cell number distribution and the life span distribution was also found for the temporal development of the characteristics. The mean time series for individual days show the same structure, but different amplitudes. The influence of the synoptic parameters on the observed characteristics could not be quantified so far. Traditional convection parameter fail to describe the dependencies. Thus, new ways of characterising the observed differences between the individual days need to be evaluated.

Consecutive work should mainly focus on the consolidation of the pool of equations and distributions to provide a thorough description of the post-frontal precipitation structures. A simulation of the precipitation field with a high resolution numerical weather prediction model may provide additional information on the physical background of the observations.

The cut-off value of 0.05 mm per 5 min applied for the analyses was based on the results of THEUSNER (2007) who studied the influence of the cut-off on the geometrical characteristics. In addition to that, a sensitivity study regarding the influence of the cut-off on the temporal development should be performed. It is assumed that the shape of the time series stays the same, but the amplitude varies when different cut-off values are used.

Concerning the cluster orientation and motion, the investigations were only of qualitative nature. A quantitative comparison of tracks with the wind field, maybe with a subdivision of the total area into smaller sections, could provide additional information on the steering level. This might also be the wind in higher levels.

### Possible applications

This thesis provides new findings on the temporal development of individual clusters. These new insights enable an improved description of the temporal development of individual clusters. The observed time series may, for example, be imprinted on individual clusters within spatial precipitation fields, which are simulated based on the characteristics of the geometric structure. This would certainly give better representations of the spatial and temporal description of the precipitation field. Current spatial-temporal stochastic rainfall models like that proposed by NORTHROP (1998) use random values for cell counts within a storm and for their life span as input parameters. An implementation of observed distributions for these parameters may be beneficial for the model performance.

The results on the geometrical structure may be used for a verification of high resolution numerical model. The COSMO-DE with its 2.8 km resolution explicitly simulates mid-level and deep convection while shallow convection is still parametrised.

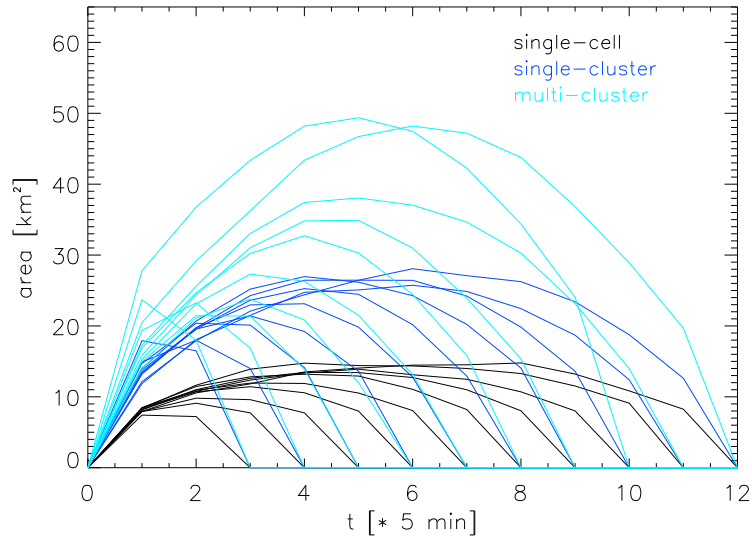


**Figure 8.1:** Mean area time series for all three track types.

The model performance regarding post-frontal shower precipitation can be tested by means of the cluster size distribution and the cell number distribution, for example. This is currently done within the scope of a DFG project at the *Institute of Meteorology and Climatology of the Leibniz University of Hannover* (D. ETLING, pers. comm.).

Another possible application is given by the different development rates with respect to track type and life span (see for example the area development in Figure 8.1). If the initial development of a cluster is known, it is possible to estimate the life span and relating further development based on the analytical functions. This is an interesting feature for nowcasting purposes, but may also be employed in other fields of research. One actual example shall be mentioned here: the new data assimilation scheme developed within the SPP 1167 DAQUA project titled *Combined Data Assimilation with Radar and Satellite Retrievals and Ensemble Modelling for the Improvement of Short Range Quantitative Precipitation Forecasts* (H. ELBERN, pers. comm.). This scheme consists of an ensemble method called SIRF (Sequential Importance Resampling Filter) in combination with a 4D-Var data assimilation. Within the ensemble runs, cells are simulated with different intensities and at different locations. Those ensemble members that are not in line with the observations are deleted, while the well-performing members are multiplied. The statistics on the life span and on the development of individual clusters may contribute to the scheme by providing hints on the probable future development based on observed initial development of the clusters. This way, the ensemble runs may be extended by a few hours and the statistics can be used as an additional performance indicator.

# Appendix A

## Track Examples

For each track type, three examples with different life spans are given revealing the range of possible developments. Displayed are (a) the time series of precipitation area (red line) and AIRR (black line) and (b) the total sum per fixed pixel (= footprint).

## A.1 Single-cell-tracks

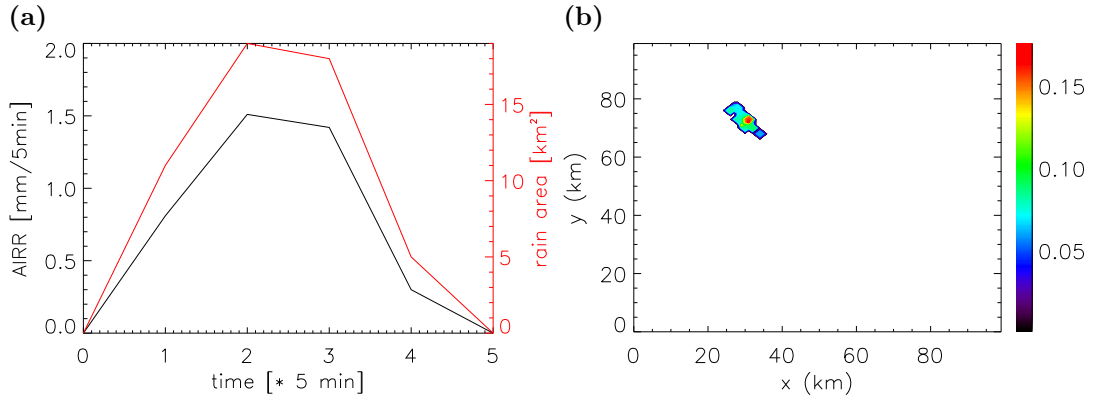


Figure A.1: Example of a single-cell-track with life span  $l = 25$  min.

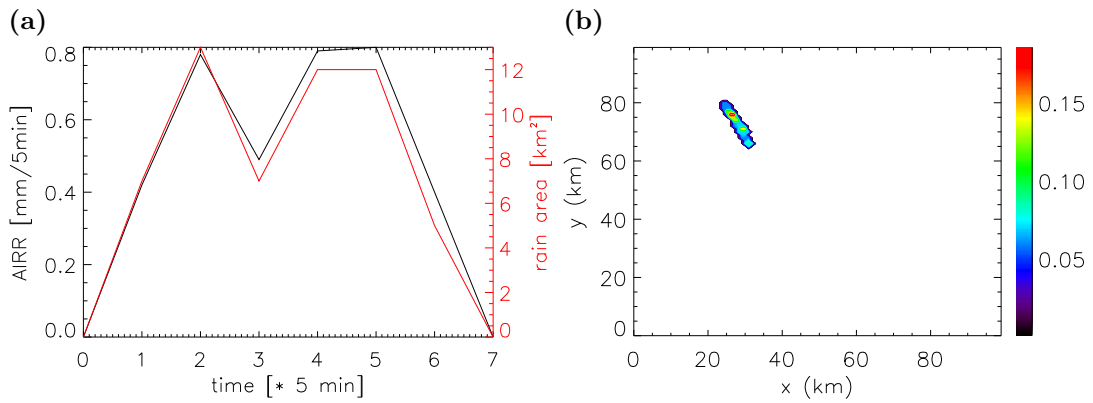


Figure A.2: Example of a single-cell-track with life span  $l = 35$  min.

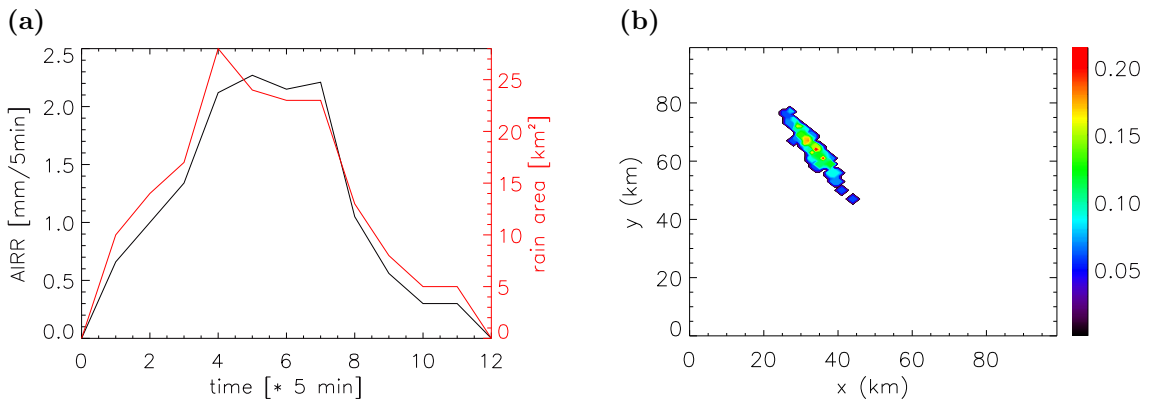
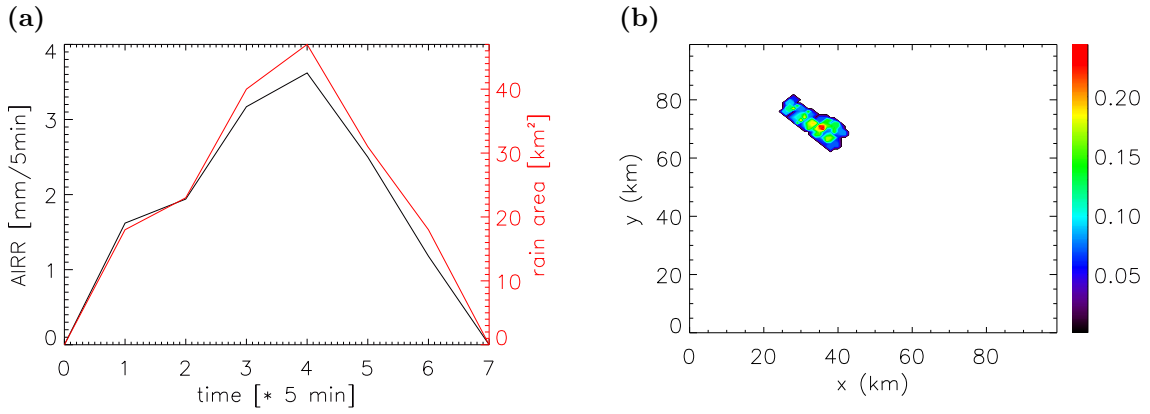
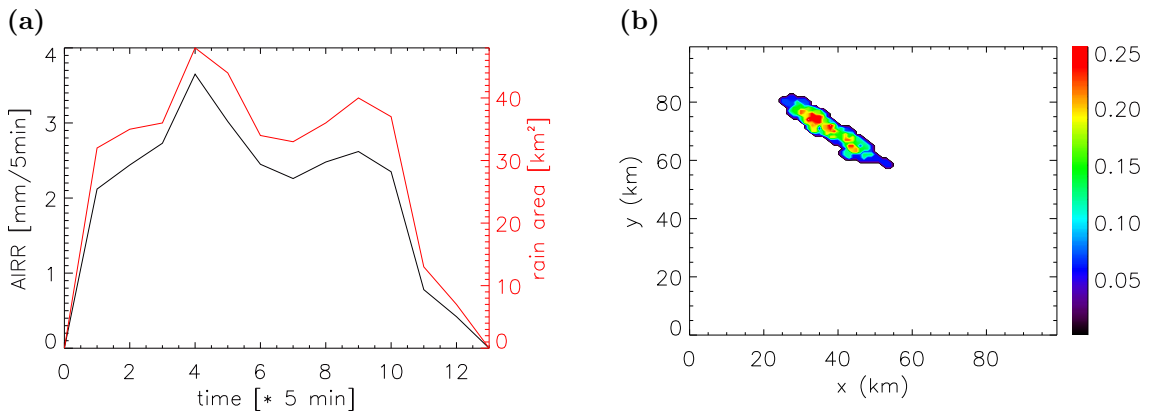


Figure A.3: Example of a single-cell-track with life span  $l = 60$  min.

## A.2 Single-cluster-tracks



**Figure A.4:** Example of a single-cluster-track with life span  $l = 35$  min.



**Figure A.5:** Example of a single-cluster-track with life span  $l = 60$  min.

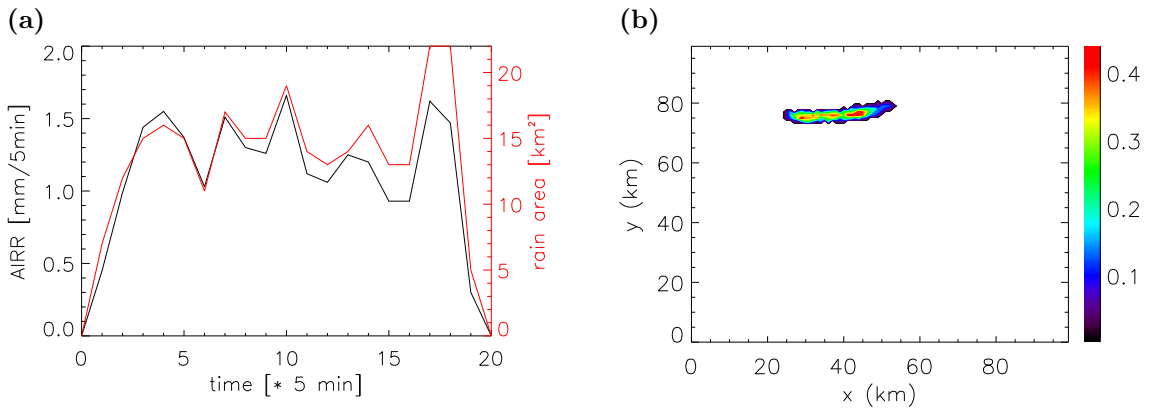


**Figure A.6:** Example of a single-cluster-track with life span  $l = 100$  min.

### A.3 Multi-cluster-tracks

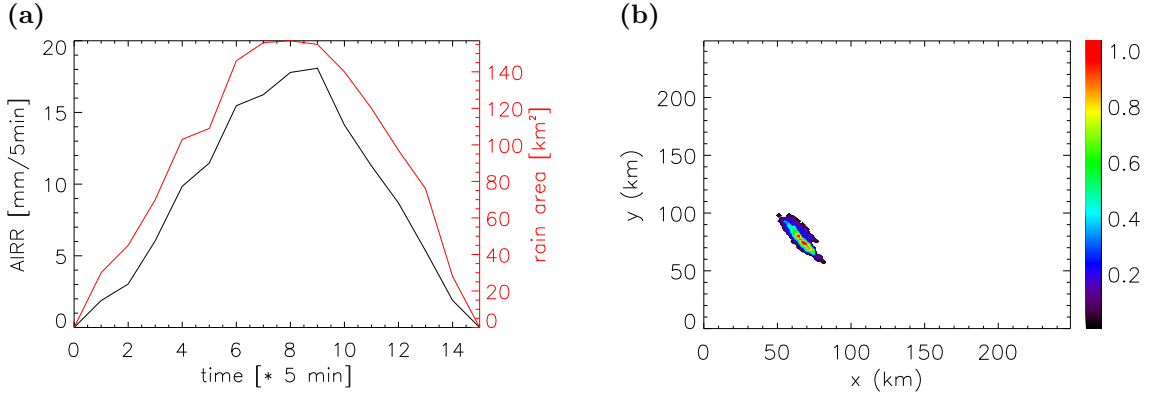


Figure A.7: Example of a multi-cluster-track with life span  $l = 70$  min.

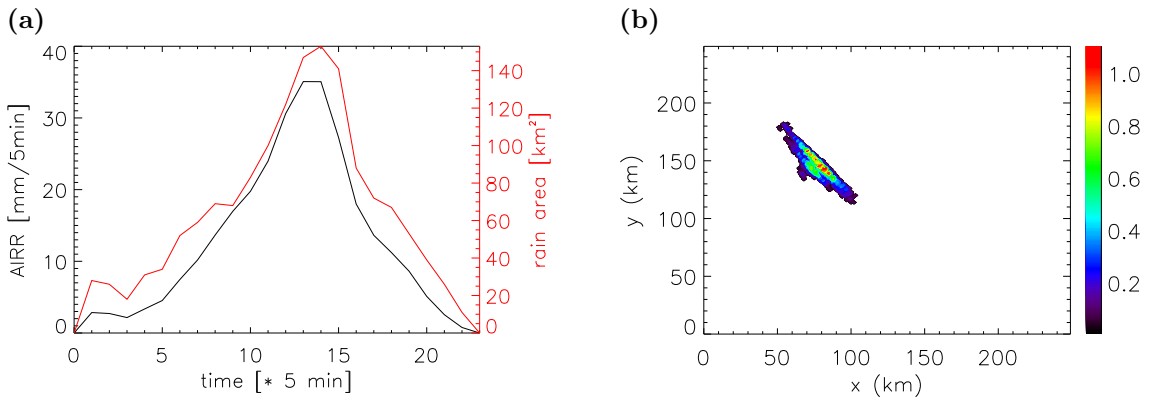


Figure A.8: Example of a multi-cluster-track with life span  $l = 115$  min.

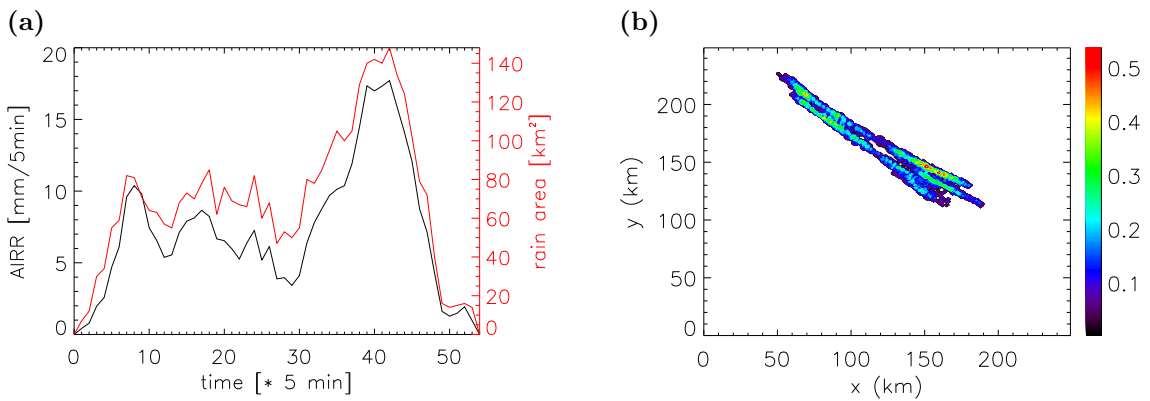
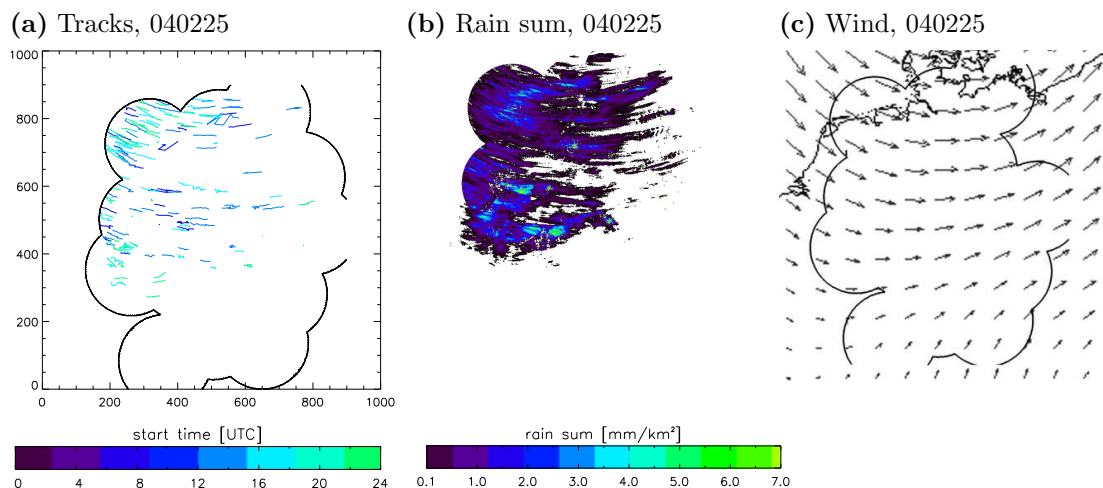


Figure A.9: Example of a multi-cluster-track with life span  $l = 265$  min.

# Appendix B

## Movement of the precipitation field

Tracks with a life span of 50 - 100 min are presented in comparison with daily precipitation sums and the 925 hPa wind field (NCEP reanalysis data). The tracks basically move with the mean wind, observed deviations are mainly to the right of the wind flow, e.g. on 21 March 2004. The different colors of the tracks represent different start times. The wind fields on the other hand display the situation at a specific time (12 UTC). Thus, a large part of the deviations is caused by the time differences. The comparison can only be seen as a qualitative attempt to relate the tracks' movement to the wind field.



**Figure B.1:** Comparison of tracks (for  $l = 50 - 100$  min), daily rain sums and 925 hPa wind field (12 UTC) for 25 February 2004.

## Appendix B: Movement of the precipitation field

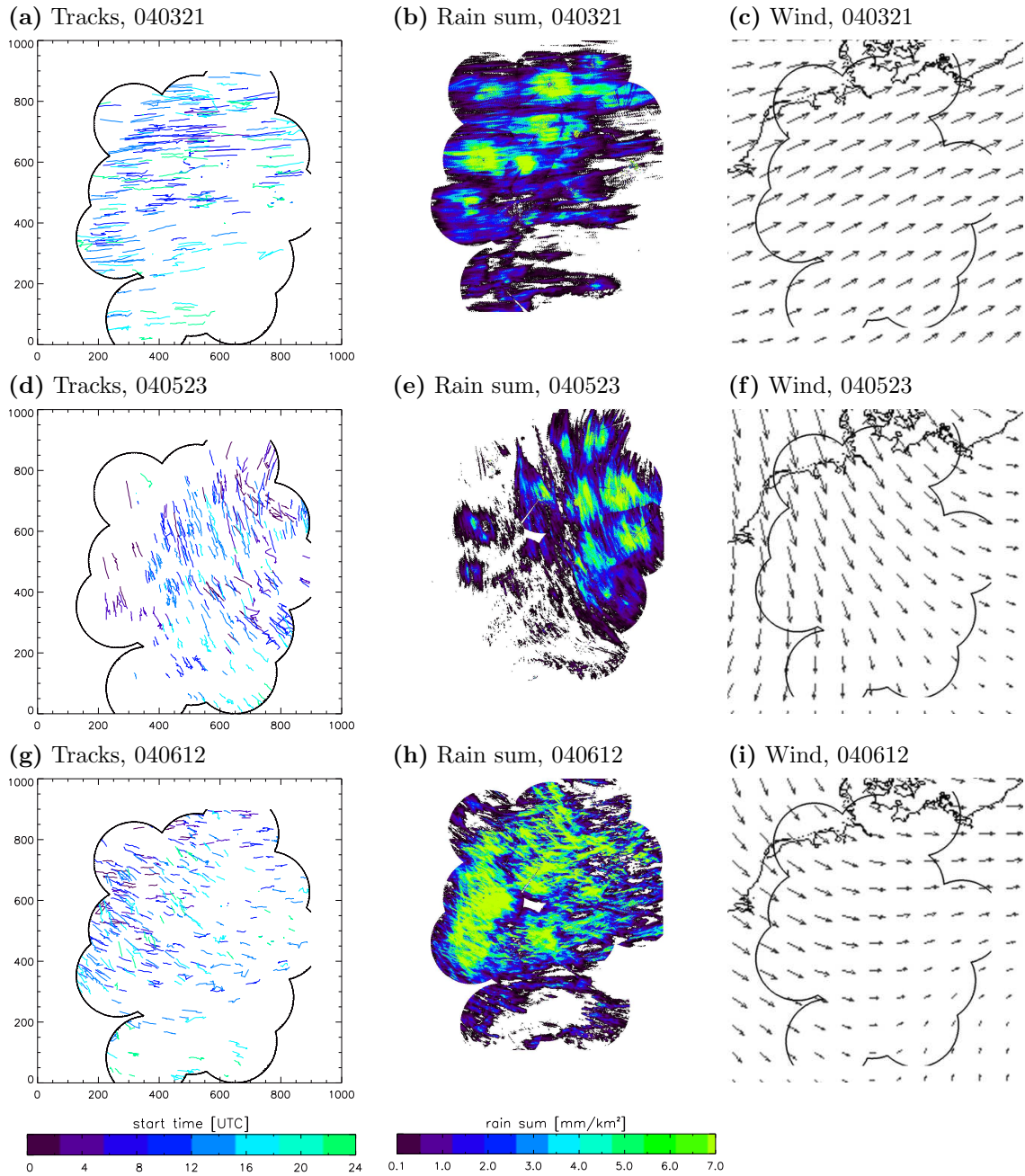


**Figure B.2:** Comparison of tracks (for  $l = 50 - 100$  min), daily rain sums and 925 hPa wind field (12 UTC) for 21 March, 23 May and 12 June 2004.



## Appendix B: Movement of the precipitation field

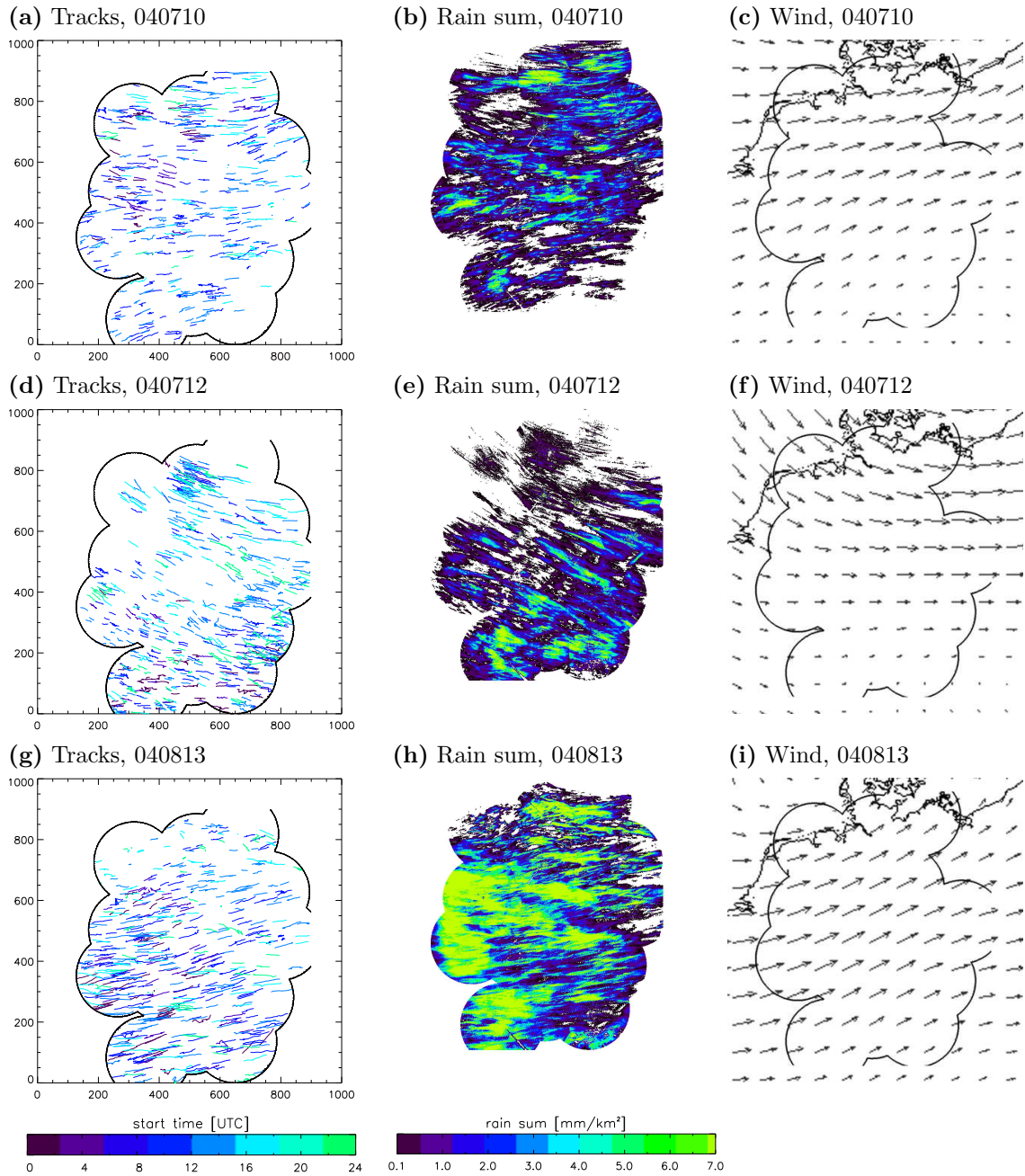


**Figure B.3:** Comparison of tracks (for  $l = 50 - 100$  min), daily rain sums and 925 hPa wind field (12 UTC) for 10 and 12 July and 13 August 2004.

## Appendix B: Movement of the precipitation field

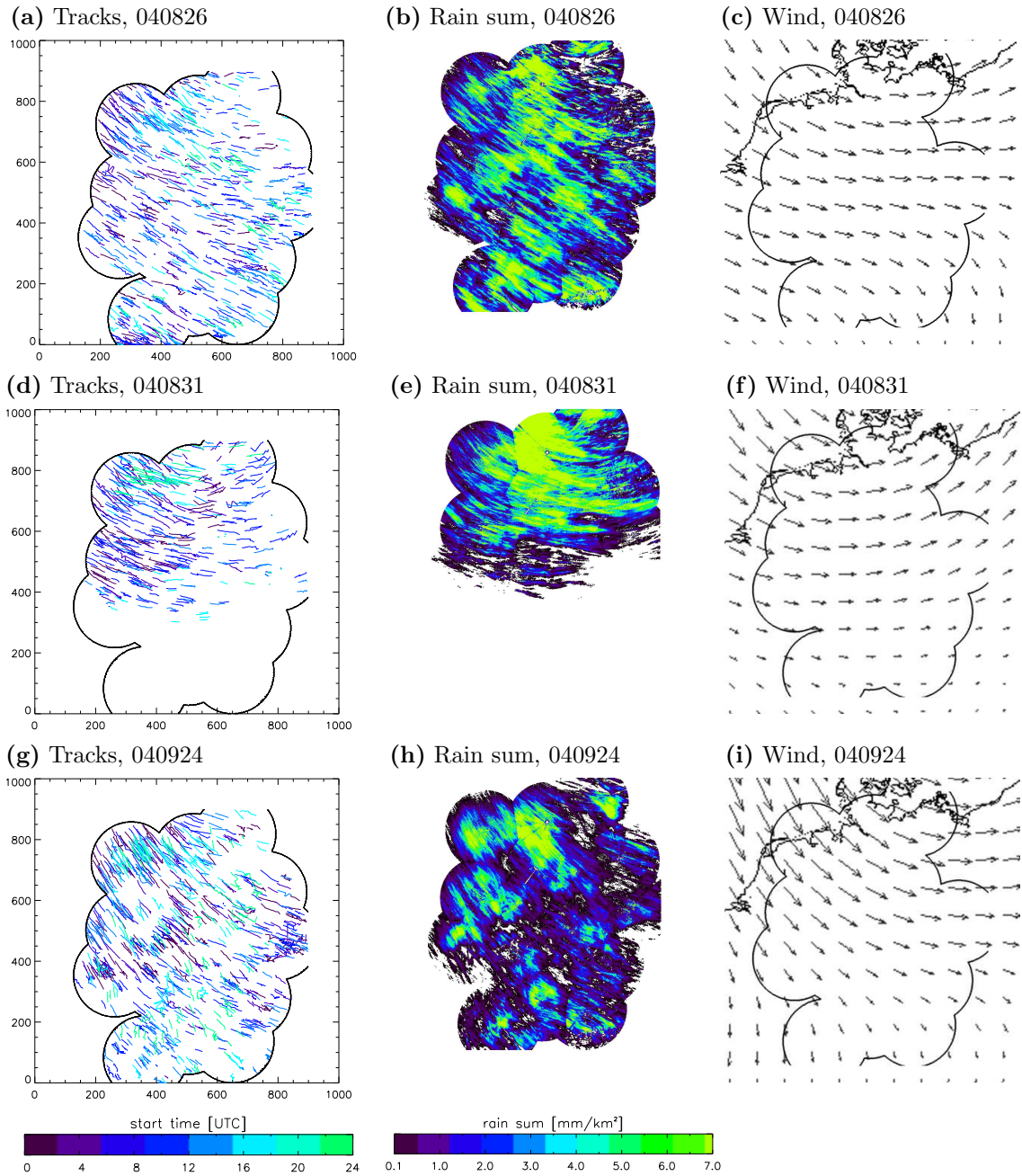


**Figure B.4:** Comparison of tracks (for  $l = 50 - 100$  min), daily rain sums and 925 hPa wind field (12 UTC) for 26 and 31 August and 24 September 2004.

## Appendix B: Movement of the precipitation field

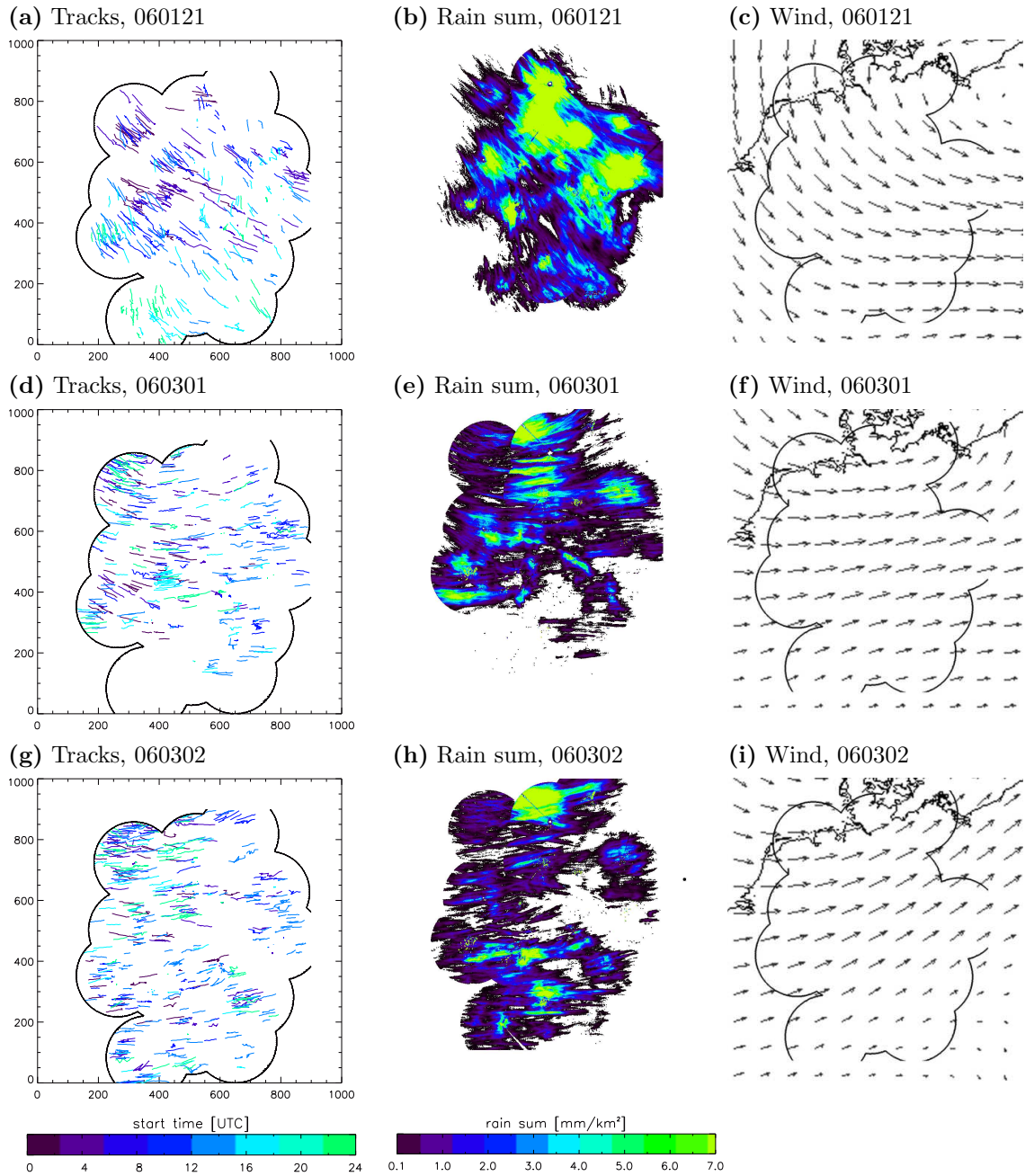


**Figure B.5:** Comparison of tracks (for  $l = 50 - 100$  min), daily rain sums and 925 hPa wind field (12 UTC) for 21 January and 1 and 2 March 2006.

## Appendix B: Movement of the precipitation field

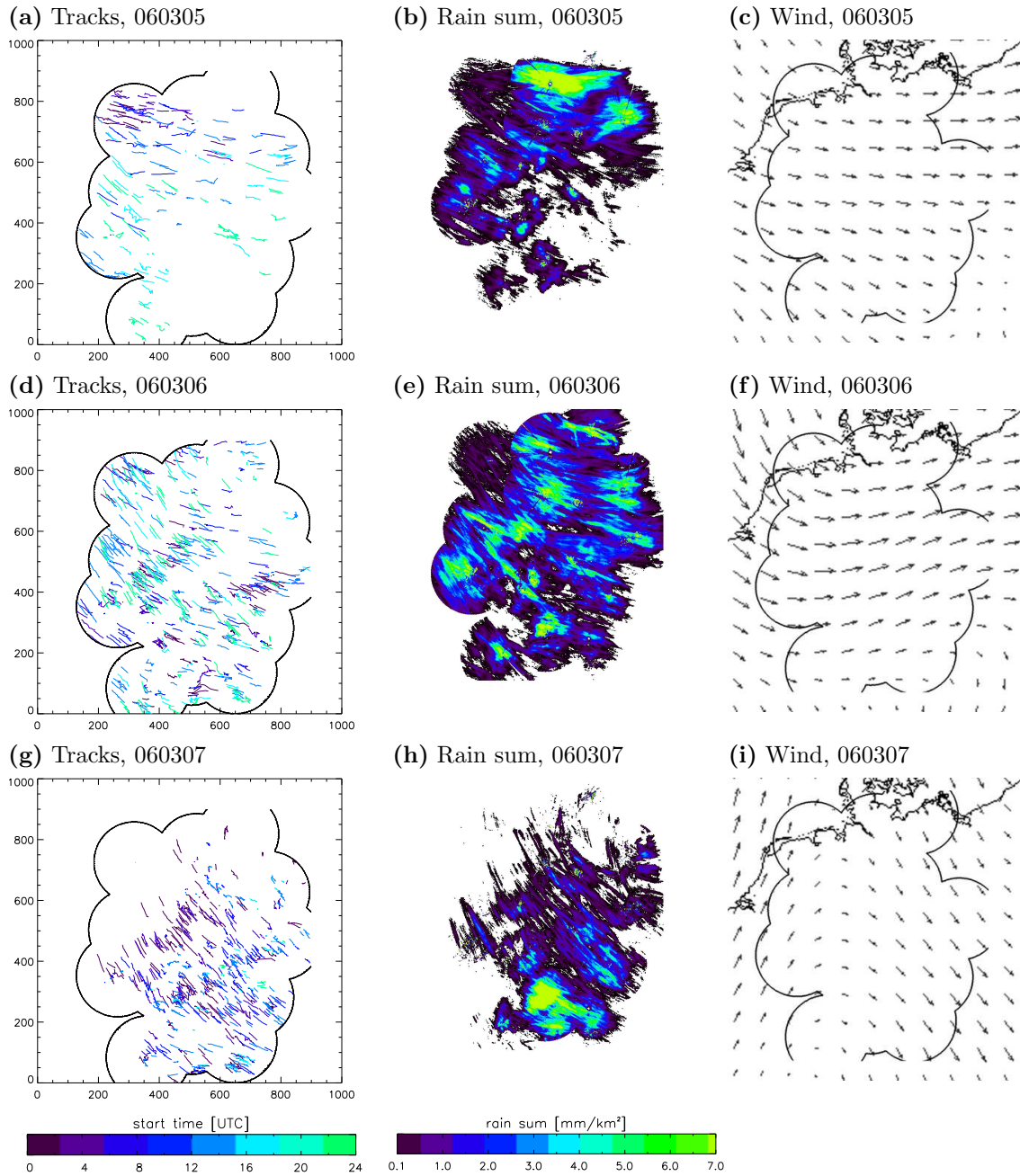


**Figure B.6:** Comparison of tracks (for  $l = 50 - 100$  min), daily rain sums and 925 hPa wind field (12 UTC) for 5, 6 and 7 March 2006.

## Appendix B: Movement of the precipitation field

---

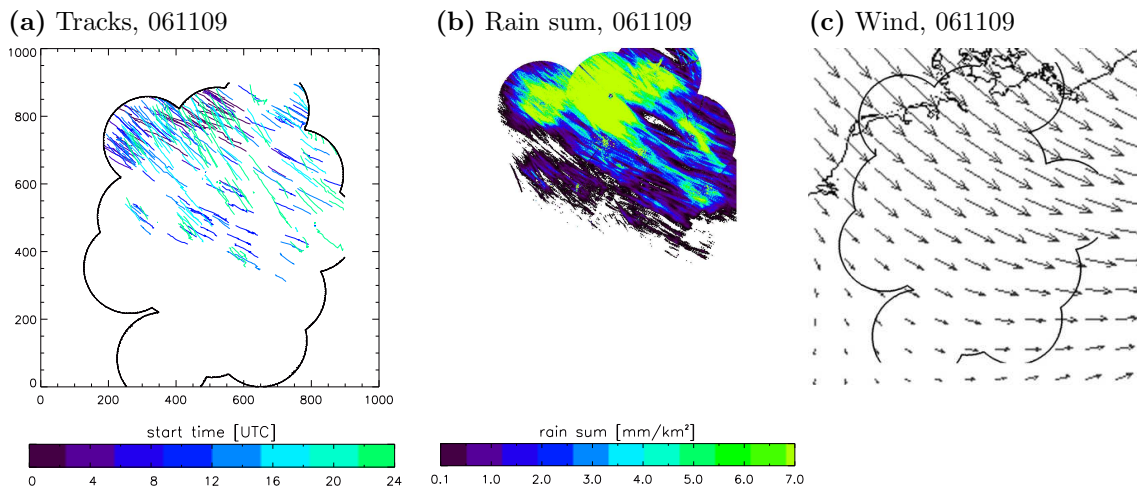


**Figure B.7:** Comparison of tracks (for  $l = 50 - 100$  min), daily rain sums and 925 hPa wind field (12 UTC) for 9 November 2006.

# Appendix C

## Statistical measures

In the following, basic statistical measures employed in the present work are introduced.

### Least squares

The fits for the various functions were derived by the least squares method, i.e. the parameters of the fitting function were adjusted in such a way that the sum of squared residuals is a minimum. A residual is defined as the difference between the values of the dependent variable  $y_n$  and the model  $y(x_n)$ .

$$MIN \sum_{n=1}^N (y_n - y(x_n))^2 \quad (C.1)$$

### Mean and standard deviation

The standard deviation  $\sigma_y$  is a statistical measure for the dispersion of a variable  $y$  around its mean value  $\mu_y$ . The mean value and the standard deviation are based on the assumption that the sample is normally distributed.

$$\sigma_y = \sqrt{\frac{1}{n} \cdot \sum_{i=1}^n (y_i - \mu_y)^2} \quad (C.2)$$

$$\mu_y = \frac{1}{n} \sum_{i=1}^n y_i \quad (C.3)$$

## Appendix C: Statistical measures

---

### Coefficient of variation

The coefficient of variation  $c_v$  is a normalized measure of dispersion of a probability distribution. It is defined as the ratio of the standard deviation  $\sigma_y$  to the mean  $\mu_y$

$$c_v = \frac{\sigma_y}{\mu_y} \quad (\text{C.4})$$

### Coefficient of determination

The coefficient of determination  $R^2$  is a statistic measure for the proportion of variability in a data set. In the case of a linear regression, it is defined as the square of the sample correlation coefficient  $\mathcal{R}$ .

$$Kor(X, Y) = \frac{Cov(X, Y)}{\sigma_x \cdot \sigma_y} \quad (\text{C.5})$$

$$= \frac{\frac{1}{n} \cdot \sum_{i=1}^n (x_i - \bar{x}) \cdot (y_i - \bar{y})}{\sqrt{\frac{1}{n} \cdot \sum_{i=1}^n (x_i - \bar{x})^2} \cdot \sqrt{\frac{1}{n} \cdot \sum_{i=1}^n (y_i - \bar{y})^2}} \quad (\text{C.6})$$

$$= r_{x,y} \quad (\text{C.7})$$

$$= \mathcal{R} \quad (\text{C.8})$$

$$R^2 = r_{x,y}^2 \quad (\text{C.9})$$

with

$\sigma_x$  standard deviation of  $x$

$\sigma_y$  standard deviation of  $y$

$Cov(X, Y)$  covariance between random variables  $X$  and  $Y$

$Kor(X, Y)$  correlation coefficient between random variables  $X$  and  $Y$

# Appendix D

## Parameters of the fitting functions for different life spans

The mean time series of the area integrated rain rate (AIRR) and the area were fitted both to a parabola and a sinus function (Section 6.1.2). The respective parameters of the non-normalised functions (see Section 6.1.3) as well as the standard deviations and the coefficients of determination are listed in the following tables. The parameters of the sinus were thereby determined assuming the exponent  $d_k$  being dependent on the life span to evaluate the correctness of the assumption of a constant exponent, which was made in Section 6.1.3.



---

**Appendix D: Parameters of the fitting functions for different life spans**

---

**AIRR, single-cell-tracks ( $k=1$ )**

$l$	$N(l)$	$A_{max}$	parabola				sinus			
			$g_k$	$h_k$	$\sigma$	$R^2$	$c_k$	$d_k$	$\sigma$	$R^2$
3	28 775	1.01	1.125	2.999	0.007	1.000	1.195	1.240	0.007	1.000
4	11 285	1.31	1.393	4.002	0.053	0.992	1.310	0.504	0.013	1.000
5	5 447	1.50	1.610	4.994	0.095	0.979	1.502	0.503	0.045	0.995
6	2 916	1.79	1.863	5.981	0.092	0.985	1.781	0.633	0.061	0.993
7	1 742	2.21	2.228	6.947	0.139	0.975	2.137	0.664	0.118	0.979
8	1 051	2.48	2.581	7.951	0.168	0.971	2.464	0.643	0.131	0.980
9	651	2.86	2.855	8.994	0.219	0.957	2.697	0.586	0.146	0.977
10	418	3.07	3.114	9.938	0.214	0.967	2.971	0.643	0.161	0.976
11	284	3.55	3.583	10.984	0.470	0.866	3.248	0.423	0.297	0.933
12	194	3.77	3.419	11.849	0.498	0.839	3.115	0.468	0.393	0.875
13	138	3.41	3.540	12.984	0.341	0.928	3.304	0.544	0.221	0.960
14	122	3.81	3.922	13.875	0.542	0.851	3.556	0.442	0.370	0.905
15	76	4.84	4.824	14.886	0.575	0.887	4.459	0.518	0.419	0.920

**Table D.1:** Parameters of the parabola and of the sinus fitted to AIRR time series data for the various life spans, single-cell-tracks.

**AIRR, single-cluster-tracks ( $k=2$ )**

$l$	$N(l)$	$A_{max}$	parabola				sinus			
			$g_k$	$h_k$	$\sigma$	$R^2$	$c_k$	$d_{aa}$	$\sigma$	$R^2$
3	2 498	2.61	2.753	2.986	0.114	0.992	2.797	0.936	0.117	0.991
4	1 926	2.15	2.288	4.007	0.086	0.992	2.150	0.497	0.006	1.000
5	1 466	2.55	2.662	4.994	0.059	0.997	2.603	0.726	0.037	0.999
6	1 096	2.64	2.695	6.019	0.084	0.994	2.614	0.686	0.037	0.999
7	794	3.03	3.089	6.951	0.078	0.996	3.084	0.847	0.087	0.994
8	615	3.67	3.666	7.912	0.152	0.989	3.623	0.810	0.161	0.985
9	478	4.45	4.332	8.959	0.210	0.983	4.262	0.775	0.193	0.984
10	385	4.66	4.654	9.914	0.232	0.982	4.560	0.767	0.222	0.981
11	307	4.15	4.223	10.936	0.179	0.987	4.154	0.779	0.166	0.987
12	224	4.93	4.868	11.893	0.236	0.982	4.831	0.827	0.242	0.979
13	195	4.69	4.995	12.837	0.338	0.966	4.834	0.723	0.324	0.962
14	165	4.88	4.900	13.736	0.408	0.947	4.756	0.752	0.421	0.934
15	129	5.29	5.437	15.161	0.397	0.952	5.215	0.635	0.297	0.970

**Table D.2:** Parameters of the parabola and of the sinus fitted to AIRR time series data for the various life spans, single-cluster-tracks.

---

---

**Appendix D: Parameters of the fitting functions for different life spans**

---

**AIRR, multi-cluster-tracks ( $k=3$ )**

$l$	$N(l)$	$A_{max}$	parabola				sinus			
			$g_k$	$h_k$	$\sigma$	$R^2$	$c_k$	$d_k$	$\sigma$	$R^2$
3	969	4.83	5.213	2.991	0.138	0.997	4.868	0.348	0.141	0.996
4	1 409	4.31	4.536	3.986	0.190	0.990	4.310	0.564	0.136	0.995
5	1 420	3.06	3.130	4.985	0.038	0.999	3.150	0.874	0.039	0.999
6	1 342	3.41	3.343	5.959	0.074	0.997	3.380	0.907	0.077	0.996
7	1 186	4.19	4.170	6.943	0.200	0.985	4.069	0.742	0.188	0.985
8	1 022	4.82	4.864	7.977	0.261	0.981	4.666	0.656	0.174	0.990
9	869	5.19	5.196	8.942	0.175	0.992	5.154	0.817	0.172	0.991
10	868	8.73	9.435	10.121	1.080	0.896	8.511	0.379	0.351	0.986
11	672	5.36	5.519	10.877	0.282	0.983	5.376	0.748	0.270	0.979
12	613	7.03	7.067	12.005	0.261	0.990	6.897	0.730	0.156	0.996
13	563	8.22	7.771	12.956	0.489	0.968	7.575	0.733	0.426	0.972
14	547	7.72	7.772	13.926	0.209	0.994	7.778	0.858	0.214	0.993
15	448	9.44	9.713	14.870	1.040	0.913	9.009	0.534	0.732	0.938

**Table D.3:** Parameters of the parabola and of the sinus fitted to AIRR time series data for the various life spans, multi-cluster-tracks.

**area, single-cell-tracks ( $k=1$ )**

$l$	$N(l)$	$A_{max}$	parabola				sinus			
			$g_k$	$h_k$	$\sigma$	$R^2$	$c_k$	$d_k$	$\sigma$	$R^2$
3	28 775	6.94	7.680	2.996	0.079	0.999	8.786	1.756	0.081	0.999
4	11 285	8.59	9.166	4.005	0.360	0.991	8.590	0.483	0.054	1.000
5	5 447	9.18	10.102	5.023	0.585	0.979	9.365	0.462	0.052	1.000
6	2 916	11.00	11.694	6.036	0.676	0.977	10.945	0.520	0.075	1.000
7	1 742	11.47	12.505	7.056	0.949	0.959	11.546	0.469	0.169	0.999
8	1 051	12.76	13.772	8.087	0.989	0.961	12.824	0.501	0.137	0.999
9	651	13.00	14.049	9.127	1.061	0.955	13.066	0.494	0.075	1.000
10	418	13.53	14.269	10.177	1.236	0.938	13.168	0.459	0.157	0.999
11	284	14.29	15.661	11.270	1.559	0.914	14.347	0.420	0.352	0.995
12	194	14.24	15.326	12.352	1.356	0.929	14.199	0.459	0.400	0.993
13	138	14.53	15.672	13.411	1.603	0.904	14.350	0.410	0.244	0.997
14	122	14.76	16.108	14.483	1.687	0.897	14.741	0.404	0.280	0.996
15	76	16.25	17.111	15.687	2.000	0.863	15.738	0.408	1.129	0.950

**Table D.4:** Parameters of the parabola and of the sinus fitted to area time series data for the various life spans, single-cell-tracks.

---

---

**Appendix D: Parameters of the fitting functions for different life spans**

---

area, single-cluster-tracks ( $k=2$ )

$l$	$N(l)$	$A_{max}$	parabola				sinus			
			$g_k$	$h_k$	$\sigma$	$R^2$	$c_k$	$d_k$	$\sigma$	$R^2$
3	2 498	17.47	18.842	2.991	0.506	0.996	20.718	1.484	0.520	0.996
4	1 926	17.47	18.073	3.993	0.466	0.996	17.471	0.651	0.298	0.998
5	1 466	19.88	22.115	5.088	1.210	0.992	20.468	0.727	0.205	0.999
6	1 096	21.00	21.651	6.018	0.715	0.993	20.885	0.661	0.141	1.000
7	794	22.71	23.635	7.021	0.586	0.996	23.073	0.720	0.119	1.000
8	615	24.71	25.471	8.047	0.874	0.991	24.709	0.687	0.299	0.999
9	478	26.47	20.190	8.864	5.539	0.982	26.379	0.622	0.298	0.999
10	385	26.06	27.789	10.181	1.468	0.977	26.665	0.606	0.245	0.999
11	307	25.24	26.140	10.985	1.705	0.976	25.472	0.601	0.423	0.998
12	224	27.59	28.445	12.233	1.555	0.974	27.168	0.600	0.554	0.996
13	195	26.71	29.113	13.343	2.248	0.945	27.386	0.526	1.026	0.987
14	165	29.82	34.522	14.094	2.044	0.967	29.944	0.601	0.843	0.993
15	129	29.18	29.067	15.214	3.144	0.934	28.994	0.502	1.441	0.976

**Table D.5:** Parameters of the parabola and of the sinus fitted to area time series data for the various life spans, single-cluster-tracks.

area, multi-cluster-tracks ( $k=3$ )

$l$	$N(l)$	$A_{max}$	parabola				sinus			
			$g_k$	$h_k$	$\sigma$	$R^2$	$c_k$	$d_k$	$\sigma$	$R^2$
3	969	23.24	22.925	2.970	2.004	0.964	21.115	0.266	2.059	0.961
4	1 409	22.71	23.165	3.979	0.806	0.993	22.706	0.732	0.800	0.993
5	1 420	21.06	21.800	5.017	0.399	0.998	21.878	0.844	0.327	0.999
6	1 342	23.24	23.075	5.965	0.468	0.997	23.275	0.892	0.506	0.997
7	1 186	26.94	27.045	6.955	0.717	0.996	26.824	0.814	0.743	0.995
8	1 022	32.12	32.294	8.015	0.879	0.995	31.615	0.738	0.407	0.999
9	869	34.35	33.092	8.734	2.461	0.988	34.389	0.787	0.408	0.999
10	868	48.71	45.859	9.742	6.091	0.968	48.248	0.562	1.063	0.996
11	672	37.53	35.567	10.841	2.979	0.990	37.719	0.720	1.197	0.992
12	613	47.82	48.362	12.143	1.923	0.987	47.207	0.691	0.769	0.998
13	563	50.94	51.136	12.947	2.677	0.980	49.634	0.716	2.079	0.984
14	547	52.88	52.337	13.956	1.074	0.997	51.988	0.818	0.903	0.997
15	448	59.29	61.714	15.020	4.436	0.961	58.504	0.604	2.457	0.983

**Table D.6:** Parameters of the parabola and of the sinus fitted to area time series data for the various life spans, multi-cluster-tracks.

---

# Appendix E

## Coefficients of variation for mean time series

The mean time series were determined in two steps as described in Section 6.1.1. In a first instance, the mean time series for each track type  $k$  and each life span  $l$  were calculated on each day  $m$ . In a second step, those mean time series for track type  $k$  and life span  $l$  of each day were averaged over all days. The frequency distribution of the respective coefficients of variation for the different track types and the two steps of averaging are displayed in Figure E.1 for the area and in Figure E.2 for the AIRR.

### E.1 Coefficients of variation for area

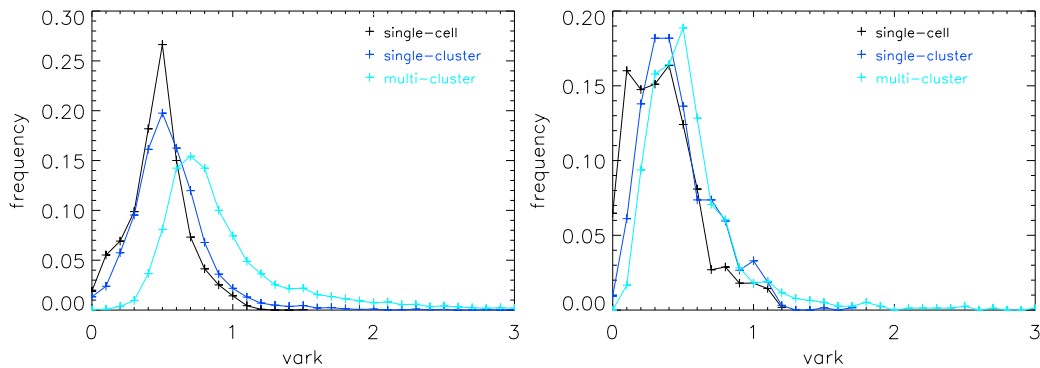


**Figure E.1:** Frequency distribution of the coefficients of variation for the area mean time series of (a) individual days (averaging step 1) and (b) for all days (averaging step 2) for all three track types.

## E.2 Coefficients of variation for AIRR

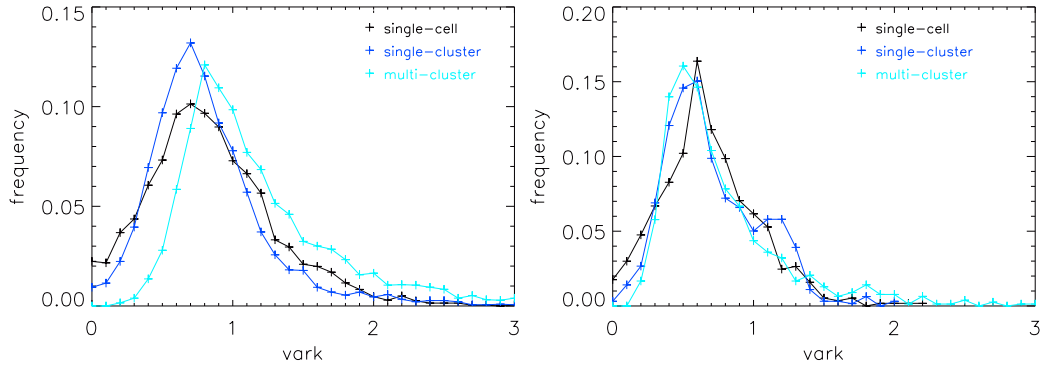


**Figure E.2:** Frequency distribution of the coefficients of variation for the AIRR mean time series of (a) individual days (averaging step 1) and (b) for all days (averaging step 2) for all three track types.

# Bibliography

- AUSTIN, P. M., 1987: *Relation between measured radar reflectivity and surface rainfall*, Mon. Weather Rev., **115**, 1053–1070
- AUSTIN, P. M. AND R. A. HOUZE, JR., 1972: *Analysis of the structure of precipitation patterns in New England*, J. Appl. Meteorol., **11**, 926–935
- BADER, M. J., G. S. FORBES, J. R. GRANT, R. B. E. LILLEY AND A. J. WATERS, 1995: *Images in Weather Forecasting*, University Press, Cambridge, 499 pp.
- BAK, P., C. TANG AND K. WIESENFELD, 1988: *Self-organized criticality*, Phy Rev A, **38**(1), 364–374
- BÁRDOSSY, A., 1998: *Generating precipitation time series using simulated annealing*, Water Resour. Res., **34**(7), 1737–1744
- BARTELS, H., E. WEIGL, T. REICH, P. LANG, A. WAGNER, O. KOHLER AND N. GERLACH, 2004: *Projekt RADOLAN - Routineverfahren zur Online-Aneicherung der Radarniederschlagsdaten mit Hilfe von automatischen Bodenniederschlagsstationen (Ombrometer)*, Abschlussbericht, Deutscher Wetterdienst, Offenbach, 111 S.
- BATTAN, L. J., 1973: *Radar Observation of the Atmosphere*, The University of Chicago Press, Chicago and London, 324 pp.
- BECHTOLD, P., J.-P. CHABOUREAU, A. BELJAARS, A. BETTS, M. KÖHLER, M. MILLER AND J.-L. REDELSPERGER, 2004: *The simulation of the diurnal cycle of convective precipitation over land in a global model*, Q. J. R. Meteorol. Soc., **130**, 3119–3137
- BEHENG, K. D., 1998: *Grundlagen der Wolkenmikrophysik und der Dynamik von Wolken und Fronten*, Annalen der Meteorologie, **38**, 7–24
- BLUESTEIN, H. B., 1992: *Synoptic-Dynamic Meteorology in Midlatitudes, Volume I*, Oxford University Press, New York, 431 pp.
- , 1993: *Synoptic-Dynamic Meteorology in Midlatitudes, Volume II*, Oxford University Press, New York, 594 pp.

## Bibliography

---

- BRAHAM JR., R. R., 1996: *The thunderstorm project*, Bull. Am. Meteorol. Soc., **77**(8), 1835–1845
- CHUMCHEAN, S., A. SHARMA AND A. SEED, 2003: *Radar rainfall error variance and its impact on radar rainfall calibration*, Phys. Chem. Earth, **28**, 27–39
- CLAUSEN, A. AND R. ROTH, 1997: *Regionalisierung von Niederschlag und Verdunstung zur besseren Parametrisierung des hydrologischen Zyklus in Klimamodellen*, Abschlussbericht zum BMBF-Projekt 07 VWK 01-6, Institut für Meteorologie und Klimatologie, Hannover, 20 S.
- CONCAS, G., M. MARCHESI, S. PINNA AND N. SERRA, 2006: *On the suitability of Yule process to stochastically model some properties of object-oriented systems*, Physica A., **370**(2), 817–831
- CRAIG, G. C. AND B. G. COHEN, 2006: *Fluctuations in an equilibrium convective ensemble. Part I: Theoretical formulation*, J. Atmos. Sci., **63**, 1996–2004
- EHRET, U., 2002: *Rainfall and Flood Nowcasting in Small Catchments using Weather Radar*, Dissertation, Universität Stuttgart, 203 pp.
- EMANUEL, K., 1997: *Overview of atmospheric convection*, R. K. Smith (editor), The Physics and Parameterization of Moist Convection, Kluwer Academic Publisher, 1–28
- EMANUEL, K. A., 1994: *Atmospheric Convection*, Oxford University Press, 580 pp.
- FERAL, L., F. MESNARD, H. SAUVAGEOT, L. CASTANET AND J. LEMORTON, 2000: *Rain cells shape and orientation distribution in South-West of France*, Phys. Chem. Earth (B), **25**(10-12), 1073–1078
- FU, D. AND X. GUO, 2006: *A cloud-resolving study on the role of cumulus merger in MCS with heavy precipitation*, Adv. Atmos. Sci., **23**(6), 857–868
- GEKAT, F., P. MEISCHNER, K. FRIEDRICH, M. HAGEN, J. KOISTINEN, D. B. MICHELSON AND A. HUUSKONEN, 2003: *The state of weather radar operations, networks and products*, P. Meischner (editor), Weather Radar: Principles and Advanced Applications, Springer Berlin, 1–51
- GERMANN, U. AND J. JOSS, 2003: *Operational measurement of precipitation in mountainous terrain*, P. Meischner (editor), Weather Radar: Principles and Advanced Applications, Springer Berlin, 52–77
- GJERTSEN, U., M. ŠÁLEK AND D. MICHELSON, 2004: *Gauge adjustment of radar-based precipitation estimates in Europe*, Proceedings of ERAD, 7–11

## Bibliography

---

- GRABOWSKI, W. W., P. BECHTOLD, A. CHENG, R. FORBES, C. HALLIWELL, M. KHAIROUTDINOV, S. LANG, T. NASUNO, J. PETCH, W.-K. TAO AND R. WONG, 2006: *Daytime convective development over land: A model intercomparison based on LBA observations*, Q. J. R. Meteorol. Soc., **132**, 317–344
- HABERLANDT, U., A.-D. EBNER VON ESCHENBACH, A. BELLI AND C. GATTKER, 2007: *Space-time representativity of precipitation for rainfall-runoff modelling: Experience from some case studies*, Proceedings of Symposium HS2004 at IUGG2007, Perugia, IAHS Publ. No. 313, 61–69
- HAESELER, S., 1995: *Niederschlagsstrukturen auf Trogrückseiten*, Diplomarbeit, Institut für Meteorologie und Klimatologie, Universität Hannover, 109 S.
- VON HARDENBERG, J., 2003: *The shape of convective rain cells*, Geophys. Res. Lett., **30**(24), 2280
- HAUF, T., C. DETTMER AND W. DEIERLING, 2001: *Parametrisierung der Statistik von konvektiven Niederschlagsfeldern durch inverse Modellierung*, Abschlussbericht zum BMBF-Projekt 01LA9853/0, Institut für Meteorologie und Klimatologie, Hannover, 59 S.
- HENSE, A., G. ADRIAN, C. SIMMER AND V. WULFMAYER, 2003: *Quantitative Niederschlagsvorhersage: Ein Anspruch der Gesellschaft an die Meteorologie*, Antrag auf Einrichtung eines Schwerpunktprogramms der Deutschen Forschungsgemeinschaft, 33 pp., in [www.meteo.uni-bonn.de/projekte/SPPMeteo/reports/SPPLeitAntrag\\_Deutsch.pdf](http://www.meteo.uni-bonn.de/projekte/SPPMeteo/reports/SPPLeitAntrag_Deutsch.pdf)
- HEUEL, E.-M., 2004: *Quantitative Niederschlagsbestimmung aus Radardaten*, Dissertation, Mathematisch-Naturwissenschaftliche Fakultät, Universität Bonn, 162 pp.
- HOUZE, JR., R. A., 2004: *Mesoscale convective systems*, Rev. Geophys., **42**(RG4003), 1–43
- ILLINGWORTH, A., 2003: *Improved precipitation rates and data quality by using polarimetric measurements*, P. Meischner (editor), Weather Radar: Principles and Advanced Applications, Springer Berlin, 130–166
- JEWETT, B. F. AND R. B. WILHELMSON, 2006: *The role of forcing in cell morphology and evolution within midlatitude squall lines*, Mon. Weather Rev., **134**, 3714–3734
- JOSS, J. AND A. WALDVOGEL, 1990: *Precipitation measurements and hydrology*, D. Atlas (editor), Radar in Meteorology, American Meteorological Society, 577–606
- KARKLINSKY, M. AND E. MORIN, 2006: *Spatial characteristics of radar-derived convective rain cells over southern Israel*, Meteorol. Z., **15**(5), 384–411



## Bibliography

---

- LEE, G. AND I. ZAWADZKI, 2004: *Errors in rain measurements by radar due to the variability of drop size distributions*, Sixth International Symposium on Hydrological Applications of Weather Radar, Melbourne, Australia
- LILJEQUIST, G. H. AND K. CEHAK, 1974: *Allgemeine Meteorologie*, Friedrich Vieweg & Sohn, Braunschweig, 396 pp.
- LIN, X., D. A. RANDALL AND L. D. FOWLER, 2000: *Diurnal variability of the hydrologic cycle and radiative fluxes: Comparisons between observations and a GCM*, *J. Climate*, **13**, 4159–4179
- LÓPEZ, R. E., 1977: *The lognormal distribution and cloud populations*, *Mon. Weather Rev.*, **105**, 865–872
- LÓPEZ, R. E., D. O. BLANCHARD, D. ROSENFELD, W. L. HISCOX AND M. J. CASEY, 1983: *Population characteristics, development processes and structure of radar echoes in South Florida.*, *Mon. Weather Rev.*, **112**, 56–75
- MARSHALL, J. AND W. PALMER, 1948: *The distribution of raindrops with size*, *J. Atmos. Sci.*, **5**(4), 165–166
- MARX, A., 2007: *Einsatz gekoppelter Modelle und Wetterradar zur Abschätzung von Niederschlagsintensitäten und zur Abflussvorhersage*, Dissertation, Institut für Wasserbau, Universität Stuttgart, 138 pp.
- MECKLENBURG, S., 2000: *Nowcasting precipitation in an Alpine region with a radar echo tracking algorithm*, Dissertation, Swiss Federal Institute of Technology, Zürich, 115 pp.
- MESNARD, F. AND H. SAUVAGEOT, 2003: *Structural characteristics of rain fields*, *J. Geophys. Res.*, **108**(D13), 4385, doi:10.1029/2002JD002808
- NORTHROP, P., 1998: *A clustered spatial-temporal model of rainfall.*, *Proc. R. Soc. Lond. A*, **454**, 1875–1888
- PAULAT, M., 2007: *Verifikation der Niederschlagsvorhersage für Deutschland von 2001-2004*, Dissertation, Institut für Physik der Atmosphäre, Universität Mainz, 149 pp.
- SÁLEK, M., J.-L. CHEZE, J. HANDWERKER, L. DELOBBE AND R. UIJLENHOET, 2004: *Radar techniques for identifying precipitation type and estimating quantity of precipitation*, technical report, Wageningen University and Researchcenter Publications [<http://library.wur.nl/oai>] (Netherlands)
- SALTIKOFF, E., U. GJERTSEN, D. MICHELSON, I. HOLLEMANN, J. SELTMANN, K. ODAKIVI, A. HUUSKONEN, H. HOHTI, J. KOISTINEN, H. POHJALA AND G. HAASE, 2004: *Radar data quality issues in Northern Europe*, *Proceeding of ERAD (2004)*, 212–215

## Bibliography

---

- SAUVAGEOT, H., 1992: Radar Meteorology, Artech House Inc., Boston, 366 pp.
- SCHREIBER, K.-J., 1998: Der Radarverbund - Informationen zum Wetterradar-Verbundsystem, Deutscher Wetterdienst, Offenbach am Main, 30 pp.
- SELTMANN, J., 1997: *Radarforschung im DWD - Vom Scan zum Produkt*, PROMET, **26**, 32–42
- SMITH, J. A., D. J. SEO, M. L. BAECK AND M. D. HUDLOW, 1996: *An inter-comparison study of NEXRAD precipitation estimates*, Water Resour. Res., **32**(7), 2035–2045
- TETZLAFF, G. AND N. HAGEMANN, 1986: *Bemerkungen zum Niederschlag in Hannover*, Meteorol. Rdsch., **39**, 1–12
- THEUSNER, M., 2007: An Investigation on Small Scale Precipitation Structures, Dissertation, Institut für Meteorologie und Klimatologie, Universität Hannover, 95 pp.
- THEUSNER, M. AND T. HAUF, 2004: *A study on the small scale precipitation structure over Germany using the radar network of the German Weather Service*, Meteorol. Z., **13**, 311–322
- WALTHER, A., 2007: Radar-based precipitation classification in the Baltic Sea area., Dissertation, Fachbereich Geowissenschaften, Freie Universität Berlin, 94 pp.
- WEUSTHOFF, T. AND T. HAUF, 2008a: *Basic characteristics of post-frontal shower precipitation rates*, submitted to Meteorol. Z.
- , 2008b: *The life cycle of convective-shower cells under post-frontal conditions*, Q. J. R. Meteorol. Soc., **134**(633), 841–857
- WEUSTHOFF, T., 2005: Beiträge zur Entwicklung eines stochastischen Niederschlagsmodells zur Simulation postfrontaler Schauer, Diplomarbeit, Institut für Meteorologie und Klimatologie, Universität Hannover, 93 pp.
- WHEATER, H., R. CHANDLER, C. ONOF, V. ISHAM, E. BELLONE, C. YANG, D. LEKKAS, G. LOURMAS AND M.-L. SEGOND, 2005: *Spatial-temporal rainfall modelling for flood risk estimation*, Stoch Environ Res Risk Assess, **19**, 403–416
- WHEATER, H., V. ISHAM, D. COX, R. CHANDLER, A. KAKOU, P. NORTHROP, L. OH, C. ONOF AND I. RODRIGUEZ-ITURBE, 2000: *Spatial-temporal rainfall fields: Modelling and statistical aspects*, Hydrol. Earth Syst. Sci., **4**(4), 581–601
- WILLEMS, P., 2001: *A spatial rainfall generator for small spatial scales*, J. Hydrol., **252**, 126–144

## Bibliography

---

- WILSON, J. W., E. E. EBERT, T. R. SAXEN, R. D. ROBERTS, C. K. MUELLER, M. SLEIGH, C. E. PIERCE AND A. SEED, 2004: *Sydney 2000 forecast demonstration project: Convective storm nowcasting*, *Wea. Forecasting*, **19**, 131–150
- WITHA, B., 2007: Untersuchungen zur Variabilität postfrontaler Schauer, Diplomarbeit, Institut für Meteorologie und Klimatologie, Universität Hannover, 99 pp.

# List of Figures

2.1	500 hPa chart, 9 November 2006 . . . . .	9
2.2	Analysis of surface chart, 9 November 2006 . . . . .	9
2.3	Radio sounding of Greifswald, 9 November 2006 . . . . .	10
2.4	Satellite image, 9 November 2006 . . . . .	10
2.5	Radar image, 9 November 2006 . . . . .	11
2.6	Cloud life stages . . . . .	12
2.7	Example of a cluster . . . . .	12
2.8	Life stages of a cluster . . . . .	13
2.9	Growth processes as a function of life span . . . . .	14
2.10	Growth model . . . . .	15
2.11	Radar network of the German Weather Service . . . . .	18
2.12	Advanced Z-R-relationship . . . . .	21
2.13	Radar error sources: clutter and shielding . . . . .	23
3.1	Example of <i>character</i> -file . . . . .	26
3.2	Ratio of daily sums from synoptical observations and radar . . . . .	27
3.3	Frequency distribution of life span for all tracks . . . . .	29
3.4	Three track types . . . . .	30
3.5	Frequency distribution of life span . . . . .	31
3.6	Comparison of movement for 26 August 2004, 00 and 06 UTC . . . . .	33
3.7	Comparison of movement for 26 August 2004, 12 and 18 UTC . . . . .	34
4.1	Diurnal cycle of rain rate classes . . . . .	36
4.2	Daily rain totals of 26 August 2004 . . . . .	37

## List of Figures

---

4.3	Frequency distribution of rain rate classes and daily rain sums . . . . .	38
5.1	Diurnal cycles of cluster count and total rain area . . . . .	42
5.2	Model of the diurnal cycle of convective activity . . . . .	44
5.3	CND plus day-to-day and diurnal variation . . . . .	45
5.4	Diurnal variation of CND for individual days . . . . .	45
5.5	Cluster size distribution . . . . .	47
5.6	Parameters of the lognormal distribution . . . . .	48
5.7	Area frequency distribution . . . . .	48
5.8	Definition of the ellipses' parameter . . . . .	49
5.9	Parameter frequency distributions of the ellipses . . . . .	50
5.10	Parameter frequency distributions of the ellipses (large clusters) . . . . .	51
5.11	AIRR, area and AIRR per area as a function of cell number . . . . .	53
6.1	Averaging of AIRR time series on a single day . . . . .	60
6.2	Frequency distribution of AIRR values for five time steps . . . . .	61
6.3	Averaging of AIRR time series over all days . . . . .	62
6.4	Average temporal development of area and AIRR . . . . .	65
6.5	Parameters of the area time series . . . . .	67
6.6	Parameters of the AIRR time series . . . . .	68
6.7	ATIRS as function of life span . . . . .	70
6.8	Average temporal development of AIRR per area . . . . .	71
6.9	Average temporal development of cell number . . . . .	72
8.1	Mean area time series for all three track types . . . . .	83
A.1	Example of a single-cell-track with life span $l = 25$ min . . . . .	85
A.2	Example of a single-cell-track with life span $l = 35$ min . . . . .	85
A.3	Example of a single-cell-track with life span $l = 60$ min . . . . .	85
A.4	Example of a single-cluster-track with life span $l = 35$ min . . . . .	86
A.5	Example of a single-cluster-track with life span $l = 60$ min . . . . .	86
A.6	Example of a single-cluster-track with life span $l = 100$ min . . . . .	86
A.7	Example of a multi-cluster-track with life span $l = 70$ min . . . . .	87

## List of Figures

---

A.8	Example of a multi-cluster-track with life span $l = 115$ min . . . . .	87
A.9	Example of a multi-cluster-track with life span $l = 265$ min . . . . .	87
B.1	Comparison of tracks, daily rain sums and wind field for 25 February 2004 . . . . .	88
B.2	Comparison of tracks, daily rain sums and wind field for 21 March, 23 May and 12 June 2004 . . . . .	89
B.3	Comparison of tracks, daily rain sums and wind field for 10 and 12 July and 13 August 2004 . . . . .	90
B.4	Comparison of tracks, daily rain sums and wind field for 26 and 31 August and 24 September 2004 . . . . .	91
B.5	Comparison of tracks, daily rain sums and wind field for 21 January and 1 and 2 March 2006 . . . . .	92
B.6	Comparison of tracks, daily rain sums and wind field for 5, 6 and 7 March 2006 . . . . .	93
B.7	Comparison of tracks, daily rain sums and wind field for 9 November 2006 . . . . .	94
E.1	Coefficients of variation for area time series . . . . .	101
E.2	Coefficients of variation for AIRR time series . . . . .	102

# List of Tables

2.1	Advanced Z-R-relationship . . . . .	21
3.1	List of analysed days . . . . .	25
3.2	Parameters of the life span frequency distribution fitted to a power law	32
3.3	Parameters of the life span frequency distribution fitted to a modified power law . . . . .	32
4.1	Rain rate classes . . . . .	35
4.2	FFT parameters for the diurnal cycle of rain rate classes . . . . .	37
4.3	Mean dry and wet times . . . . .	38
5.1	FFT parameters for diurnal variations of cell count and rain area . .	43
5.2	Parameters of equations for $\sigma_p$ and $\mu_p$ . . . . .	47
6.1	Frequency of life span . . . . .	62
6.2	Coefficients of variation . . . . .	63
6.3	Parameters of curve fitting . . . . .	64
6.4	Parameters of the area time series . . . . .	67
6.5	Constant $\beta_k$ for the three track types . . . . .	69
D.1	Parameters of the parabola and of the sinus fitted to AIRR time series, single-cell-tracks . . . . .	98
D.2	Parameters of the parabola and of the sinus fitted to AIRR time series, single-cluster-tracks . . . . .	98
D.3	Parameters of the parabola and of the sinus fitted to AIRR time series, multi-cluster-tracks . . . . .	99
D.4	Parameters of the parabola and of the sinus fitted to area time series, single-cell-tracks . . . . .	99

## List of Tables

---

D.5	Parameters of the parabola and of the sinus fitted to area time series, single-cluster-tracks . . . . .	100
D.6	Parameters of the parabola and of the sinus fitted to area time series, multi-cluster-tracks . . . . .	100



# List of Symbols

$\mathbf{a}$	constant of power law (e.g. for Z-R-relationship, cell number distribution, life span distribution)
$\mathbf{a}_0, \mathbf{a}_n$	parameters of the FFT
$\bar{\mathbf{a}}_{k,l}(t)$	area of a track of type $k$ with life span $l$ at time $t$
$\mathbf{A}(\mathbf{p})$	area of a cluster with cell number $p$
$\mathbf{A}_{k,l}$	maximum amplitude of $\bar{f}_{k,l}$ for track type $k$ and life span $l$ [unit of $f$ ]
$\mathbf{A}_{k,l}^*$	maximum amplitude of $\bar{f}_{k,l}^*$ for track type $k$ and life span $l$ [unit of $f$ per unitless time length]
$\mathbf{AIRR}(\mathbf{p})$	area integrated rain rate of a cluster with cell number $p$
$\alpha$	orientation of mean flow, relative to x-direction
$\alpha_{i,k}$	function coefficients
$\mathbf{b}$	exponent of power law (e.g. for Z-R-relationship, cell number distribution, life span distribution)
$\beta$	orientation of ellipses relative to mean flow
$\beta_k$	function coefficient
$\mathbf{c}$	speed of light, $\approx 3 \cdot 10^8 \frac{m}{s}$
$\mathbf{c}_{1,2,3,4}$	function coefficients
$\mathbf{c}_k$	parameter of the sinus fitting functions
$\mathbf{C}$	radar constant
$\mathbf{d}_{1,2,3}$	function coefficients
$\mathbf{d}_k$	parameter of the sinus fitting functions
$\mathbf{D}, \mathbf{D}_{\min}, \mathbf{D}_{\max}$	diameter of particles in the radar volume
$\mathbf{D}_p$	equicircle diameter of a rain area with cell number $p$
$\bar{\mathbf{D}}_p$	mean equicircle diameter of rain areas with cell number $p$
$\bar{\Delta}$	shower index
$\eta$	radar reflectivity
$\bar{f}_{k,l,m}$	mean parameter development for track type $k$ and life span $l$ for individual days $m$
$\bar{f}_{k,l}$	mean parameter development for track type $k$ and life span $l$ for all days
$\bar{f}_{k,l}^*$	mean parameter development for track type $k$ and life span $l$ for all days, normalised with life span

## List of Symbols

---

$\langle \bar{\mathbf{f}}_k^* \rangle$	mean parameter development for track type $k$ , normalised with life span and with maximum amplitude
$\mathbf{g}_k, \mathbf{h}_k$	parameters of the parabola fitting functions
$\mathbf{k}$	track type
$ \mathbf{k} ^2$	factor in the radar equation depending on aggregation state of hydrometeors
$l$	life span of a track
$L$	mean cloud spacing
$\lambda$	wavelength of the radar signal
$\mathbf{m}$	day
$\mu_p$	mean of the lognormal cluster size distribution for cell number $p$
$\langle N \rangle$	average number of clouds within a rain area
$N(\mathbf{D})$	size distribution of the particles in the radar volume
$N(l)$	life span distribution
$N(p)$	cell number distribution
$\text{obs}_{\text{synop}}$	daily rain sum from synoptic observations
$\text{obs}_{\text{radar}}$	daily rain sum from radar measurements
$p$	cell number
$p_{\text{max}}$	maximum cell number occurring
$P_r$	received power at radar station
$\phi_n$	parameters of the fast Fourier transformation
$r$	distance from radar station to the target
$\bar{r}_{k,l}(t)$	area integrated rain rate of a track of type $k$ with life span $l$ at time $t$
$r_{\text{max}}$	maximum range for unambiguous radar measurement
$\mathbf{R}$	rain rate [ $mm/h$ ]
$\mathbf{R}^2$	coefficient of determination
$\mathcal{R}$	correlation coefficient
$\bar{\mathbf{R}}_{k,l}$	mean area and time integrated rain sum
$\sigma_i$	backscattering cross section of the individual particles
$\sigma_p$	standard deviation of the lognormal cluster size distribution for cell number $p$
$t$	time
$t^*$	time normalised with life span
$\tau$	duration of pulsed radar signal
$\mathbf{V}$	unit volume
$\Delta \mathbf{x}$	size of a region of interest
$\mathbf{Z}$	radar reflectivity factor

# List of Abbreviations

<b>RHI</b>	<b>R</b> ange- <b>H</b> eight <b>I</b> ndicator,
<b>RVP-6</b>	Encoding of radar reflectivity values for the RX composite,
<b>AIRR</b>	<b>A</b> rea <b>I</b> ntegrated <b>R</b> ain <b>R</b> ate,
<b>ATIRS</b>	<b>A</b> rea and <b>T</b> ime <b>I</b> ntegrated <b>R</b> ain <b>S</b> um,
<b>CAPE</b>	<b>C</b> onvective <b>A</b> vailable <b>P</b> otential <b>E</b> nergy,
<b>CAPPI</b>	<b>C</b> onstant- <b>A</b> ltitude <b>P</b> lan- <b>P</b> osition <b>I</b> ndicator,
<b>CND</b>	<b>C</b> ell <b>N</b> umber <b>D</b> istribution,
<b>COSMO</b>	<b>C</b> Onsortium for <b>S</b> mall-scale <b>M</b> Odelling,
<b>CSD</b>	<b>C</b> luster <b>S</b> ize <b>D</b> istribution,
<b>dBZ</b>	Decibels of radar reflectivity (factor) Z,
<b>DFG</b>	German Research Foundation ( <b>D</b> eutsche <b>F</b> orschungs <b>G</b> esellschaft,
<b>DWD</b>	German Weather Service ( <b>D</b> eutscher <b>W</b> etter <b>D</b> ienst),
<b>FFT</b>	<b>F</b> ast <b>F</b> ourier <b>T</b> ransformation,
<b>LMSA</b>	<b>L</b> arge <b>M</b> eso <b>S</b> cale <b>A</b> rea,
<b>MCS</b>	<b>M</b> esoscale <b>C</b> onvective <b>S</b> ystem,
<b>PPI</b>	<b>P</b> lan- <b>P</b> osition <b>I</b> ndicator,
<b>PRF</b>	<b>P</b> ulse- <b>R</b> epetition <b>F</b> requency,
<b>RADAR</b>	<b>R</b> Adio <b>D</b> etection <b>A</b> nd <b>R</b> anging,
<b>SMSA</b>	<b>S</b> mall <b>M</b> eso <b>S</b> cale <b>A</b> rea,
<b>SOC</b>	<b>S</b> elf- <b>O</b> rganised <b>C</b> riticality,
<b>UTC</b>	<b>C</b> oordinated <b>U</b> niversal <b>T</b> ime,

# Acknowledgements

Finally, it is time to address the people which accompanied me during those last years. First of all I would like to thank my mentor and advisor Prof. Dr. Thomas Hauf who entrusted me with the DFG project and gave me the possibility to do my PhD within this project. I enjoyed the mostly self dependent work on a project with all duties that belong to this position including the opportunity to participate in various national and international meetings and conferences. I'd also like to express my thanks to Prof. Dr. Dieter Etling for taking the Korreferat of this thesis.

Further thanks go to:

- The German Research Foundation (DFG) for funding this work through the project *Hybrid probabilistic forecast scheme for post-frontal shower precipitation* under grant numbers HA 1761/5-1 and 5-2 within the Priority Program 1167 *Quantitative Precipitation Forecast*.
- The German Weather Service (DWD), hydro-meteorological department, for providing the radar data which forms the basis for the analyses.
- Sarah and Ole, Jakob, Florian and Darius for partially or completely proof reading my manuscript.
- Dominik and Benjamin for their auxiliary work.
- My former room-mates Katharina, Peer and Michael for the good times with coffee and cookies and for tips and advices when problems with IDL or L<sup>A</sup>T<sub>E</sub>X occurred. Special thanks also to Danijela and Clemens for their support.
- The working group *Allgemeine Meteorologie* with its actual and previous members, who are not explicitly named here, as well as the students and colleagues at the IMUK for the pleasant atmosphere.
- Last but not least special thanks to my family for being as they are and for their support and encouragement, especially in the last weeks of my thesis.

# Curriculum Vitae

Family Name	Weusthoff
First Name	Tanja
Date of Birth	07. August 1976
Place of Birth	Gifhorn
Nationality	german

## Education and Academic Career

since 07/2008	Research assistant, Bundesamt für Meteorologie und Klimatologie, MeteoSwiss, Zürich
06/2005 - 07/2008	Research assistant, Institut für Meteorologie und Klimatologie, Leibniz Universität Hannover
10/1999 - 05/2005	Studies of Meteorology, Institut für Meteorologie und Klimatologie, Leibniz Universität Hannover
08/2003 - 01/2004	Studies of Meteorology and Hydrology, Uppsala University, Sweden, ERASMUS student exchange
01/1999 - 07/1999	Employee, Vermessungs- und Katasterbehörde Wolfsburg, Katasteramt Gifhorn
10/1996 - 01/1999	Professional training as a Vermessungstechnikerin, Vermessungs- und Katasterbehörde Wolfsburg, Katasteramt Gifhorn
08/1989 - 05/1996	Humboldt-Gymnasium Gifhorn

## Scientific Publications

WEUSTHOFF, T. AND T. HAUF, 2008: *Basic characteristics of post-frontal shower precipitation rates*, Meteorol. Z., **17**(6), 793–805

WEUSTHOFF, T. AND T. HAUF, 2008: *The life cycle of convective-shower cells under post-frontal conditions*, Q. J. R. Meteorol. Soc., **134**(633), 841–857